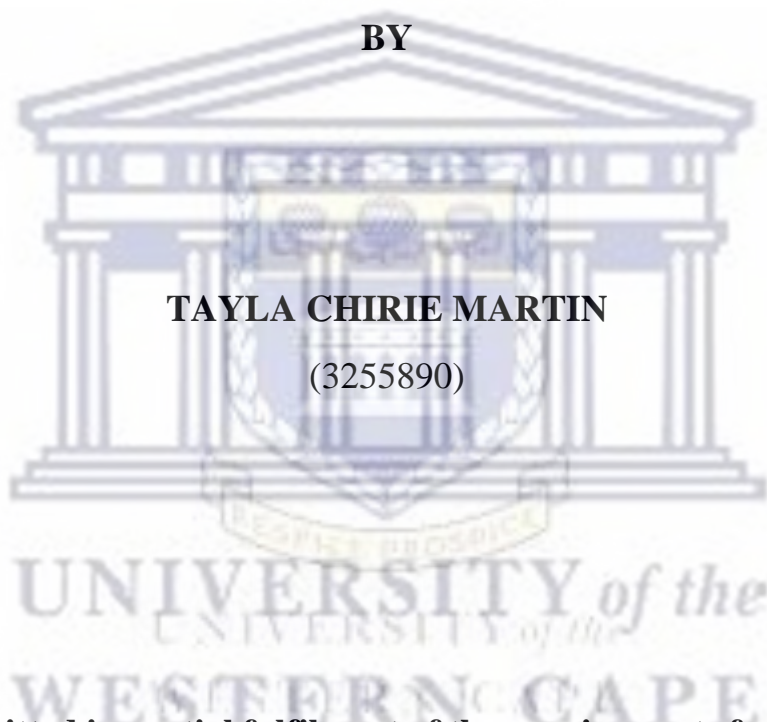


**UPSCALE EFFECTS IN THE PREPARATION OF METAL HYDRIDE
MATERIALS**

BY

TAYLA CHIRIE MARTIN
(3255890)



**A thesis submitted in partial fulfilment of the requirements for the degree of
Doctor of Philosophy in the Department of Chemistry, Faculty of Natural
Science, University of Western Cape**

SUPERVISOR: DR. MYKHAYLO LOTOTSKYY

CO-SUPERVISOR: DR. MOEGAMAT WAFEEQ DAVIDS

2024

KEYWORDS

Alloy

Arc melting

Hydrogen storage

HySA

Induction melting

Laves phase

Metal hydrides

Sievert's method

Ti-Zr based AB₂ alloys

Pressure composition isotherm



UNIVERSITY of the
WESTERN CAPE

ABSTRACT

The preparation of Ti-Zr based AB₂ alloys where A=Ti, Zr ; B= Mn,Cr, Ni, Fe, V, Cu for use in hydrogen storage was investigated. In Ti-Zr based AB₂ metal hydrides, the effects of composition, microstructure, and hydrogen sorption properties were examined using Scanning electron microscope (SEM), Energy dispersive x-ray spectroscopy (EDS), X-ray diffraction (XRD), and Sievert's type Pressure composition temperature (PCT) measurements. Alloys were prepared by arc melting and induction melting.

Ti_{0.85}Zr_{0.15}Cr_{0.2}Mn_{1.22}Ni_{0.22}V_{0.3}Fe_{0.06} alloy prepared by arc melting served as the base alloy. The EDS and XRD revealed that the alloy contained no impurities with a single C14 Laves phase and had a maximum storage capacity of 1.8 wt.% H₂ at 20°C .

The base alloy additionally doped with Lanthanum (Ti_{0.85}Zr_{0.15}Cr_{0.2}Mn_{1.22}Ni_{0.22}V_{0.3}Fe_{0.06}La_{0.02}) was prepared by induction melting with an alumo-silica crucible and graphite crucible, respectively. The alumo-silica crucible was coated with a Y₂O₃ slurry, whereas the graphite crucible was coated with Mo slurry + (Y₂O₃ + Mo) + Y₂O₃ slurry. However, even though coated with Y₂O₃, the XRD revealed an impurity phase in both alloys (La₂TiO₅) with an additional impurity phase in the alloy prepared by alumo-silica crucible (Ti,Zr)O₂. The transmission electron microscope (TEM) results showed that the alloy prepared with alumo silica crucible had the poorest crystallinity due to the additional impurity phase, whereas the alloy prepared with graphite crucible had the highest degree of crystallinity. In addition, the atomic emission spectroscopy (AES) results showed that alloy prepared by alumo silica crucible had the maximum amount of oxygen whereas the oxygen content decreased by 3% for the alloy prepared with graphite crucible. Finally, the hydrogen storage capacity decreased from the initial 1.8 wt.% to 1.36 wt.% and 1.5 wt.%, for alloy prepared with the alumo silica crucible and graphite crucible, respectively.

Oxygen was introduced to the base alloy (Ti_{0.85}Zr_{0.15}Cr_{0.2}Mn_{1.22}Ni_{0.22}V_{0.3}Fe_{0.06}O_{0.05}) to investigate its influence on the alloy's performance. The SEM/EDS results of the alloy modified by oxygen showed that the surface contained more cracks than the unmodified alloy (base alloy). In addition, the total oxygen impurity was 0.78% from EDS data. The XRD revealed that both the unmodified and modified oxygen alloy consisted of the main C14 Laves phase and also an impurity phase of η-phase (Ti₄Fe₂O_{1-x}). The reason for the impurity phase in the unmodified alloy was due to the commercial use of ferrovanadium (FeV). The hydrogen

absorption kinetics revealed that the hydrogen intake for the oxygen-modified alloy was slower after activation by vacuum heating. However, in the non-activated state, the hydrogen intake was immediate due to the impurity phase acting as a catalyst, but this ultimately caused a decrease in hydrogen storage capacity.

The effect of changing the Ti/Zr ratio on hydrogen sorption performance of $Ti_xZr_yCr_{0.2}Mn_{1.22}Ni_{0.22}V_{0.3}Fe_{0.06}$ ($x=0.9, 0.8$; $y=0.1, 0.2$) was also studied. The EDS data revealed that despite having Cr and Fe in the composition, it was absent in the EDS data. This may be due to the increase in Ti content since the atomic radii is larger than Cr and Fe and may occupy the B-sites of Cr and Fe. By increasing the Zr content, the lattice parameter and unit cell volume increased due to the larger Zr atomic radius than the Ti one. However, this led to a decrease in hydrogen storage capacity.

A substitution of a cheaper alternative material such as FeV was also investigated. The $Ti_{0.85}Zr_{0.15}Cr_{0.2}Mn_{1.2}Ni_{0.22}Cu_{0.02}FeV_{0.42}$ showed to exhibit a single C14 phase in the XRD, however in the EDS data a minor silicon impurity was found. The hydrogen storage capacity compared to the base alloy, decreased to 1.5 wt.%.

Finally, the effect of changing Mn/Cr ratio by $Ti_{0.85}Zr_{0.15}Cr_xMn_yNi_{0.22}V_{0.3}Fe_{0.06}$ ($x=0, 0.3, 0.6$; $y=1.4, 1.1, 0.8$) showed to have a decrease in hydrogen storage capacity with increasing Cr content. However, the hydrogen capacity with the alloy containing no Cr, showed to have a higher maximum hydrogen storage capacity than the base alloy.

DECLARATION

I declare that *Upscaling effect in the preparation of metal hydride materials* is my own work, that it has not been submitted for any degree or examination in any other university, and that all the sources I have used or quoted have been indicated and acknowledged by complete references

Tayla Martin

Date:

Signed:



UNIVERSITY of the
WESTERN CAPE

ACKNOWLEDGEMENTS

I would like to thank my supervisors, Dr Moegamat Wafeeq Davids and Dr Mykhaylo Lototsky, for their continued patience, advice and mentorship.

To Hydrogen South Africa (HySA), and South African Institute for Advanced Materials Chemistry (SAIAMC) for allowing me to complete my PhD studies in their facility.

To the funders, Department of Science, Technology and Innovation (DSTI), and National Research Foundation (NRF), for financial support throughout my study.

To my husband and family for their support.



UNIVERSITY of the
WESTERN CAPE

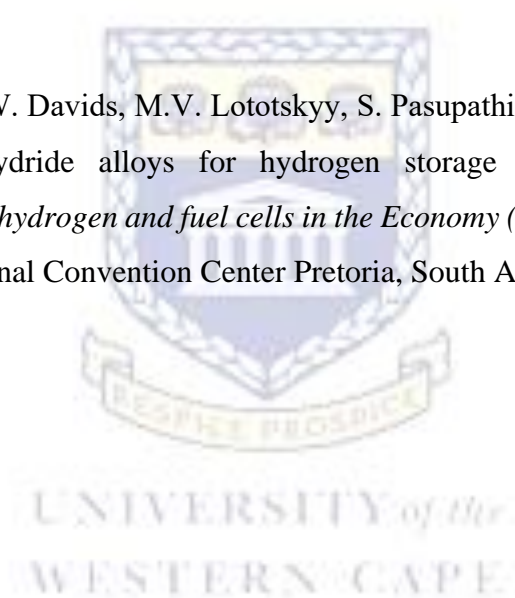
RESEARCH OUTPUTS

Publications

- M.W Davids, **T. Martin**, M. Lototskyy, R. Denys, V. Yartys. “Study of Hydrogen Storage Properties of Oxygen modified Ti-based AB₂ type Metal Hydride Alloys” *Manuscript published in International Journal of Hydrogen Energy (IF = 8.1)*
- M.W Davids, **T. Martin**, P.V. Fursikov, M. V. Zhidkov, I. Khodos, S. Fashu, M. V. Lototskyy. “Effect of preparation routes on the performance of a multi-component AB₂-type hydrogen storage alloy”. *Manuscript published in Journal of Physics: Energy (IF = 7)*

Presentation

- **T. Martin**, M.W. Davids, M.V. Lototskyy, S. Pasupathi. “Upscaling of Ti-Zr based AB₂ Metal Hydride alloys for hydrogen storage application” *International Partnership for hydrogen and fuel cells in the Economy (IPHE)*, Poster Presentation. CSIR International Convention Center Pretoria, South Africa, 24 – 25 April 2023.



LIST OF FIGURES

Figure 1. 1: HySA structure.....	4
Figure 2. 1: Simplified phase diagram for hydrogen	8
Figure 2. 2: Flows of mass and energy for a general fuel cell.....	11
Figure 2. 3: Hydrogen storage technology categorized.	17
Figure 2. 4: Reaction of a H ₂ molecule with a storage material: a) H ₂ molecule approaching the metal surface. (b) Interaction of the H ₂ molecule by Van der Waals forces (physisorbed state). (c) Chemisorbed hydrogen after dissociation. (d) Occupation of subsurface sites and diffusion into bulk lattice sites.....	21
Figure 2. 5: A Pressure-Composition-Temperature Isotherm (PCT) plot.	22
Figure 2. 6: A PCT plot illustrating absorption and desorption.....	22
Figure 2. 7: PCT diagram(left) at different temperatures ($T_1 < T_2 < T_3 < T_4 < T_c$). The α -phase is the solid solution phase, the β -phase the hydride phase. Within the (α - β) two phase region both the metal-hydrogen solution and the hydride phase coexist. The van't Hoff plot diagram (right)	23
Figure 2. 8: Schematic of (a) C14 (hexagonal), (b) C15 (cubic), and (c) C36 (rhombohedral) crystal structures.	25
Figure 2. 9: XRD patterns of Ti-Zr-V-Cr-Ni high entropy alloy, (a) as cast, (b) annealed, and (c) rapidly solidified ribbon.	29
Figure 2. 10: XRD patterns of Ti _{0,72} Zr _{0,28} Mn _{1,6} V _{0,4} alloy produced by (a) vacuum copper boat induction melting, (b) vacuum plasma spraying.....	30
Figure 3. 1: Arc-melter at IFE, Norway.....	35
Figure 3. 2: Images and schematic cross-section of the Y ₂ O ₃ – coated crucibles	36
Figure 3. 3: Basic diagram of Sievert's system	41
Figure 4. 1: SEM images of the AB ₂ -type alloy prepared by (A) – arc-melting and annealing, (B) – induction melting in alumo-silica crucible, and (C) – induction melting in graphite crucible.....	44
Figure 4. 2: Observed (points) and calculated (red lines) XRD patterns of the AB ₂ -type alloy prepared by (A) – arc-melting, (B) – induction melting in alumo-silica crucible, and (C) – induction melting in graphite crucible. Bottom ticks show the calculated peak positions of the	46
Figure 4. 3: TEM images (A,C,E) and the corresponding SAED patterns (B,D,F) for the arc-melted sample (A,B), the sample induction melted in the alumo-silica crucible (C,D) and the sample induction melted in the graphite crucible (E,F).....	48
Figure 4. 4: TEM images (A,C,E) and the corresponding SAED patterns (B,D,F) of separate particles for the arc-melted sample (A,B), the sample induction melted in the alumo-silica crucible (C,D) and the sample induction melted in the graphite crucible (E,F).	49
Figure 4. 5: Selected area of the TEM image (A) taken for the sample induction melted in alumo-silica crucible and the corresponding SAED patterns supplemented by Miller indexes of rings and spots for the major C14-AB ₂ phase (B) and La ₂ TiO ₅ impurity (C).....	50
Figure 4. 6: Fragments of atomic emission spectra for the arc-melted sample (1) and samples induction melted in alumo-silica (2) and graphite (3) crucible. The most intensive oxygen spectral lines are shown by the vertical arrows.	51

Figure 4. 7: Hydrogen absorption and desorption isotherms at T=20°C (A) and van't Hoff plots for the AB ₂ -type alloy samples (B): (1) – arc melted, (2) – induction-melted in alumo-silica crucible and (3) – induction-melted in graphite crucible. Points a, b and c on the absorption isotherm for the arc melted sample (1 in A) correspond to hydrogen pressures and concentrations for which kinetic data (Figure 4.8A,B) are presented..	52
Figure 4. 8: Hydrogen absorption kinetics and changes of the sample temperature at T ₀ =21°C for the arc melted sample: A – first absorption at the starting H ₂ pressure of 33 bar and final H ₂ pressure of 27 bar (point a in Figure 4.7A). B – hydrogen absorption during the measurement of the pressure–composition isotherm (points b and c in Figure 4.7A).	53
Figure 4. 9: SEM images for the arc-melted samples: (A) Ti _{0.85} Zr _{0.15} Cr _{0.2} Mn _{1.22} Ni _{0.22} V _{0.3} Fe _{0.06} , (B) Ti _{0.85} Zr _{0.15} Cr _{0.2} Mn _{1.22} Ni _{0.22} V _{0.3} Fe _{0.06} O _{0.05}	56
Figure 4. 10: XRD patterns for arc-melted samples (A) as prepared AB ₂ alloy, (B) hydrogenated AB ₂ alloy, (C) as prepared AB ₂ O _{0.05} alloy, (D) hydrogenated AB ₂ O _{0.05} .	57
Figure 4. 11: Hydrogen absorption kinetics at T=20 °C and P ₀ = 30 bar for the Ti-based AB ₂ type alloys: (1) AB ₂ alloy without activation, (2) AB ₂ O _{0.05} alloy without activation, (3) AB ₂ O _{0.05} alloy after activation by vacuum heating at 300 °C for 1 hr, (4) AB ₂ alloy after activation by vacuum heating at 300 °C for 1 hr.	58
Figure 4. 12: Hydrogen absorption and desorption isotherms for Ti-Zr based AB ₂ alloys (A) Unmodified AB ₂ , (B) Oxygen modified AB ₂ alloy	59
Figure 4. 13: Van't Hoff plots for hydrogen absorption and desorption for the unmodified (A) and modified (B) alloys.	60
Figure 4. 14:	61
Figure 4. 15: XRD patterns of (A) Ti _{0.9} Zr _{0.1} Cr _{0.2} Mn _{1.2} Ni _{0.22} Cu _{0.02} V _{0.3} Fe _{0.06} and (B)Ti _{0.8} Zr _{0.2} Cr _{0.2} Mn _{1.2} Ni _{0.22} Cu _{0.02} V _{0.3} Fe _{0.06}	63
Figure 4. 16: PCT isotherms of (A) Ti _{0.9} Zr _{0.1} Cr _{0.2} Mn _{1.2} Ni _{0.22} Cu _{0.02} V _{0.3} Fe _{0.06} and (B) Ti _{0.8} Zr _{0.2} Cr _{0.2} Mn _{1.2} Ni _{0.22} Cu _{0.02} V _{0.3} Fe _{0.06} prepared by arc melting at different temperatures.	65
Figure 4. 17: Van't Hoff plots for hydrogen absorption and desorption for (A) Ti _{0.9} Zr _{0.1} Cr _{0.2} Mn _{1.2} Ni _{0.22} Cu _{0.02} V _{0.3} Fe _{0.06} and (B) Ti _{0.8} Zr _{0.2} Cr _{0.2} Mn _{1.2} Ni _{0.22} Cu _{0.02} V _{0.3} Fe _{0.06}	65
Figure 4. 18: SEM image of (A) Ti _{0.85} Zr _{0.15} Cr _{0.2} Mn _{1.2} Ni _{0.22} Cu _{0.02} FeV _{0.42} and (B) pure FeV at low magnification.	67
Figure 4. 19: Refined XRD patterns of Ti _{0.85} Zr _{0.15} Cr _{0.2} Mn _{1.2} Ni _{0.22} Cu _{0.02} FeV _{0.42}	69
Figure 4. 20: (A) PCT isotherms of Ti _{0.85} Zr _{0.15} Cr _{0.2} Mn _{1.2} Ni _{0.22} Cu _{0.02} FeV _{0.42} , (B) van't Hoff plots for hydrogen absorption and desorption of Ti _{0.85} Zr _{0.15} Cr _{0.2} Mn _{1.2} Ni _{0.22} Cu _{0.02} FeV _{0.42} .	70
Figure 4. 21: Surface morphology of (A)Ti _{0.85} Zr _{0.15} Mn _{1.4} Ni _{0.22} Cu _{0.02} Fe _{0.06} V _{0.3} , (B)Ti _{0.85} Zr _{0.15} Cr _{0.3} Mn _{1.1} Ni _{0.22} Cu _{0.02} Fe _{0.06} V _{0.3} , and (C)Ti _{0.85} Zr _{0.15} Cr _{0.6} Mn _{0.8} Ni _{0.22} Cu _{0.02} Fe _{0.06} V _{0.3} .	71
Figure 4. 22: XRD patterns of (a) Ti _{0.85} Zr _{0.15} Mn _{1.4} Ni _{0.22} Cu _{0.02} Fe _{0.06} V _{0.3} , (b)Ti _{0.85} Zr _{0.15} Cr _{0.3} Mn _{1.1} Ni _{0.22} Cu _{0.02} Fe _{0.06} V _{0.3} , and (c) Ti _{0.85} Zr _{0.15} Cr _{0.6} Mn _{0.8} Ni _{0.22} Cu _{0.02} V _{0.3} Fe _{0.06}	73
Figure 4. 23: PCT isotherms of (A) Ti _{0.85} Zr _{0.15} Mn _{1.4} Ni _{0.22} Cu _{0.02} Fe _{0.06} V _{0.3} , (B) Ti _{0.85} Zr _{0.15} Cr _{0.3} Mn _{1.1} Ni _{0.22} Cu _{0.02} Fe _{0.06} V _{0.3} , and (C) Ti _{0.85} Zr _{0.15} Cr _{0.6} Mn _{0.8} Ni _{0.22} Cu _{0.02} Fe _{0.06} V _{0.3} prepared by arc melting at different temperatures.	75

Figure 4. 24: Van't Hoff plots for hydrogen absorption and desorption for (A) $\text{Ti}_{0,85}\text{Zr}_{0,15}\text{Mn}_{1,4}\text{Ni}_{0,22}\text{Cu}_{0,02}\text{Fe}_{0,06}\text{V}_{0,3}$, (B) $\text{Ti}_{0,85}\text{Zr}_{0,15}\text{Cr}_{0,3}\text{Mn}_{1,1}\text{Ni}_{0,22}\text{Cu}_{0,02}\text{Fe}_{0,06}\text{V}_{0,3}$, and (C) $\text{Ti}_{0,85}\text{Zr}_{0,15}\text{Cr}_{0,6}\text{Mn}_{0,8}\text{Ni}_{0,22}\text{Cu}_{0,02}\text{Fe}_{0,06}\text{V}_{0,3}$ 76



UNIVERSITY of the
WESTERN CAPE

LIST OF TABLES

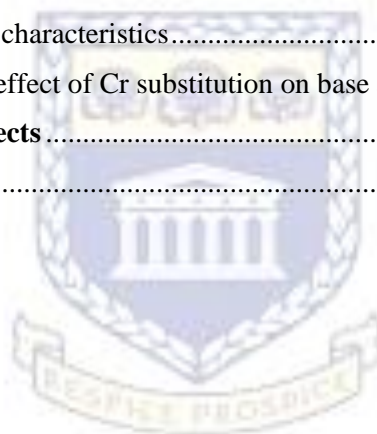
Table 2. 1: Summary of fuel cell types	12
Table 2. 2: Storage capacities of different hydrogen storage materials	14
Table 2. 3: Examples of intermetallic hydrides.....	16
Table 2. 4: Hydrogen storage capacities of absorption materials	16
Table 2. 5: Laves phases with stacking sequences.....	26
Table 2. 6: Summary on ball milled variables of Ti-Zr based AB ₂ alloys.....	28
Table 4. 1: Summary of compositional properties of the alloy samples according to EDS data collected from typical points (1–3 in Figure 4.1).	44
Table 4. 2: Results of Rietveld refinement of the XRD patterns of the studied alloy samples (Figure 4.2). Errors of the values calculated during refinement (shown in brackets) relate to the last decimal digit.	47
Table 4. 3: Hydrogen sorption parameters of the studied alloy samples	53
Table 4. 4: Compositional properties of the multi component AB ₂ type alloys prepared via arc melting	56
Table 4. 5: EDS data of arc-melted (A)Ti _{0,9} Zr _{0,1} Cr _{0,2} Mn _{1,2} Ni _{0,22} Cu _{0,02} V _{0,3} Fe _{0,06} and (B)Ti _{0,8} Zr _{0,2} Cr _{0,2} Mn _{1,22} Ni _{0,22} Cu _{0,02} V _{0,3} Fe _{0,06}	62
Table 4. 6: Results of Rietveld refinement of the XRD patterns of the studied alloy samples (Figure 4.13). Errors of the values calculated during refinement (shown in brackets) relate to the last decimal digit.	63
Table 4. 7: EDS data of arc-melted Ti _{0,85} Zr _{0,15} Cr _{0,2} Mn _{1,2} Ni _{0,22} Cu _{0,02} FeV _{0,42}	68
Table 4. 8: EDS data of pure FeV	68
Table 4. 9: EDS data of Cr substituted alloys prepared by arc melting.....	72
Table 4. 10: Results of Rietveld refinement of the XRD patterns of the studied alloy samples (Figure 4.18). Errors of the values calculated during refinement (shown in brackets) relate to the last decimal digit.	74

TABLE OF CONTENTS

KEYWORDS	ii
ABSTRACT	iii
DECLARATION	v
ACKNOWLEDGEMENTS	vi
RESEARCH OUTPUTS	vii
LIST OF FIGURES	viii
LIST OF TABLES	xi
TABLE OF CONTENTS	xii
Chapter 1: Introduction	1
1.1 Motivation of research	1
1.2 Problem statement.....	3
1.3 HySA program.....	4
1.4 Objectives and Aim of Research.....	5
1.5 Thesis outline.....	6
Chapter 2: Literature Review	7
2.1 Properties of Hydrogen	7
2.2 Hydrogen Production	9
2.3 Hydrogen distribution and delivery	10
2.4 Hydrogen storage and conversion.....	10
2.4.1 Combustion engines.....	10
2.4.2 Fuel cells	11
2.5 Hydrogen storage	13
2.5.1 Physical storage methods:.....	13
2.5.2 Physical-Chemical storage.....	15
2.5.3 Adsorption on high surface area materials.....	19
2.6 Metal hydride/hydrogen interactions	20
2.6.1 Hydrogen in metal hydrides.....	20
2.6.2 Pressure Composition Temperature Isotherms	21
2.6.3 Thermodynamics.....	23
2.6.4 Heat Transfer	24
2.7 Phase structure of AB ₂ alloys.....	25
2.8 Zr-based AB ₂ alloys	26
2.9 Ti - Zr based AB ₂ alloys	26
2.10 Phase structure and hydrogen sorption characteristics with regards to upscaling techniques	27

i.	Ball milling	27
ii.	Rapid solidification techniques	28
iii.	Induction melting	31
2.11	Phase structure and hydrogen sorption characteristics in Ti-Zr based AB ₂ alloys by arc melting	32
2.12	Limitations of AB ₂ metal hydride alloys	33
2.13	Conclusion	34
Chapter 3: Preparation of alloys and Characterization techniques		35
3.1	Alloy preparation techniques	35
3.1.1	Arc melting	35
3.1.2	Induction melting	36
3.2	Characterization of alloys	38
3.2.1	X-ray Diffraction.....	38
3.2.2	Scanning Electron Microscope	39
3.2.3	Transmission Electron Microscope.....	39
3.2.4	Hydrogen sorption measurements.....	40
Chapter 4: Results and Discussion		43
4.1	Effect of preparation routes on the performance of a multi-component Ti-Zr based AB ₂ -type hydrogen storage alloy	43
4.1.1	Surface morphology and elemental composition of Ti-Zr based AB ₂ type alloys prepared by different routes	43
4.1.2	Phase and structural characterisation of Ti-Zr based AB ₂ type alloys prepared by different routes	45
4.1.3	TEM, SAED and AES characterisation of Ti-Zr based AB ₂ type alloys prepared by different routes	47
4.1.4	Hydrogen sorption properties of Ti-Zr based AB ₂ type alloys prepared by different routes	51
4.1.5	Conclusions on the effect of preparation routes of Ti-Zr based AB ₂ type alloys	54
4.2	Effect of Oxygen substitution on Ti-Zr based AB ₂ alloy	55
4.2.1	Surface morphology and elemental composition of oxygen modified Ti-Zr based AB ₂ alloy	55
4.2.2	Phase and structural properties of oxygen modified Ti-Zr based AB ₂ alloy.....	57
4.2.3	Hydrogen absorption kinetics of the unmodified and oxygen-modified Ti based AB ₂ alloy	58
4.2.4	Hydrogen sorption PCT properties of unmodified and oxygen-modified Ti based AB ₂ alloy	59
4.2.5	Conclusions of Oxygen substitution on Ti-Zr based AB ₂ alloy	60
4.3	Effect of changing Ti-Zr ratio	61
4.3.1	Surface morphology and elemental composition of Ti _{0,9} Zr _{0,1} Cr _{0,2} Mn _{1,2} Ni _{0,22} Cu _{0,02} V _{0,3} Fe _{0,06} and Ti _{0,8} Zr _{0,2} Cr _{0,2} Mn _{1,22} Ni _{0,22} Cu _{0,02} V _{0,3} Fe _{0,06}	61

4.3.2	Phase and structural properties of $Ti_{0,9}Zr_{0,1}Cr_{0,2}Mn_{1,2}Ni_{0,22}Cu_{0,02}V_{0,3}Fe_{0,06}$ and $Ti_{0,8}Zr_{0,2}Cr_{0,2}Mn_{1,22}Ni_{0,22}Cu_{0,02}V_{0,3}Fe_{0,06}$	63
4.3.3	Hydrogen sorption characteristics.....	64
4.3.4	Conclusions on the effect of changing Ti-Zr ratio	66
4.4	The effect of Ferrovandium on the base alloy.....	67
4.4.1	Surface morphology and elemental composition of $Ti_{0,85}Zr_{0,15}Cr_{0,2}Mn_{1,2}Ni_{0,22}Cu_{0,02}FeV_{0,42}$	67
4.4.2	Phase structure	69
4.4.3	Hydrogen sorption characteristics.....	70
4.4.4	Conclusion on the effect of Ferrovandium on base alloy.....	70
4.5	Effect of Chromium/Manganese substitution on the base alloy	71
4.5.1	Surface morphology and elemental composition of $Ti_{0,85}Zr_{0,15}Mn_{1,4}Ni_{0,22}Cu_{0,02}Fe_{0,06}V_{0,3}$, $Ti_{0,85}Zr_{0,15}Cr_{0,3}Mn_{1,1}Ni_{0,22}Cu_{0,02}Fe_{0,06}V_{0,3}$, and $Ti_{0,85}Zr_{0,15}Cr_{0,6}Mn_{0,8}Ni_{0,22}Cu_{0,02}Fe_{0,06}V_{0,3}$	71
4.5.2	Phase structure	73
4.5.3	Hydrogen sorption characteristics.....	74
4.5.4	Conclusion on the effect of Cr substitution on base alloy.....	76
5.	Conclusion and Future prospects	77
	References.....	79



UNIVERSITY of the
WESTERN CAPE



UNIVERSITY *of the*
WESTERN CAPE

Chapter 1: Introduction

1.1 Motivation of research

The demand for fossil fuels, for instance; coal, natural gas, gasoline and diesel has led to consistent environmental issues such as global warming, air pollution and climate change due to the toxic release of carbon dioxide (CO₂) emissions [1],[2]. Renewable energy sources like wind and solar will be available infinitely. However, the requirement to store excess energy during high energy demand remains a problem. A promising solution for reducing CO₂ emissions is utilising hydrogen as an energy carrier for stationary and mobile applications. Hydrogen is considered as a renewable and clean energy carrier. When burnt with oxygen, its only by-product is water [3]. Hydrogen can be produced by various renewable sources of energy such as hydroelectric, wind, solar, and geothermal, with water being the only raw material needed, thus in terms of obtaining and distribution of hydrogen as a fuel source, a country's reliance on foreign energy resources can be drastically reduced. Therefore, hydrogen presents immense positive socio-economic incentives. However, while hydrogen has many advantages, one of the major shortcomings of widespread use of hydrogen as an energy source is its effective storage. To successfully use hydrogen as an energy carrier, suitable storage techniques are required:

- a) Compressed hydrogen gas
- b) Liquid hydrogen
- c) Solid state of hydrogen

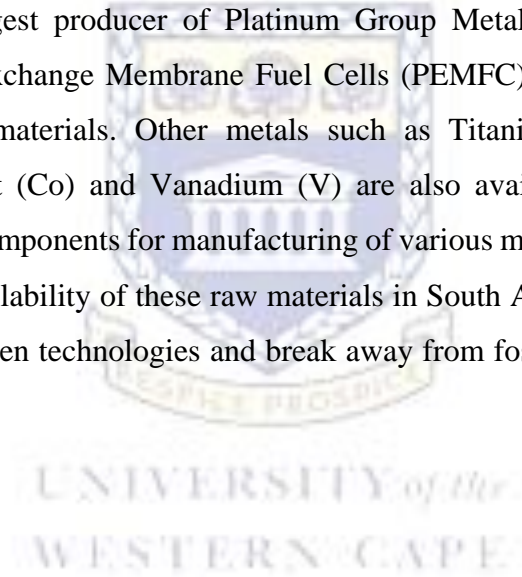
Compressed hydrogen gas and liquid hydrogen require hydrogen to be stored in either gaseous or liquid form in high-pressure or cryogenic tanks [4]. The downside to these techniques is in safety concerns, as well as high energy consumption for hydrogen compression and liquefaction.

Solid-state hydrogen storage allows hydrogen to be stored in solid materials rather than in gaseous and liquid states. This approach is considered a promising solution for safely and efficiently storing hydrogen. Metal Hydride (MH) hydrogen storage has shown to be a promising solid-state hydrogen storage technique which is based on metals and alloys which are able to reversibly and selectively interact with hydrogen both from gas (gas phase application) and an electrolyte (electrochemical applications). MH are characterised by unique properties, including extremely high volume density of H atoms accommodated in the metal

matrix, wide tuneability of thermodynamics and fast kinetics of hydrogenation / dehydrogenation, selectivity of hydrogen uptake process, significant changes of physical properties of the host metal (alloy) in the course of its hydrogenation, catalytic activity in hydrogen transfer reactions, etc. The MH technologies utilising these features is a typical application-driven niche area able to provide very efficient solutions for hydrogen handling in a particular end-use application by the tuning of several parameters, including component and phase composition of the parent MH material, system layout, operation conditions, etc. [5]

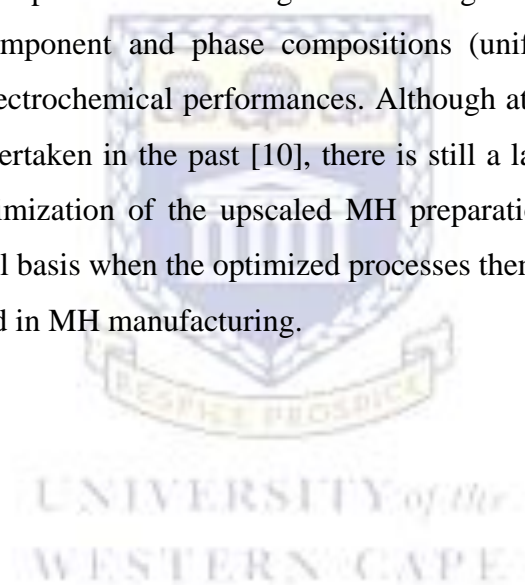
Laves phase AB_2 metal hydrides have been the focus of much research for the replacement of AB_5 metal hydrides. AB_2 metal hydrides exhibit high energy density and design flexibility [6] compared to AB_5 metal hydrides. AB_2 alloys are cheaper than AB_5 alloys, particularly if component A is Titanium [7]. More on these materials will be discussed in Chapter 2.

South Africa is the biggest producer of Platinum Group Metals (PGM), which is a key component for Proton Exchange Membrane Fuel Cells (PEMFC) but could also be used to prepare advanced MH materials. Other metals such as Titanium (Ti), Zirconium (Zr), Manganese (Mn), Cobalt (Co) and Vanadium (V) are also available commercially in the country, which are key components for manufacturing of various metal hydride-forming alloys of the AB_2 type. The availability of these raw materials in South Africa gives it an advantage to focus solely on hydrogen technologies and break away from fossil fuels for stationary and mobile applications.



1.2 Problem statement

For hydrogen storage technology to succeed, a suitable method for storing hydrogen as an energy carrier should be implemented. Solid-state technology research, specifically metal hydrides, shows promise for practical applications. A few criteria for metal hydrides are the reversibility of hydrogen capacity, low operating pressure or temperature range, high storage capacity, fast reaction kinetics and activation, and low cost of materials. Still, when metal hydrides are exposed to air, they produce oxides, which deteriorate the hydrogen storage capacity. In order to remove the oxides, many cycles of activation are required, followed by heating under vacuum and absorption of hydrogen at high pressures. One of the main challenges of using MH technology is in their preparation routes, especially upscaling. Despite the properties of practically important MH materials are studied well enough [8],[9], the upscale of their preparation processes causes significant changes in the properties of the final product, affecting its component and phase compositions (uniformity) and, in turn, the hydrogen sorption and electrochemical performances. Although attempts to reveal the origin of these effects were undertaken in the past [10], there is still a lack of available systematic information, and the optimization of the upscaled MH preparation processes, as a rule, is performed on an empirical basis when the optimized processes themselves become know-how of the companies involved in MH manufacturing.



1.3 HySA program

Hydrogen South Africa (HySA) Systems was established in May 2007 by the Department of Science and Technology (DST). It is located at the South African Institute for Advanced Materials Chemistry (SAIAMC), hosted by the University of Western Cape (UWC). It is a 15-year program that focuses on (i) the “Use and Displacement of Strategic Minerals”, (ii) ways of harnessing South Africa’s mineral endowments to promote hydrogen economy and renewable energy use, and seeking the most cost-effective and sustainable ways of incorporating PGM-based components in hydrogen fuel cells and other technologies, resulting in commercialisation and a viable industry around mineral beneficiation. The main objective of HySA systems is to develop HFC systems and prototypes and perform technology validation and system integration, particularly in metal hydride-based technologies for hydrogen storage and compression.

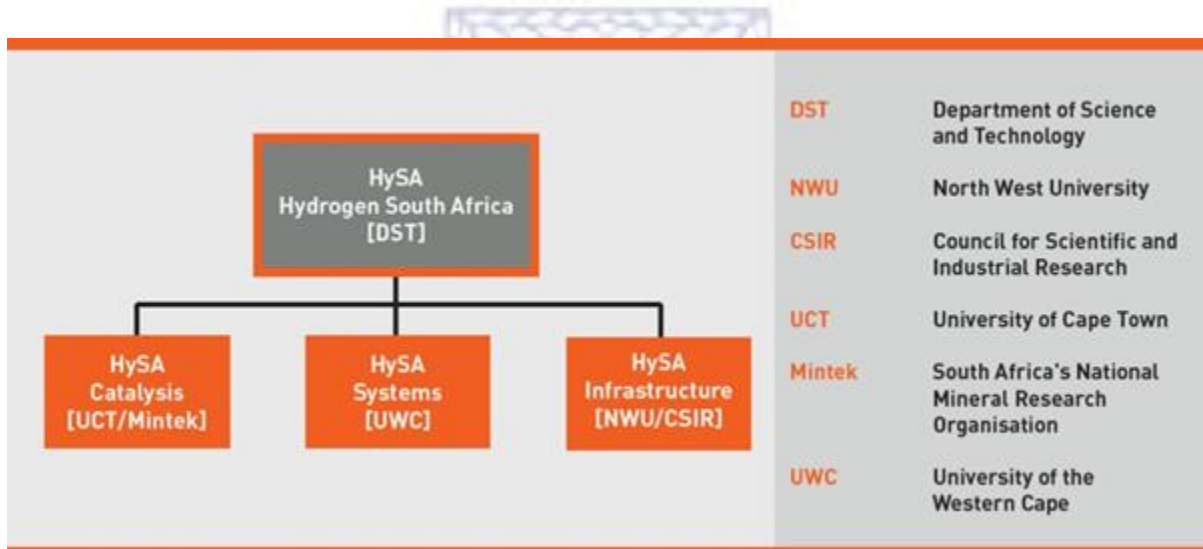


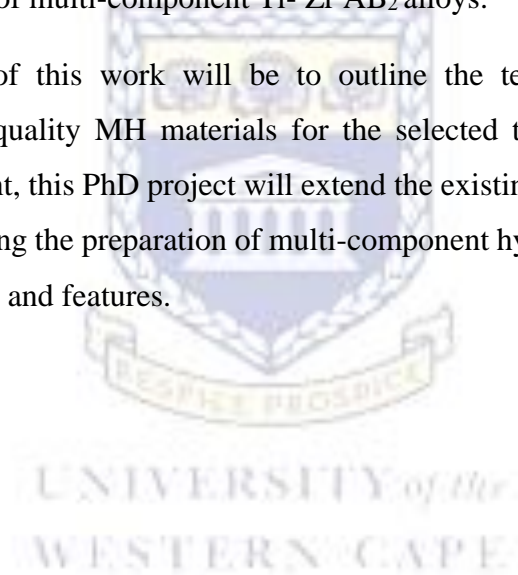
Figure 1. 1: HySA structure [<https://www.hysasystems.com/index.php/about-hysa>]

1.4 Objectives and Aim of Research

The main objective of this research project involved the study of AB₂ metal hydrides, namely Titanium-Zirconium based AB₂ intermetallic compounds by:

- 1.1 Studying different preparation routes such as arc-melting and induction melting.
- 1.2 Comparison of performances due to different preparation routes.
- 1.3 Structural and phase characterization of alloys by various techniques (X-Ray diffraction, Scanning Electron Microscope (SEM), and Energy Dispersive Spectroscopy (EDS)).
- 1.4 Studying the effect of various changes in alloy composition (i.e. Effect of Ferrovanadium on base alloy, the effect of Oxygen substitution on base alloy, etc)
- 1.5 Investigating the reversible capacity and hydrogenation / dehydrogenation rates for hydrogen storage of multi-component Ti- Zr AB₂ alloys.

The main outcome of this work will be to outline the technological procedure for manufacturing good-quality MH materials for the selected target applications. From a fundamental viewpoint, this PhD project will extend the existing knowledge about upscale effects that occur during the preparation of multi-component hydride-forming materials by revealing their origins and features.



1.5 Thesis outline

Chapter 1

Outlines the motivation of the research, the problem statement and the main aims and objectives.

Chapter 2

It highlights the different hydrogen storage materials, such as physical and chemical methods, and the sub-categories of each. The advantages, problems, and areas of solutions are also discussed. This chapter also describes the principles of metal hydride/hydrogen interactions and the instrumentation involved in hydrogen sorption analysis. A review of Ti-Zr based AB₂ materials regarding their lab-scale and upscaling effects, such as preparation procedure, structural and phase effects, various changes in alloy composition, and their hydrogen sorption effects based on these changes, are also discussed

Chapter 3

Chapter three fundamentally serves as a continuation of the literature review but with more emphasis placed on the characterisation techniques employed in the study. It also gives an outline of the different materials that were used in the study.

Chapter 4

The results based on the structural, phase, and hydrogen sorption properties of the Ti-Zr AB₂ multi-component alloy.

Chapter 5

Conclusions and future outlooks.

References

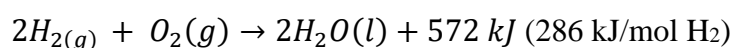
Chapter 2: Literature Review

2.1 Properties of Hydrogen

Hydrogen is the universe's simplest and most abundant element, with a chemical symbol H and atomic number of 1 [11],[12]. It is the lightest element due to its atomic weight of 1,0079 amu and covalent radius of 31,5 pm. It consists of three isotopes, namely Protium (^1H), Deuterium (D or ^2H) and unstable Tritium (T or ^3H) [11],[12]. Hydrogen has a molecular weight of 2,01594 g and a density of 0,08987 kg/m³ at 0°C and 1 atm. Its boiling point and melting point is -253 and -259°C, respectively [12]. The phase diagram of hydrogen shown in Figure 2.1 illustrates hydrogen has a low boiling point. Liquid hydrogen exists only from the triple point to the critical point. The liquid state of hydrogen is maintained between a narrow temperature range between 14 and 33 K. The critical point for hydrogen is of -240°C (33,15 K) and 13 bar [13]. The critical point of a substance is when the liquid and gas phases merge. Above the critical point, hydrogen becomes a supercritical fluid, which is neither gaseous nor liquid. The triple point or three phase point where all three phases are in thermodynamic equilibrium for hydrogen is -259,19°C and 0,077 bar.

At standard temperature and pressure conditions, it is odourless, colourless, tasteless and non-toxic [12]. It consists of two oxidation states (+1, -1), which in turn makes it able to perform both as an oxidizing agent and a reducing agent. It exists in two different spin isomers (parallel and antiparallel) that differ by the relative spin of their nuclei [11]. At standard temperatures and pressure hydrogen gas (H_2) consists of 75% ortho-hydrogen (parallel spin) and 25% para-hydrogen (antiparallel spin) [12].

Hydrogen gas is flammable [12] and has an enthalpy of combustion of -286 kJ/mol, described by the equation:



The auto-ignition temperature is 500°C. When hydrogen burns, a flame detector is required due to the flames of pure hydrogen emitting ultraviolet light and, therefore invisible to the naked eye. Also, hydrogen flames are buoyant in air and causes it to ascend quickly.

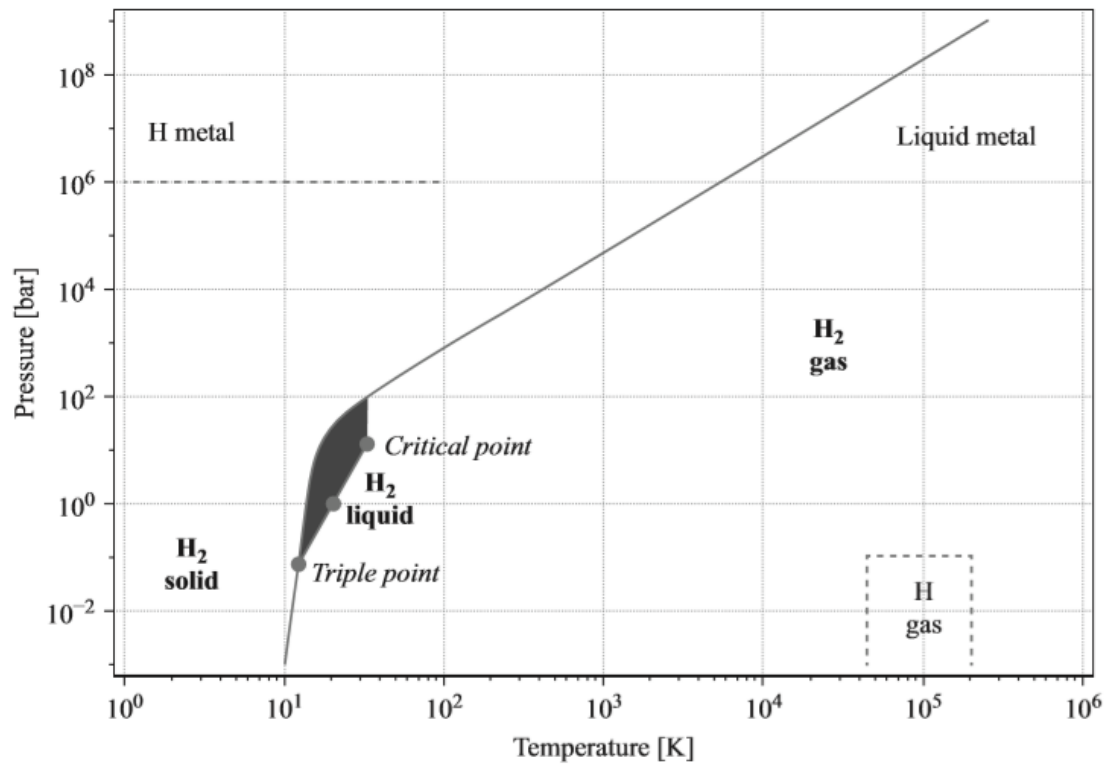
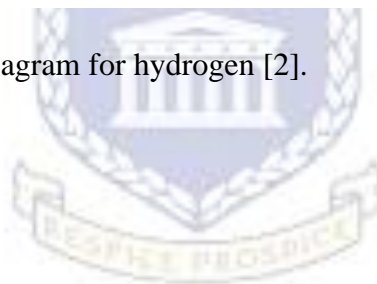


Figure 2. 1: Simplified phase diagram for hydrogen [2].



UNIVERSITY of the
WESTERN CAPE

2.2 Hydrogen Production

“Hydrogen Economy” refers to the primary use of hydrogen as an energy carrier and to overcome the dependency on hydrocarbons as a fuel, which will lead to the reduction of greenhouse gases and, therefore will result in decreased air pollution [2],[14].

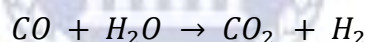
Despite the advantages of using hydrogen as an energy carrier, many barriers exist to fully use hydrogen in the future. Significant advances in hydrogen production, distribution, delivery, storage and conversion of use may overcome the boundaries [2].

There are various methods of producing hydrogen. The two common methods are natural gas conversion and electrolysis. Natural gas conversion process involves steam reacting with methane at temperatures over 800°C in two stages to produce gas stream containing carbon monoxide (CO), carbon dioxide (CO₂) and hydrogen [15].

Stage 1: Steam methane reforming

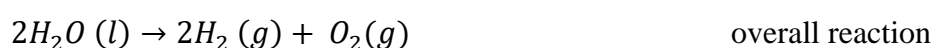
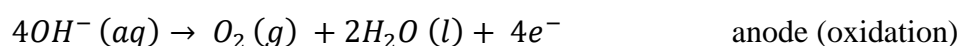
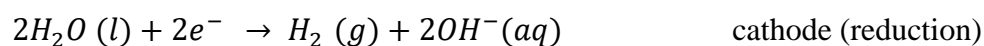


Stage 2: Water gas shift reaction



CO and other contaminants are removed from the gas stream by a process called pressure swing adsorption, resulting in pure hydrogen formation. The disadvantage of this process involves the formation of carbon dioxide (CO₂) released into the atmosphere. Carbon capture and storage research are still ongoing to reduce the amount of CO₂ released [16].

The second technique of hydrogen production is electrolysis [16],[17]. The process involves producing electricity by splitting water into hydrogen and oxygen with a charge passing through the water [15].



The electricity used in this technique is preferably from renewable energy resources such as wind and solar.

2.3 Hydrogen distribution and delivery

Various ways exist to distribute and deliver hydrogen in small or large quantities. These methods include pipelines [16], high-pressure tube trailers or liquefied hydrogen tanks [4], and natural gas blending. The advantages of these methods allow hydrogen to be transported for short or long distances however, high maintenance and cost of the trailers or hydrogen tanks are problematic. The preferred method for transportation of hydrogen are pipelines [4]. There are approximately 2574,95 kilometres (km) of hydrogen pipelines in the United States of America (USA) in operation. Technical concerns related to the pipelines are the embrittlement of the steel and welds used to produce the pipelines. Possible solutions include installation of fiber reinforced polymer pipelines, which are 20% cheaper than steel pipelines.

2.4 Hydrogen storage and conversion

Hydrogen can be stored as a compressed gas in high-pressure tanks or cylinders and as a liquid [4],[18]. As discussed above, there are issues relating to maintenance and cost. Liquid and gaseous hydrogen storage techniques are still in use today on small and large scale; however, these techniques are not suitable for on-board vehicle transportation. A promising method to store hydrogen and use it as an energy carrier is solid state storage in metal hydrides which will be further discussed in Chapter 3.

There are two ways hydrogen can be used to generate power, through direct combustion with air in combustion engines and through an electrochemical reaction with oxygen to produce electrical energy in a fuel cell.

2.4.1 Combustion engines

Hydrogen as an energy carrier can be used in spark ignition engines due to its desirable properties such as low ignition energy, fast flame propagation speed, and wide operational range. When hydrogen is mixed with air it produces a combustible mixture which can be burned in a conventional spark ignition engine, which is below the lean flammability limit of a gasoline/air mixture. The combustion of hydrogen/air produces low flame temperatures, higher engine efficiency and lower exhaust of NO_x emission [19].

2.4.2 Fuel cells

Fuel cells convert chemical energy directly into electricity by electrochemically combining oxygen from air with hydrogen, as shown in Figure 2.2 [4]. Unlike the toxic substances exposed into the atmosphere by fossil fuel combustion, fuel cells do not emit any harmful pollutants that can lead to acid rain or smog-producing substances [4]. Batteries store energy, while fuel cells can produce electricity continuously as long as fuel and air are supplied. There are two types of fuel cells based on operating temperatures:

- a) Low temperature (60-250°C)
- b) High temperature (600-1000°C)

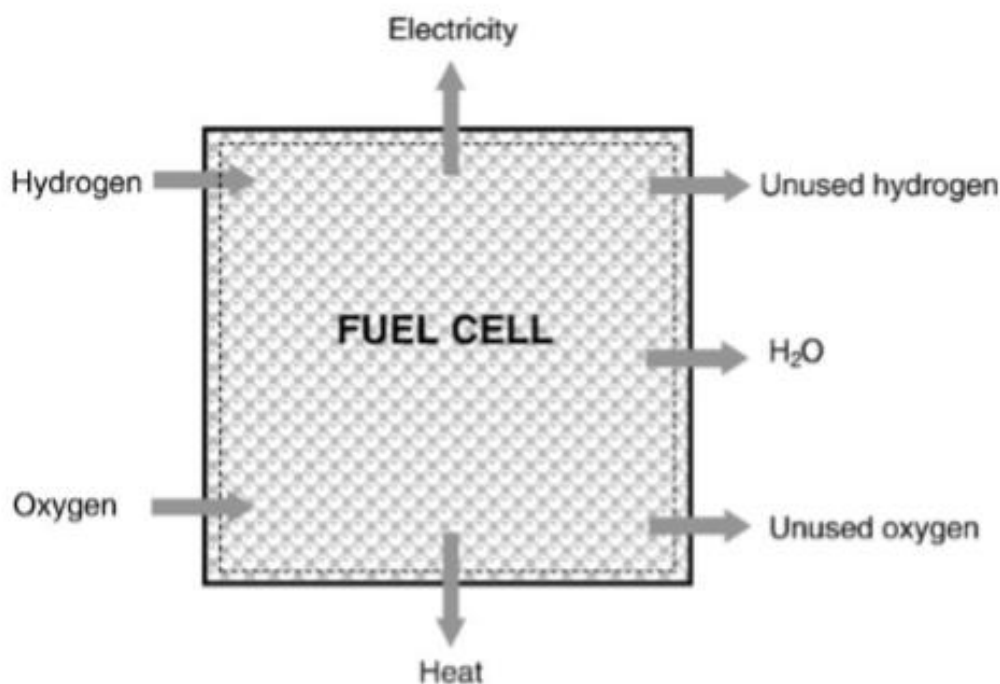


Figure 2. 2:Flows of mass and energy for a general fuel cell [4].

Low-temperature fuel cells generally have quick start times, compact volumes and low weight. Proton exchange membrane (PEM) fuel cells are the most common type [4]. Other types include phosphoric acid, alkaline and direct methanol. Alkaline and PEM fuel cell require a platinum catalyst and pure hydrogen, which is expensive. Phosphoric acid fuel cells are more tolerant to impurities in hydrogen than PEM or alkaline fuel cells and are used for stationary power generation [16]. High-temperature fuel cells are more efficient for electricity generation. Common types for this operating temperature are molten carbonate and solid oxide electrolyte. Regarding transportation, hydrogen fuel cell engines operate at an efficiency of 65%, whereas

petrol-driven car engines at 25%. However, production volumes are low and costs remain high for fuel cells [16]. A summary of fuel cell types is tabulated in Table 2.1.

Table 2. 1: Summary of fuel cell types [16].

Fuel cell type	Operating temperatures (°C)	Applications	Electrical power (kW)	Efficiency (%)
Proton exchange membrane	60-110	Mobile, portable, low power generation	0.01-250	40-55
Alkaline	70-130	Space, military, mobile	0.1-50	50-70
Direct methanol	60-120	Portable, mobile	0.001-100	40
Phosphoric acid	175-210	Medium to large scale power and CHP	50-100	40-45
Molten carbonate	550-650	Large scale power generation	200-100.000	50-60
Solid oxide	500-1000	Medium to large scale power and CHP	0.5-2000	40-72

2.5 Hydrogen storage

Hydrogen storage can be categorised in two sections, physical and physical-chemical storage methods. Physical methods use physical processes to compact hydrogen gas. Hydrogen being stored by physical methods contains hydrogen molecules which do not interact with a storage medium, e.g. storage as compressed gas (in high-pressure cylinders), or hydrogen storage as liquid hydrogen (LH₂). Physical–chemical methods provide hydrogen storage using physical–chemical processes of its interaction with some materials. The methods are characterised by an essential interaction of molecular or atomic hydrogen with the storage environment e.g. hydrogen storage in metal hydrides.

2.5.1 Physical storage methods:

- i. Compressed gas (CGH₂)
- ii. Liquid hydrogen (LH₂)

These methods involve no any bonds between hydrogen and a host compound [7]. The different hydrogen storage materials based on their hydrogen storage capacities are shown in Table 2.2.

i. Compressed gas (CGH₂)

Compressed hydrogen gas is stored in high-pressure cylinders and the pressures up to 350–700 bar [7],[19],[21]. To withstand high pressures above 700 bar, the cylinder materials should be made from carbon composites, which are light and commercially available to withstand high pressures [7],[13]. This method isn't practical due to its low energy density, high operating costs, and the safety issues associated with the high-pressure storage [22]. Compressed hydrogen can be stored either above or below ground level. Above ground storage is more expensive compared to below ground storage. Underground salt cavities in the United Kingdom and United States of America have been implemented to store large quantities of compressed hydrogen due to their low leakage rates, low construction costs, fast withdrawal, injection rates, and minimal risks of hydrogen contamination [23]. The problem with this method is that not all regions have the geological prerequisites for salt cavity storage. Metal containers to store compressed gas may be an alternative solution. It ensures the purity of stored hydrogen and it can be stored anywhere regardless of location. Placing it underground may also be advantageous, it saves space and will be protected against physical impact and weather. However, the cost of metal containers is expensive also, if placed underground, the inspection may become troublesome and special precautions should be taken to protect against corrosion [23].

ii. Liquid hydrogen (LH₂)

The critical temperature of hydrogen is low (-240 °C); therefore, it can only be stored in open systems such as cryogenic tanks at -252°C [2]. The process of liquefaction of hydrogen demands an excess of energy. The process involved increasing the volumetric density and decreasing the temperature.

The loss of hydrogen during dormancy is significant. Dormancy refers to hydrogen in an idle mode [7]. Transportation of liquid hydrogen is easier than transportation of compressed gas. However, the equipment required for liquid hydrogen needs to be specially designed to withstand the low temperatures. Tanks are usually spherical or cylindrical shaped and vacuum sealed. Due to various safety issues, energy consumption and leakage, liquid hydrogen has only been used for special applications [24].

Table 2. 2: Storage capacities of different hydrogen storage materials [25]

Storage method	Materials	Storage capacity (wt.%)	P_{eq}, T
Compressed gas	Energy for compression : ≈ 4 kcal mol^{-1}	13	140 bar, 298 K
Cryogenic liquid	Energy for liquefaction: ≈ 7 kcal mol^{-1}	Size dependent	1 bar, 21 K
Adsorption	Activated carbon	5.5	80 bar, 298 K
	Graphite	4.48	100 bar, 298 K
	SWCNT	4.5	4 bar, 298 K
	MWCNT	6.3	148 bar, 298 K
	CNF	6.5	120 bar, 300 K

2.5.2 Physical-Chemical storage

Materials that interact with atomic or molecular hydrogen through physical-chemical processes could be identified as attractive sorption media for hydrogen. The literature on hydrogen storage materials has shown that the best competitive position in the future for hydrogen storage would be to combine physical and chemical methods. The combination would produce small, medium and large scale hydrogen storage units.

i. Metal hydrides

Metal hydrides store hydrogen in the bulk of the material. It's classified into three categories namely:

- a) Interstitial/Intermetallic hydrides
- b) Chemical hydrides
- c) Complex hydrides

a) Intermetallic hydrides

Intermetallic hydrides contain host materials that are typically two metallic compounds, A and B. Where A forms a stable hydride and B does not form a stable hydride. The common types of intermetallic hydrides include AB, A₂B, AB₂ and AB₅. Examples of some intermetallic hydrides are shown in Table 2.3.

The intermetallic hydride AB have been extensively studied for more than 40 years. TiFe is a popular metal hydride for its large adsorption capacity (1.8-1.9 wt.%), good kinetics for absorption and desorption of hydrogen after activation, equilibrium pressures (5-10 bar) and low cost. TiFe is not easily activated at room temperature. However, V or Mn and/or other transition metals can be replaced or substituted for Fe, improving the activation and the resistance to contamination.

For A₂B, A is from the group IVA element (Ti, Zr, Mg or Hf) and B is a transition metal, often Ni (e.g. Mg₂Ni). Mg₂Ni has good hydrogen capacity and its raw materials are inexpensive. It has a reversible capacity of 3.6 wt.% however, due to the high stability of the bonding [26], the hydride decomposition is high -63.5 kJ/mol H₂. This requires temperatures up to 300°C for desorption at 2.5 bar. A₂B is impractical due to the low operating pressure and high temperature required for desorption [26].

AB₂ metal hydrides have several advantages compared to AB₅ metal hydrides. They have good hydrogen storage capacity and kinetics, long cycling life, low cost, and higher maximum

capacities than AB₅ [7]. The elements A in AB₂ are Ti, Zr, Hf and/or lanthanides (La, Ce, Pr, etc) and B is a variety of transition or non-transition metals with a preference for V, Cr, Mn or Fe.

The hydrogen storage capacities of absorption of the intermetallic hydrides are shown in Table 2.4.

The raw materials of AB₅ metal hydrides are expensive e.g. La [7]. The A components are La, Ca, Y or Zr and B elements are mainly based on Ni, Co, Al, Mn or Ti. The alloys are easy to activate due to not forming protective oxide layers. It has good tolerance towards impurities such as O₂ and H₂O; however, their gravimetric densities are limited to 1- 1.25 wt% reversible capacity.

The hydrogen storage technologies were summarized in Figure 2.3.

Table 2. 3: Examples of intermetallic hydrides [2].

	A	B	Compounds
AB	Ti, Zr	Ni, Fe	TiNi, TiFe, ZrNi
A ₂ B	Mg, Zr	Ni, Fe, Co	Mg ₂ Ni, Mg ₂ Co, Zr ₂ Fe
AB ₂	Zr, Ti, Y, La	V, Cr, Mn, Fe, Ni	LaNi ₂ , YNi ₂ , YMn ₂ , ZrCr ₂ , ZrMn ₂ , ZrV ₂ , TiMn ₂
AB ₅	Ca, La, rare earth	Ni, Cu, Co, Pt, Fe	CaNi ₅ , LaNi ₅ , CeNi ₅ , LaCu ₅ , LaPt ₅ , LaFe ₅
AB ₃	Ce, Y	Ni, Fe	CeNi ₃ , YFe ₃
A ₂ B ₇	Y, Th	Ni, Fe	Y ₂ Ni ₇ , Th ₂ Fe ₇
A ₆ B ₂₃	Y	Fe	Y ₆ Fe ₂₃

Table 2. 4: Hydrogen storage capacities of absorption materials [25],[62].

Storage method	Material	Storage capacities (wt.%)	<i>P_{eq}</i>, <i>T</i>
Absorption	AB; FeTi	1.89	5 bar, 303 K
	A ₂ B; Mg ₂ Ni	3.59	1 bar, 555 K
	AB ₂ ; ZrMn ₂	1.77	0.3 bar, 323 K
	AB ₅ ; LaNi ₅	1.37	2 bar, 298 K
	NaAl	5.6	493 K
	LiAl	7.9	453 K

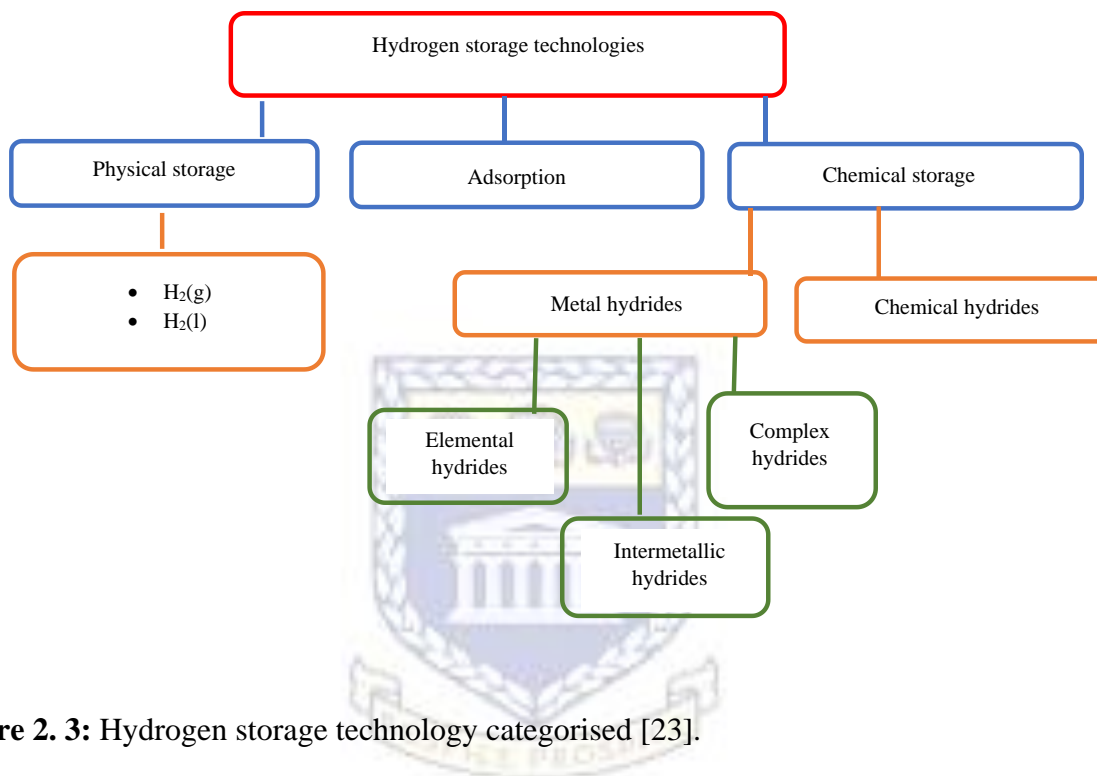


Figure 2. 3: Hydrogen storage technology categorised [23].

b) Complex hydrides

A complex anion is formed when hydrogen is covalently bound to a metal. A cation, which is either an alkali or alkaline earth ion balances the charge of the anion [7]. Complex hydrides include borohydrides (LiBH_4), alanates (NaAlH_4), amides (LiNH_2). These hydrides have high energy densities [27]; however, they decompose irreversibly, that poses a challenge for refuelling on-board [28]. An exception is sodium alanate which can reversibly desorb and absorb hydrogen at presence of Ti-based catalyst and $T \geq 150^\circ\text{C}$ according to the scheme $\text{NaAlH}_4 \leftrightarrow \text{Na}_3\text{AlH}_6 \leftrightarrow \text{LiH} + \text{Al}$ [29].

Borohydrides such as lithium borohydrides (LiBH_4) and sodium borohydrides (NaBH_4) are extensively researched due to their high gravimetric storage capacity at 18.4 wt.%. However, these compounds cannot be used for on-board applications due to the required temperatures for dehydrogenation are greater than 673 K [27]. Alanates such as sodium aluminohydride (NaAlH_4) have a reversible storage capacity of 5.5 wt.% [7] with a total hydrogen content of

7.4 wt.% [30]. Reported results of 4.5 wt.% at temperatures 80-150 °C with a suitable catalyst and hydrogen absorption at 100°C and a pressure of 100 bar. Imides and amides exhibit endothermic hydrogen desorption with partial or full reversibility. The common cation paired with imides/amides is lithium [27]. Lithium adsorbs hydrogen at 1 atm and 558 K.



This reaction reversibly stores 6.5 wt.% of hydrogen however, imides/amides will always be a problem due to the ammonia formed as a by-product during hydrogen release. Ammonia is poisonous for PEM fuel cells and its concentration cannot exceed 0.1 ppm. Its poor kinetic rate during the dehydrogenation process is problematic [27].

c) Chemical hydrides

Chemical hydrides are organic liquids that can be used to store hydrogen indirectly. These organic liquids include compounds such as ammonia borane (NH_4BH_4), methylcyclohexane (C_7H_{14}) and methanol (CH_3OH). These materials possess high theoretical gravimetric weight densities, however these materials are impractical due to their non-reversibility, toxicity and increased pollution [31]. Methylcyclohexane and toluene (C_7H_8) have a three-step rechargeable process for dehydrogenation and hydrogenation. The summarised three steps involve dehydrogenation (catalytic process) to produce H_2 gas on-board, transportation of the dehydrogenation product to a central processing plant while simultaneously refilling the tank with fresh H_2 liquid and lastly, rehydrogenation of the H_2 depleted liquid to its starting material then returned to the filling station [13].



The equation above yields a gravimetric density of 6.1 wt.% H_2 and volumetric density of 43 kg H_2/m^3 .

2.5.3 Adsorption on high surface area materials

i. Zeolites

Zeolites are alumina-silicate crystals composed of SiO_4 or AlO_4 building blocks used in industrial applications involving separation, absorption or adsorption of gases. The properties of zeolites include reversibility, fast kinetics, contain weak van der Waals forces, and their narrow pores, which make it easy to adsorb hydrogen [32]. However, their low gravimetric density is not desirable for practical applications.

ii. Activated carbon

Activated carbon (AC) is produced from carbonaceous material through dry distillation, the pore volume of which can be increased by thermal or chemical activation [25]. Due to their high surface area and weak van der Waals forces enable the physisorption of hydrogen molecules as they get adsorbed and diffuse into the pores of the ACs [25]. Though results have been reported on using activated carbon for hydrogen storage by various methods such as palladium and palladium doping, microwave treatment and grinding, these methods cannot be used as practical applications due to AC possessing low mass density, small pore size that can only hold two layers of adsorbed hydrogen [25]. The highest value of hydrogen adsorption in AC are close to 1 wt.% at 10 MPa.

iii. Carbon materials

Graphite is sp^2 hybridised with a sheet-like structure. It possesses low hydrogen storage capacity due to its small interlayer distance (3.354 Å) and low specific surface area (SSA) [25]. In order to improve the hydrogen capacity of graphite, the interlayer distance needs to be increased [25]. Introducing alkali metals or alkali bonded to organic ligands may improve the interlayer distance in the range 8.7-12.4 Å, however this may result in exfoliation [25]. Ball milling may also increase the SSA by reducing particle size [25].

Carbon nanotubes and nanofibers are popular research topics for hydrogen adsorption for storage applications [25]. Carbon nanotubes are a single rolled graphene layer (SWNTs) and usually, when rolled multiple times, refers to multi-walled nanotube (MWNTs) [25]. To improve the hydrogen capacity of nanotubes, it can be doped with alkali metals such as potassium and lithium [25],[33]. Reported results of 20 wt.% for lithium and 14 wt.% potassium doped MWNTs hydrogen adsorption [25]. Carbon nanofibers are graphite platelets

that are fixed in several alignments with the fiber axis. To improve hydrogen capacity, nanofibers can be purified by removal of amorphous carbon [25].

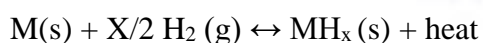
iv. Metal organic frameworks

Metal organic frameworks (MOFs) are synthetic crystalline materials with rigid organic ligands linked to metal containing clusters[34]. They possess structures with pores, channels, big void spaces and a large surface area with thermal stability [7]. MOF-177 can store a minimum of 7.5% H₂ wt .% at 77 K and 110 bar H₂ pressure [35]. Challenges related to capacity, uptake and release of hydrogen, management of heat during refuelling, cost and life cycle impacts the use for practical applications.

2.6 Metal hydride/hydrogen interactions

2.6.1 Hydrogen in metal hydrides

Most of the metals in the periodic table, their alloys or intermetallic compounds, react with hydrogen to form metal hydrides. In this sense, the host metallic system acts like a hydrogen sponge. The bonding between hydrogen and the metal can range from ionic, covalent, as well as multi-centred bonds, and metallic bonding. Metal hydride method of hydrogen storage is based on the process of reversible hydrogen adsorption in hydride forming metals and intermetallic compounds with the formation of metal hydrides (MH) with metallic M–H bonding. In this process hydrogen is placed in interstitials of crystal structure of the matrix of the metal, as an individual, not associated in molecules, H atoms. The process can be described as gas-solid reaction represented by the equation below.



Where M denotes hydride forming metal or intermetallic compound; s, g denote the solid and gas phase, respectively. This reaction is usually exothermic and reversible. Heating of the hydride causes hydrogen desorption. Hydrogen gas or hydrogen ions from an electrolyte is used to charge the hydride. If hydrogen is loaded from gas phase, several reaction stages of hydrogen with metal would occur, shown in Figure 2.4. The process involves the interaction of the hydrogen molecule approaching the metal surface is the Van der Waals force, leading to the physisorbed state (Figure 2.4(a and b)). In the next step, hydrogen has to overcome an activation barrier for the formation of the hydrogen-metal bond and for dissociation. The height of the activation barrier depends on the chemical composition of the surface. When hydrogen atoms become chemisorbed (Figure 2.4(c)), it shares its electron with the metal atoms at the

surface. After dissociation on the metal surface, the H atoms have to diffuse into the bulk to form a M-H solid solution, commonly referred to as α -phase (Figure 2.4(d)). The thermodynamic aspects of hydride formation from gaseous hydrogen are described by pressure-composition isotherms.

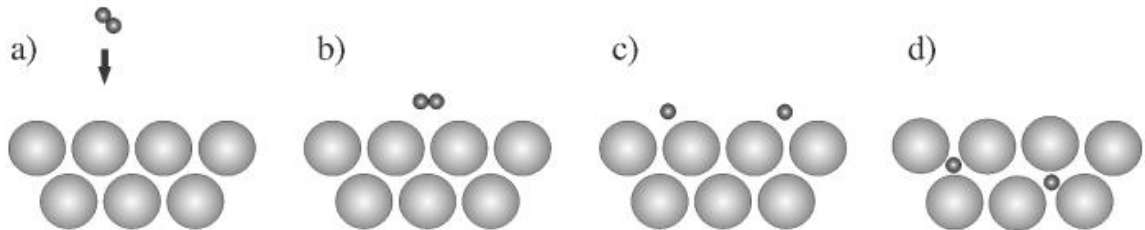


Figure 2. 4: Reaction of a H₂ molecule with a storage material: a) H₂ molecule approaching the metal surface. (b) Interaction of the H₂ molecule by Van der Waals forces (physisorbed state). (c) Chemisorbed hydrogen after dissociation. (d) Occupation of subsurface sites and diffusion into bulk lattice sites [36].

2.6.2 Pressure Composition Temperature Isotherms

Pressure-Composition-Temperature (PCT) Isotherms are used to identify various hydride phases of the alloy compounds. It describes the relationship between the hydrogen equilibrium pressure and the amount of hydrogen dissociated into the solid phase at fixed temperatures. In Figure 2.5 shows a typical PCT plot. In an α -phase, hydrogen atoms form a diluted solid solution in the host metal [2],[3],[37]. As hydrogen pressure increases, more interactions occur between the metal and hydrogen. This leads to nucleation and growth of a new hydride, β -phase [2],[3]. The plateau present relates to both phases co-existing ($\alpha+\beta$) [2],[3]. The hysteresis is the difference between the absorption and desorption path in a PCT isotherm, shown in Figure 2.6. The plateau pressure for absorption, P_a , is greater than the plateau pressure for desorption, P_d . The hysteresis loss of energy is calculated from the ratio P_a/P_d . The amount of hydrogen which corresponds to the fully saturated alloy is referred to as its maximum capacity. For the removal of hydrogen from the metal hydride, pressure decrease below desorption plateau pressure (P_d) is required. The width of the plateau section is the reversible capacity of the metal hydride proportional to the amount of hydrogen reversibly absorbed in and desorbed from the material. The hydrogen storage capacity of the material per unit weight can be calculated by the equation [38]:

$$wt \% = 100 \times \left(\frac{M_H}{M_S \times M_H} \right)$$

Where M_H is the mass of hydrogen, M_S is the mass of the sample.

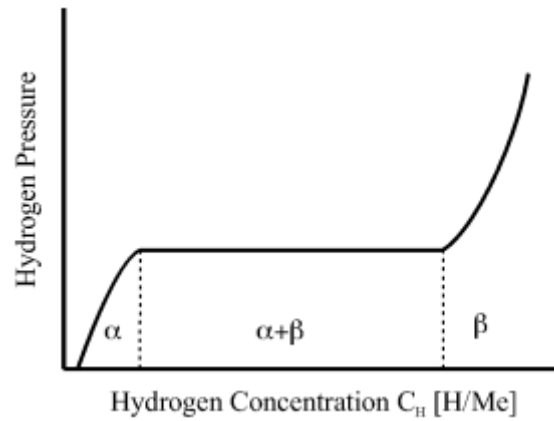


Figure 2. 5: A Pressure-Composition-Temperature Isotherm (PCT) plot [36].

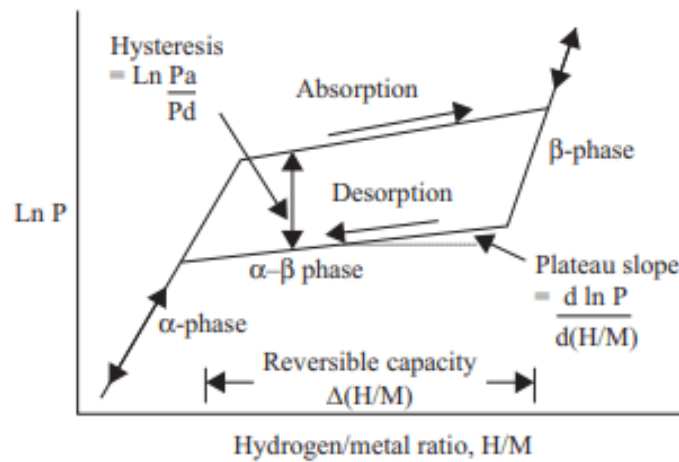


Figure 2. 6: A PCT plot illustrating absorption and desorption [2].

2.6.3 Thermodynamics

The PCT diagram in Figure 2.7 shows the effect of temperature on PCT curves. As the temperature is increased from T_1 to T_3 , the plateau width is reduced until it reaches the critical temperature, T_c . Above T_c there is no plateau present [3].

The van't Hoff equation[2] expresses the relationship between the plateau pressure and temperature:

$$\ln P = \frac{\Delta H}{RT} - \frac{\Delta S}{R}$$

Where P is the equilibrium pressure at temperature, T .

ΔH and ΔS are standard enthalpy and entropy changes of the hydriding/dehydriding reaction and R is the gas constant (8.3145 J/mol K). Using the van't Hoff equation, the gradient of the line is used to give ΔH and the intercept (when, $1/T=0$) the ΔS .

$$\Delta H = Rm$$

$$\Delta S = -Rc$$

where m and c are coefficients of equation $y=mx+c$ ($x=1/T$, $y=\ln P$) describing the van't Hoff plot.

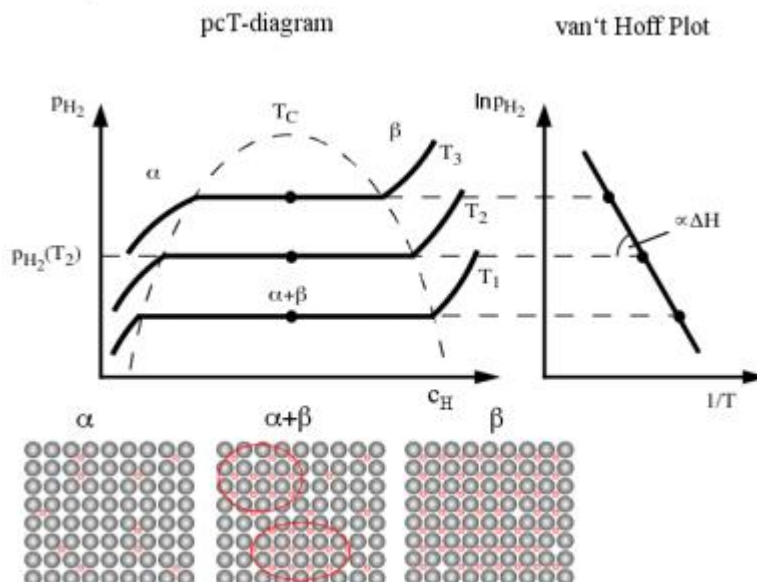


Figure 2. 7: PCT diagram(left) at different temperatures ($T_1 < T_2 < T_3 < T_4 < T_c$). The α -phase is the solid solution phase, the β -phase the hydride phase. Within the (α - β) two phase region both

the metal-hydrogen solution and the hydride phase coexist. The van't Hoff plot diagram (right) [36].

2.6.4 Heat Transfer

A combination of significant heat effects of the hydrogen absorption (exothermic) and hydrogen desorption (endothermic) by metal hydrides (up to 30–40 kJ/mol H₂) and poor effective thermal conductivities of the MH beds (as a rule, below 1 W/(m K)) results in the fact that the charge and discharge rates of the MH reactors are limited by the heat transfer in the MH bed [39]. That is why, to store hydrogen in metal hydrides, efficient heat management is required. During the refuelling, heat is removed, whereas, during discharge, it needs to be supplied [40]. Heat transfer for refuelling is more demanding than discharge due to refuelling time being short while discharging time extends for a few hours [40]. The heat transfer performance of hydride containers can be improved by decreasing their diameter or by augmentation of heat transfer inside the MH bed (e.g., using Al foams, internal fins) [2], [39].



UNIVERSITY of the
WESTERN CAPE

2.7 Phase structure of AB₂ alloys

As previously discussed, there are various ways to store hydrogen, however these methods aren't favourable due to low energy densities and high cost. Storing hydrogen in metallic materials has been the focus due to its high storage capacity, particularly AB₂ alloys [41]. These alloys demonstrate:

1. High energy density [6]
2. Flexibility in design [6]
3. Contain multi-phase and multi elements [6]
4. Easy activation and low-cost
5. Longer electrochemical charge-discharge cycle life [42]

Laves phases form the largest group of intermetallics and hence have a wide range of properties. There are typically three different types of Laves phase, C14, C15, and C36 (Figure 2.8). They are all composed of the same A₂B₄ unit block but differ in stacking sequences, shown in Table 2.5. Metal hydrides exhibit C14 and C15 phases, whereas C36 exist between C14 and C15 phases. Alloys containing C14 and C15 crystal structures serve as hydrogen storage alloys and electrode materials. Alloys containing C14 crystal structure were used earlier when alloy composition design was focussed on capacity and cycle stability [43].

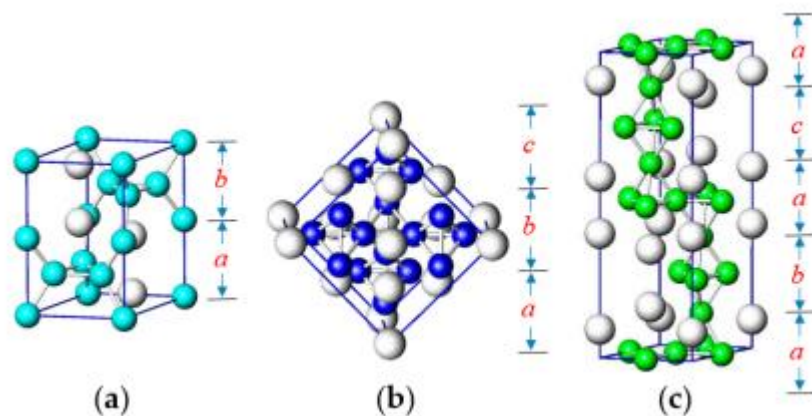


Figure 2. 8: Schematic of (a) C14 (hexagonal), (b) C15 (cubic), and (c) C36 (rhombohedral) crystal structures [43].

Table 2. 5: Laves phases with stacking sequences [43].

Phase	Crystal structure	Stacking sequence
C14	Hexagonal	<i>a-b-a-b</i>
C15	Cubic	<i>a-b-c-a-b-c</i>
C36	Rhombohedral	<i>a-b-a-c</i>

2.8 Zr-based AB₂ alloys

Zr based AB₂ alloys have been recognized to be the ideal hydrogen storage material due to their relatively good hydrogen storage capacity, fast kinetics, long cycling life, and low cost. However, they are too stable at room temperature and sensitive to gas impurities. The hydrogenation characteristics of Zr based Lave phase compounds such as ZrV₂ [44], ZrCr₂, ZrMn₂, ZrFe₂ [45], [46], [47], and ZrCo₂ have been extensively studied due to their ability to absorb large quantities of hydrogen; nonetheless, the hydrides that are formed are too stable to be of practical importance. Hence, the partial substitution of A (Ti, Y, La, Ce) or B (Mn, Co, Cr, Fe, Cu, Ni etc.) component by any transition metal, creates a multi-component system.

2.9 Ti - Zr based AB₂ alloys

The hydrogen storage characteristics of Ti-based AB₂ alloys can be improved by several methods such as:

- 1) Adding alloying elements or components with catalytic effects
- 2) Modifying the surface properties of the hydrides
- 3) Employing new preparation methods including; smelting methods, mechanical alloying, rapid solidification methods, severe plastic deformation, physical vapour deposition.

This section will highlight Ti based AB₂; where (A= Ti, Zr, B=Mn, Cr, Cu, Fe, V, Co, etc.) alloys with regards to their performance in an upscale preparation (e.g. ball-milling/mechanical alloying, induction melting etc.), and a further look into the performance of Ti-Zr based AB₂ alloys with regards to changes in different variables (e.g. effect of; O, FeV, Cr, Fe, V, etc.) when prepared by arc melting.

2.10 Phase structure and hydrogen sorption characteristics with regards to upscaling techniques

i. Ball milling

High energy ball milling is a technique widely used in the field of metal hydrides. It provides homogeneous mixtures of different powders with a reduction in particle size and crystallites, leading to a faster reaction with hydrogen. It can be used to synthesise materials, re-activate materials, and also allow for large scale production [48].

Researchers have found that the method modifies the surface of the alloy by creating fresh surfaces to improve electrochemical properties and hydrogen sorption characteristics. In addition, with the poor activation of Ti-based AB₂ alloys, the ball milled method facilitated faster activation [49].

It has been reported that with increased ball milling time, the diffraction peaks broadened due to the refinement of crystallite size. The ball milled powders may lose their crystalline characteristics, due to conversion into the amorphous phase during the milling process [50]. The effect of heat treatment on ball milled powders with regards to their diffraction peaks show higher intensity and have smaller widths. This is due to the rising grain size of powder crystallites and modified lattice strain due to recovery and recrystallization during annealing [51].

The use of rare earth metals to form composites (AB₂-x% RE₅) has been shown to improve the electrochemical properties and also no changes to the basic structure of the Laves phase were reported [52], [53].

A thesis published in 2011 [54] explained even though ball milling contained advantages with regards to facilitating faster activation by creating fresh surfaces, the problems associated with the technique, such as time consumption, high energy requirement for synthesis of alloys, increased temperature due to the sticking of powders to vessels, and contamination of the material which may impact the structure and properties of the end product, limits the use of this method for upscale manufacturing of metal hydride alloys. A summary on Ti-Zr based AB₂ alloys prepared by ball-milling is tabulated in Table 2.6.

Table 2. 6:Summary on ball milled variables of Ti-Zr based AB₂ alloys

Composition	Speed (rpm)	Ball to powder ratio	Milling time (hrs)	References
Ti _{0,36} Zr _{0,64} (V _{0,15} Ni _{0,58} Mn _{0,20} Cr _{0,07}) ₂	250	20:1	1, 3, 5	[49]
Ti _{0,9} Zr _{0,2} Mn _{1,6} Ni _{0,2} V _{0,2}	200	20:1	30 min 90 min 180 min 320 min	[50]
Ti _{0,9} Zr _{0,1} Mn _{1,2} V _{0,4} Cr _{0,4}	300	15:1	5, 10, 20	[55]
Ti _{0,72} Zr _{0,28} Mn _{1,6} V _{0,4}	200	15:1	4	[51]
Ti _{0,9} Zr _{0,2} Mn _{1,5} Cr _{0,3} V _{0,3} + La-Mg alloy	400	20:1	2	[56]
Ti _{0,9} Zr _{0,2} Mn _{1,5} Cr _{0,3} V _{0,3} + La alloy	400	20:1	2	[53]

ii. Rapid solidification techniques

Rapid solidification is a technique used to improve the properties of the alloys by modifying their microstructures, extending solid solubility limits and forming metastable constituent phases, and enhancing their hydrogen sorption properties [57].

a) Melt spinning

Melt spinning involves a molten metal casted from the crucible and ejected through a spinning drum. It is then rapidly cooled to form a ribbon with a specific atomic structure. It has previously been reported that the C14 phase abundance of Ti-based AB₂ alloys becomes higher as the wheel rotation speed increases. This suggests that the C14 phase is more likely to form at higher solidification rates compared to the C15 phase. Additionally, with increased rotation speeds, the grain size gradually decreases, and the formation of dendrite microstructures are introduced [57].

Diffraction peak broadening and reduced peak intensity were found for melt spun alloys compared to cast and annealed alloys (Figure 2.9). The broadening of the diffraction peaks is primarily attributed to the decrease in the crystallite size and an increase in residual strain during rapid solidification [58].

However, due to the high solidification rate, the structure of the fibers may be poor. Also, due to the high input energy, the temperature needs to be controlled; hence extensive knowledge of the procedure would be advantageous, which may also be useful when doing regular maintenance.

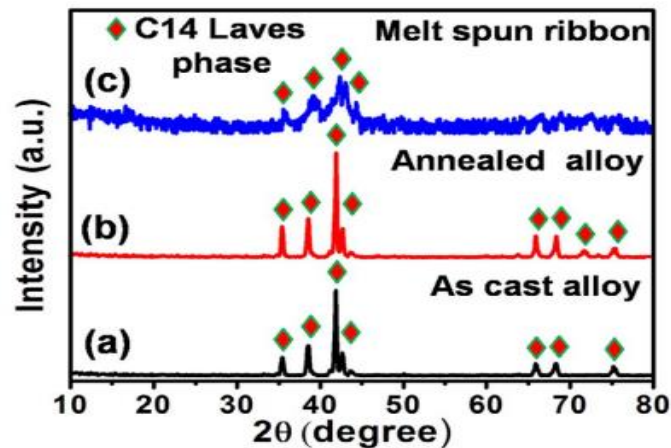


Figure 2. 9: XRD patterns of Ti-Zr-V-Cr-Ni high entropy alloy, (a) as cast, (b) annealed, and (c) rapidly solidified ribbon [58].

b) Gas atomisation

Another rapid solidification method is gas atomisation (GA). It is a process that creates a melt stream from molten metal, which is then impinged with a strong flow of an atomisation gas that causes dispersion and creates particles or droplets. These particles then fall and cool onto a substrate or metal plate [59].

The advantage of this method is that it reduces production costs by cutting out the pulverization process. The spherical shape of the GA particles increases packing density and reduces stress created in the alloy particle during hydride-dehydride process to enhance cycle life [59].

However, the limitations of the GA process may include a thicker surface oxide layer hindering the activation process and a higher oxygen content in the bulk to reduce hydrogen storage capacity [60].

High-temperature annealing ($>850^{\circ}\text{C}$) was shown to reduce the thickness of the surface oxide layer, but also segregates out the oxygen impurity in the bulk of the gas-atomized powder. In addition, it enhances the properties of C14 Laves phase [60] including the electrochemical ones [61].

c) Plasma spraying

Plasma spraying (PS) involves a primary gas (e.g. Argon) and a secondary gas (e.g. H₂), which is ionised while passing between a tungsten cathode and copper anode. A plasma with an electron temperature of approximately 15 000 K is produced. The particles of powder mixture injected into the plasma are melted and sprayed onto the substrate. The particles solidify rapidly on the substrate, forming lenticular splats [62]. The use of vacuum plasma spraying (VPS) on Ti-Zr based AB₂ alloys is limited. A study comparing VPS and Induction melting of Ti-Zr based AB₂ alloy was reported in [51] (Figure 2.10). The author concluded that both methods produced a hexagonal C14 Laves phase, however the intensity of the diffraction peaks were higher for the induction melted alloy due to better solvation, and the phase ratio was higher for the VPS alloy due to the higher cooling rate.

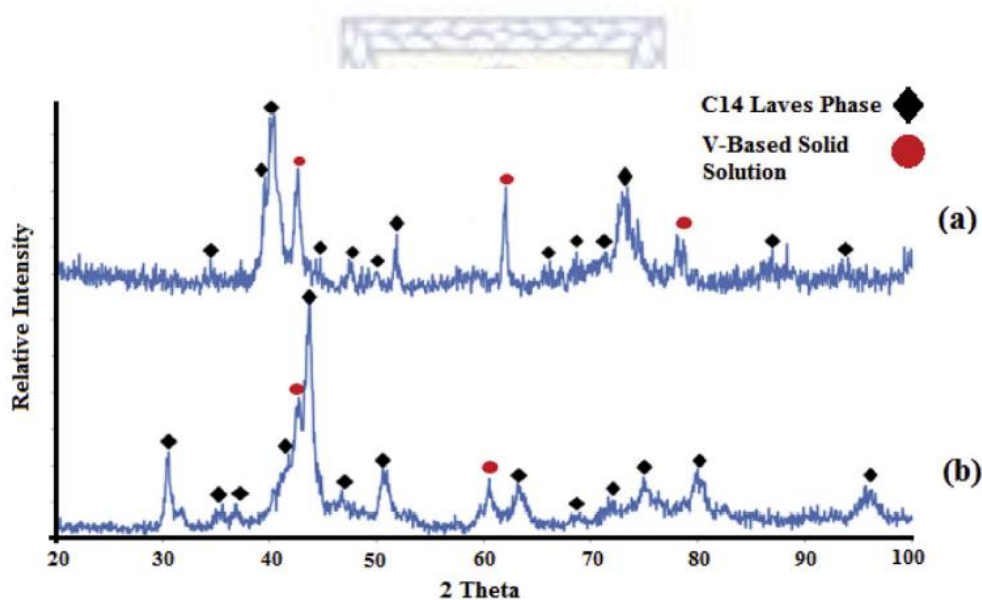


Figure 2. 10: XRD patterns of Ti_{0.72}Zr_{0.28}Mn_{1.6}V_{0.4} alloy produced by (a) vacuum copper boat induction melting, (b) vacuum plasma spraying [51].

iii. Induction melting

Unlike arc melting, which is performed at small scale, vacuum induction melting (VIM) [63], [64] is performed at a large scale. The basic principle involves melting an alloy, under vacuum or inert gas, placed in a crucible with heating and cooling coils and refractory lining. An electric current is passed through a set of induction coils, which creates a magnetic field that induces a current in the charge material. The magnetic field causes the molten material to stir, which enables homogenous composition. The advantages of vacuum induction melting include, easy operation, precise temperature control, low level of environmental pollution from dust output, removal of undesired trace elements with high vapour pressures, etc.

Despite its advantages, the main problem with this preparation route is the crucible melt interaction, which results in the contamination of the product and shortens the crucible service time [65]. Since molten Ti metal requires high operating temperatures ($>1600^{\circ}\text{C}$), the crucible material has to be resistant to reacting with the melt, and also durable enough to withstand the high temperature, so no crucible-melt interaction must occur [66]. Therefore, the crucible material should have higher melting and softening temperatures than molten Ti.

Reported studies on traditional ceramic crucibles such as Al_2O_3 [10], [67], MgO [68]–[70], MgAl_2O_4 [71]–[73] are used in the preparation of Ti-Zr based AB_2 alloys. The indicated materials above are relatively inexpensive, and have low thermal shock. Therefore, it is important to select crucible materials that have high thermal shock resistance, which in turn exhibit low thermal expansion coefficients and high thermal conductivity [66].

To overcome the crucible-melt interaction, possible solutions are to increase the thermal shock resistance of the crucible material to the interaction with the melt (e.g. protective coatings) or elimination of the contact of the melt with the wall of the cooled crucible (levitation melting) [65].

Protective coatings usually contain a thin inert material that is either plasma sprayed or slurry painted. Ytria (Y_2O_3) is a common inert material as it displays good thermal shock resistance and chemical inertness towards molten Ti. However, Y_2O_3 has poor shelf life of its slurry, poor sinterability, low adhesion to many substrates, and cracking due to thermal shock for thick coatings [66].

Levitation induction melting (LIM) or cold crucible melting (CCM) is a form of producing alloys under the same principle of induction melting, however there are no crucible-melt interactions taking place. This process instead calls for an immediate solidification by a cold

crucible wall. It also ensures that there are less or no contamination from other materials. With regards to phase structure, a number of researchers have reported of a single hexagonal C14-type Laves phase present in Ti-Zr based AB₂ alloys [74]–[78].

A slight modification of the CCM is copper boat induction melting (CBIM). The only reported study that utilizes this method was Kazemipour *et al.*, [51] for Ti-Zr based AB₂ alloys.

2.11 Phase structure and hydrogen sorption characteristics in Ti-Zr based AB₂ alloys by arc melting

Alloys are formed by melting metals used by arc melting. The process involves using an electric arc to heat a sample of material to very high temperatures, typically above its melting point. The heat generated by the arc causes the material to melt and form a molten pool. Arc melting is typically carried out in a specialized apparatus called an arc furnace, which consists of a refractory-lined chamber filled with high-purity inert gas (Argon or Helium) with a pair of electrodes. The sample of material is placed on one of the electrodes (water-cooled copper hearth), and an electric arc is struck between the electrodes. The arc generates intense heat, which melts the material and forms a molten pool in the chamber. The process can be used to alloy different metals together, creating new materials with specific properties. Arc melting is primarily used for lab scale and produces alloys with higher purity than induction melting.

The phase structure of Ti-based AB₂ alloys usually consists of either a hexagonal C14-type or a cubic type C15 Laves phase. Elliot and Rostoker [79] explained the relation between the average number of outer electrons (ANOE) and phase structure, (a) when ANOE is less than 5.4 and A site is Ti, the Laves phase cannot form while the C15 phase exists for Zr atom, (b) when ANOE is in the range of 5.4-7, the C14 phase structure can form for Ti and Zr, and (c) when ANOE is more than 7, the C15 Laves phase exists for Ti and Zr atom. This relation was used by Kandavel and Ramaprabhu [80] to determine the phase formation of the Ti-Zr based AB₂ alloy. The calculated values were between 6.43 to 6.71, indicating a C14 Laves phase.

Kandavel *et al.*, [81] and Cao *et al.*, [82], reported on diffraction patterns that shifted towards lower angles, indicating lattice expansion, when increasing Zr content, since the atomic radius of Zr (1,602 Å) is higher than that of Ti (1,462 Å).

On the other hand, Tu *et al.*, [83] reported on diffraction patterns that shifted towards higher angles, when Mn content was increased, which indicated a lattice shrinkage of the C14 phase.

The unit cell volume was decreased with Mn substitution and further decreased with the addition of Ni. However, the addition of V lead to an increase in the unit cell volume.

Authors have found that with the increase in Zr content, decreased the plateau pressure and hysteresis [82], [84]–[86], while the increase in Cr content the equilibrium pressure hysteresis of dehydrogenation improves, the plateau pressures of dehydrogenation decreases, and the hydrogen storage capacity decreases [78]. It was reported that Fe content should be controlled, as too much will increase the hysteresis, plateau pressure and plateau slope, which would negatively impact the reversible hydrogen capacity [84], [87].

Chuang and Chan [41] found that the partial substitution of Cr by Ni, reduced the cell volume and increased the plateau pressure, however the addition of V decreased the plateau pressure. In another study published by Hagström *et al.*, [88], partial substitution of Mn by V eliminated the hysteresis at 20 °C, however presented a wider α -phase and increased slopes.

Since high purity Ti and V are expensive, Ulmer *et al.*, [89] studied an alternative route of using a less expensive with low purity Ti sponge and FeV instead. They found that the maximum hydrogen storage capacity absorbed was 2 wt.% for the base alloy with high quality Ti and V, and after substitution with Ti sponge and FeV it decreased to 1.7wt.%.

2.12 Limitations of AB₂ metal hydride alloys

Although Ti-Zr based AB₂ alloys offer quite a wide range of attractive features, there are drawbacks such as surface poisoning in hydrogen gas streams. Nakagawa *et al.*, [90] and Hanada *et al.*, [91] studied the effect of CO₂ on Ti-Zr based AB₂ alloys by partial substitution of varying amounts of Co, Ni, Fe, and Cu. They found that increasing the Fe concentration showed an impact on CO₂ resistance.

Since the surface of Ti-Zr based AB₂ alloys are easily oxidized by either forming Zr and/or Ti oxides, which hinder the catalytic dissociation of H₂→2H in gas-solid reactions or H⁺ in electrochemical reactions. In order to remove the oxide layer, surface modifications such as fluorination solution containing Ni ion [92], boiling KOH alkaline solution, or with solution of NH₄F/NiCl₂. Even though these procedures effectively remove the oxide layer and initiate faster activation, high rate discharge ability, and cycle durability, they require severe conditions such as temperature, concentration, etc., which may damage the alloy electrode.

Alternatively, modification of the alloy composition was proven to improve the electrochemical performance of the alloy electrodes. Thus, the addition of small amounts of

rare earth elements such as Lanthanum (La) was shown to accelerate initial activation and surface protection against air and water exposure in Ti-Zr based AB₂ alloys research. This was mainly due to La being insoluble in AB₂ matrix; however, it forms small La-Ni particles on the surface of the alloy. This allows for a porous and H₂ transparent oxide and boundaries between La rich particles and the AB₂ matrix for quick H₂ absorption [93], [94], [95], [96].

2.13 Conclusion

The purpose of this literature review was to evaluate the upscaling effects of Ti-Zr based AB₂ metal hydride materials based on;

- Preparation techniques
- Structural and phase changes due to the different preparation methods employed
- Modifications to crucible materials

In addition, lab scale effects based on arc melting preparation of Ti-Zr based AB₂ metal hydride materials were also reviewed and focussed on;

- Structural and phase changes
- Hydrogen absorption capacities when modifying the alloy composition
- Limitations

Based on the reviewed articles, Ti-Zr based AB₂ metal hydrides, are advantageous to use for hydrogen storage based on;

- relatively good hydrogen absorption capacity
- inexpensive raw materials
- good kinetics

However, during upscaling, these materials suffer from crucible-melt interaction, affecting the hydrogen storage capacities. Ti-Zr based AB₂ alloys are sensitive to surface poisoning such as CO₂, which limits their full capacity. Some modifications to overcome this boundary include surface modifications, but this proved to cause damage to the alloy. Instead, modifying the alloy composition by adding a small amount of rare earth metal proved to be a suitable option for improving the sensitivity to surface poisoning.

Chapter 3: Preparation of alloys and Characterisation techniques

3.1 Alloy preparation techniques

3.1.1 Arc melting

The alloys with a composition of (A= $\text{Ti}_{0.85}\text{Zr}_{0.15}$, B= $\text{Cr}_{0.2}\text{Mn}_{1.22}\text{Ni}_{0.22}\text{V}_{0.3}\text{Fe}_{0.06}$) were prepared via arc-melting (Figure 3.1) at the Institute of Energy Technology (IFE), Norway. The elements were weighed out individually to produce a total mass of 10g. It was then placed onto a water-cooled copper hearth and then flushed with Ar to remove air. The alloys were melted three times to provide homogeneity. The alloys were heat treated afterwards at 950°C for 19 hours. This alloy will serve as the base alloy.

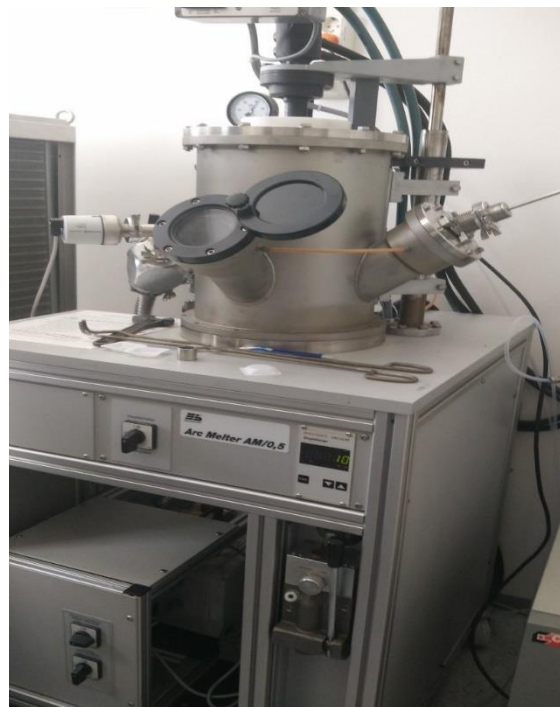


Figure 3. 1: Arc-melter at IFE,Norway.

3.1.2 Induction melting

Ti-Zr based AB_2 alloy was prepared by induction melting at South African Institute of Advanced Material Chemistry (SAIAMC). The alloy was prepared by induction melting of the metallic components under Ar atmosphere. The starting components were all purchased from South African suppliers with a purity of $>98\%$; these included electrolytic Mn (low oxygen flake), Ti (grade cut-offs), Zr (sponge), Cr (pieces), Ni (powder), and Ferrovandium (powder; 80 wt.% V). wt.% La was added to the charge to assist with the activation of the alloy according to the recommendation found in [97]. The samples ($m = 100$ g) were prepared in SM 10 K VHT vacuum induction melting furnace with a crucible capacity of 200 g. Two types of crucibles were used: ceramic aluminosilica ($Al_2O_3 + SiO_2$) and graphite, ~ 150 g in weight each. Each crucible was placed into aluminosilica crucible of the bigger size (Figure 3.2).

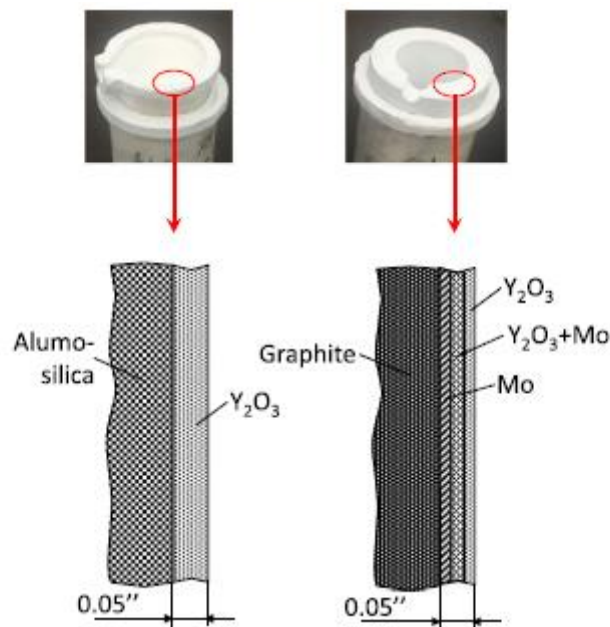


Figure 3. 2: Images and schematic cross-section of the Y_2O_3 – coated crucibles [98].

To minimise interaction between the melt and the crucible material, both crucibles were coated inside by the deposition of a protective coating whose surface contacting the melt was yttria (Y_2O_3). In both cases, the total coating thickness was 0.05 inches.

The alumo-silica crucible was directly spray-painted with Y_2O_3 slurry—pure yttria powder suspended in 5% aqueous solution of caboxylmethylcellulose (CMC) stabiliser. The coated crucible was dried in an oven at $T = 80\text{ }^\circ\text{C}$.

The coating of the graphite crucible had three layers, which were shown to provide good adhesion of the external Y_2O_3 refractory layer to the graphite substrate. The inner molybdenum metallic layer was applied as a diffusion barrier to carbon, and the intermediate $\text{Mo} + \text{Y}_2\text{O}_3$ layer was used to absorb thermal shocks. Spray painting was used to first coat Mo slurry (powder with particle size below 5μ suspended in the CMC solution), then $\text{Mo} + \text{Y}_2\text{O}_3$ slurry, and finally Y_2O_3 slurry, with drying in an oven after each stage at $T = 80\text{ }^\circ\text{C}$. The CMC was vaporised during pre-heat of the crucible before the melting.

The charge was loaded into the Y_2O_3 lined alumo-silica- or graphite-based crucible, which was then placed into the vacuum furnace chamber, followed by flushing the chamber three times by evacuation to 10–3 mbar and Ar refilling (0.3–1 bar). After flushing, the vacuum furnace chamber was filled with Ar (1 bar), and the electric power supplied to the inductor was gradually increased until the complete melting of the charge was visually observed. The charge was maintained in the molten state at $T = 1600\text{ }^\circ\text{C}$ – $1800\text{ }^\circ\text{C}$ for 1 min.

3.2 Characterization of alloys

3.2.1 X-ray Diffraction

X-ray diffraction (XRD) is a non-destructive tool to analyse information about the structure of crystalline materials from liquids, powders and solids. The process involves an incident beam of monochromatic X-rays generated in a cathode ray tube (CRT) by heating a filament to produce electrons that are then accelerated and directed to the target material. The interaction between the target material and the X-rays results in constructive or destructive interferences. X-rays are produced by constructive interferences that are detected, processed and counted. This process of diffraction of X-rays by crystals is described by Bragg's equation:

$$n\lambda = 2d \sin \theta$$

where:

n = integer

λ = characteristic wavelength of the X-ray source

d = interplanar spacing between rows of atoms

θ = the angle of the X-rays with respect to the plane of atoms (diffraction angle)

In this research, the alloys phase composition was determined by XRD using Bruker D2 Diffractometer; Cu-K α radiation ($\lambda_1 = 1.5406 \text{ \AA}$, $\lambda_2 = 1.5444 \text{ \AA}$, $\lambda_2/\lambda_1 = 0.5$, $2\theta = 15\text{--}90^\circ$). The XRD data was further processed by Rietveld full-profile analysis using GSAS software. A standard α -Al₂O₃ sample was used to determine the instrumental contribution into peak profile parameters. During refinements, the Gaussian profile parameters (GU, GV and GW) were fixed (kept the same as for the Al₂O₃ standard), and only two Lorentzian profile parameters were refined, LX (size broadening) and LY (strain broadening).

The following reference data were used for the full profile analysis with GSAS software:

- C14-AB₂ Laves phase intermetallic (Ti_{0.95}Zr_{0.05}Mn₂): space group $P6_3/mmc$ (194), $a = 4.826 \text{ \AA}$, $c = 7.921 \text{ \AA}$, unit cell volume 159.8 \AA^3 [99].
- (Ti,Zr)O₂ mixed oxide: space group $Pbcn$ (60), $a = 4.7447 \text{ \AA}$, $b = 5.0119 \text{ \AA}$, $c = 5.4925 \text{ \AA}$ [100].
- La₂TiO₅; space group $Pnma$ (62), $a = 11.0092 \text{ \AA}$, $b = 3.9433 \text{ \AA}$, $c = 11.4063 \text{ \AA}$ [101].
- Ti₂Ni (η - phase (Ti₄Fe₂O_{1-x})); space group $Fd3m$, $a = 11.3193(2) \text{ \AA}$ [102]

3.2.2 Scanning Electron Microscope

Scanning electron microscopy (SEM) is used to obtain information about its morphology, chemical composition and crystallinity. The basic principle involves a beam of electrons from an electron column. The electromagnetic lenses focus the electrons into a small beam in the column. An image is produced by the scanning coils, which direct and position the electron beam over the sample surface horizontally and vertically in a raster pattern. A scanning electron microscope (SEM) was used to study Ti-Zr-based AB₂ alloys' morphology, composition, and degree of crystallinity using a Zeiss Auriga scanning electron microscope. The samples were placed on double-sided carbon tape and attached to an aluminium stub.

Elemental composition information was obtained using an energy dispersive X-ray spectroscopy (EDS), which is coupled to SEM. As the basic principle in SEM, EDS uses x-rays which are emitted from the interaction of the sample surface with the electron beam. The interaction results in an excitation of the electrons ejected from the atoms, leaving behind a vacancy. The vacancy is then filled with electrons from a higher energy state and an x-ray to balance the energy difference between the two energy states. The x-rays which are emitted are the characteristic of each element within the sample. The samples were prepared the same manner as in SEM.

3.2.3 Transmission Electron Microscope

A transmission electron microscope (TEM) is one of the most powerful microscopes with respect to its magnification and resolution, it is applied in a wide range of applications and can be utilised in a variety of different fields. The working principle of TEM involves a high voltage electron beam to create the image, where the electron gun is placed at the top, which produces the electron that travels through the vacuum tube. The electromagnetic lens is used to focus the fine beam of electrons that passes through the ultra-thin specimen. The transmitted electrons get hit on the fluorescent screen which is present at the bottom of the microscope. The image of the specimen with its assorted parts appears on the screen which is based on its density. The obtained image can be directly studied or also photographed [103].

Atomic emission spectroscopy is an elemental analysis technique with detection limits of subparts per billion for most elements. It relies on the detection of light emitted by excited atoms. To excite these atoms, such that they will emit sufficient light to allow for routine

detection, samples are most commonly exposed to plasma, flame, arc, or spark at a particular wavelength to determine the quantity of an element in a sample.

Selected area electron diffraction (SAED) is an additional tool used for the investigation of crystal structure of the material. Electrons are accelerated in this instrument via an electrostatic potential to possess the required energy and determine their wavelength before they interact with the material. The periodic structure of a crystalline solid behaves as a diffraction grating, scattering the electrons in a predictable way [104].

The Ti-Zr based AB₂ type alloy was characterised by TEM/SAED (JEOL JEM-2100, operating at 200 kV. The samples were prepared by the deposition of the sample powder, using ultrasonic dispersant, onto a substrate (copper mesh covered with electrically conductive amorphous film). The studies of the elemental composition of the alloys were supplemented by the atomic emission spectroscopy (AES) for the detection of impurities using a laser analyser LES-S500 (SOL Instrument). Improvement of the resolution of the impurity spectral lines overlapping with the ones for the metallic components was achieved by optimising the energy of laser irradiation impulse in the range between 19 and 21.5 J.

It should be noted that only the upscaled alloys were studied by this technique.

3.2.4 Hydrogen sorption measurements

There are two means of expressing the amount of hydrogen stored in metal hydride forming materials. Gravimetric techniques are used to determine the amount of hydrogen absorbed or desorbed by a sample through calculating the change in its mass. Volumetric techniques determine the amount of hydrogen absorbed or desorbed by a sample by calculating the change in pressure of a fixed volume.

For metal hydride, the volumetric method involving Sievert's type apparatus is used for measurement. The basic operating principle is based on introducing a known amount of gas into a known volume containing an absorbing sample and measuring the pressure. By assuming an equation of state, usually the ideal gas law with the correction taking into account the gas compressibility, the amount of absorbed gas can be calculated.

A basic diagram of a Sievert's system is shown in Figure 3.3. Known dose volumes (V1) and reactor volumes (V2) are determined. The control of the gas pressure set in V1 are done by valves A and B. The pressure in V2 is varied by valve C, which is a fast opening valve. The

pressure gauge is used to monitor the pressure in V1. V1 is set at a constant temperature (e.g. T_1 ; 303 K), whilst V2 can be set at a desirable temperature (T_2) using a furnace or water bath. Thermocouples are placed in the furnace and sample holder to control and monitor the temperature.

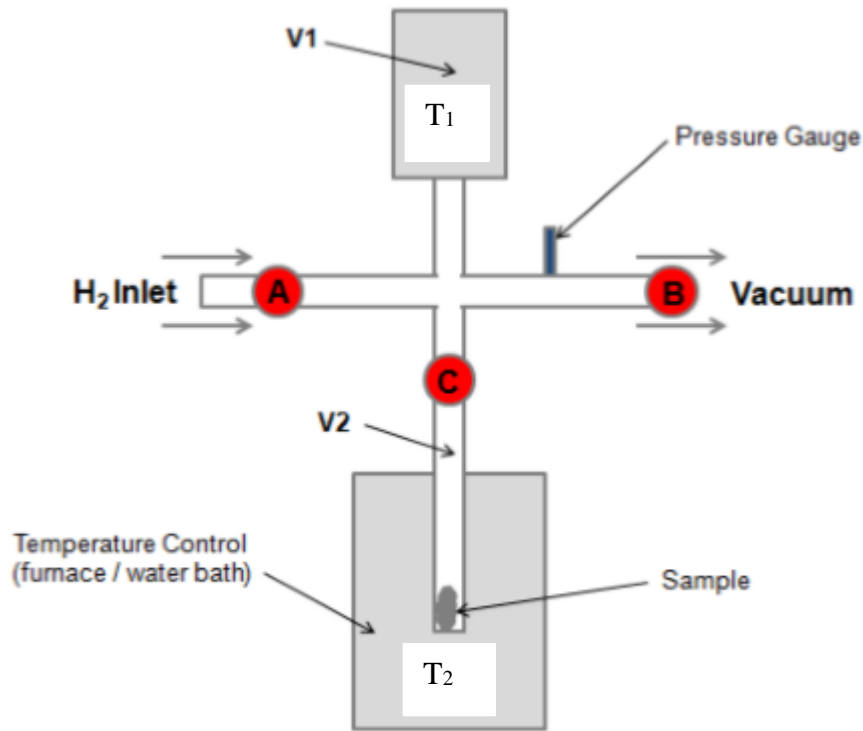


Figure 3. 3: Basic diagram of Sievert's system [38].

During an absorption measurement, an initial pressure (P_i) is set in V1, while all valves are closed. The pressure is allowed to stabilize and recorded. Valve C is opened and the pressure is allowed to reach equilibrium. The equilibrium pressure is measured in V1 only and then valve C is closed.

The equation for the number of hydrogen moles uptake by a sample at any given pressure step is given by:

$$\Delta n = n_2 + n_1$$

Where:

$$n_1 = \frac{P_i^{V1}}{Z_i(P_i^{V1}, T_1) RT_1} + \frac{P_i^{V2}}{Z_i(P_i^{V2}, T_2) RT_2};$$

$$n_2 = \frac{P_f}{Z_f(P_f, T_1) RT_1} + \frac{P_f}{Z_f(P_f, T_2) RT_2};$$

Z_i and Z_f are hydrogen compressibility factors calculated for the corresponding pressures and temperatures.

T_1 and T_2 are temperatures of volumetric system and reactor with the sample, respectively.

P_i is the initial pressure measured, V_1 and V_2 relate to the volumetric system and reactor, respectively.

P_f is the final pressure measured.

R is the universal gas constant.

The wt. % of hydrogen can be calculated once the calculation of moles of hydrogen has been determined with the known sample mass.

The performance of Ti-Zr based AB₂ hydride-forming materials is represented by pressure-composition-temperature (PCT) diagrams. The PCT diagram provides a clear understanding of the hydrogenation/dehydrogenation properties and phase transformation occurring in the hydrogen sorption material, hydride stability, and equilibrium relationships between the H₂ pressure and concentration at a constant temperature.

The pressure-composition-temperature isotherms (PCI) of the samples were measured using a commercial automated Sievert-type apparatus (PCT Pro-2000). Approximately 1g of the sample was loaded into the reactor, the sample was then activated by heating to 300°C under dynamic vacuum for 1 hour. The sample was allowed to cool down to ambient temperature, followed by charging with hydrogen at 100 bar. The hydrogen absorption and desorption isotherms were recorded at temperatures of 20, 40, and 60°C and hydrogen pressures from 0.1 to 100 bar.

Chapter 4: Results and Discussion

4.1 Effect of preparation routes on the performance of a multi-component Ti-Zr based AB₂-type hydrogen storage alloy

In this work we studied the effect of preparation of Ti-Zr based AB₂ alloys to demonstrate the influence of the preparation routes on the hydrogen storage performance of the alloys. The AB₂ type hydrogen storage alloy (A= Ti_{0.85}Zr_{0.15}, B= Mn_{1.22}Ni_{0.22}Cr_{0.2}V_{0.3}Fe_{0.06}), was prepared by induction melting of the metallic components under Ar atmosphere. Two types of crucibles were used: ceramic alumo-silica (Al₂O₃+SiO₂) and graphite, ~150 g in weight each. In the induction melted samples 1 wt.% La was added to the charge to assist with the activation of the alloy. To minimise interaction between the melt and the crucible material, both crucibles were coated inside by the deposition of a protective coating whose surface contacting the melt was yttria (Y₂O₃) see Chapter 3 on the method used to coat the crucibles. The reference sample of the same composition was prepared by arc-melting.

4.1.1 Surface morphology and elemental composition of Ti-Zr based AB₂ type alloys prepared by different routes

The SEM images of the AB₂ type alloy samples prepared by the different routes are shown in Figure 4.1. The SEM images show that there are no visual differences between the alloys prepared by arc and induction melting: all the alloys exhibit a smooth, continuous surface.

The EDS results (Table 4.1) show that the measured amounts of the metallic components are in satisfactory correspondence with the nominal composition of the alloy. However, for the induction melted samples several deviations were observed. Mainly, it relates to the underestimation of Zr content in the alloy induction-melted in alumo-silica crucible.

No impurities were detected in the arc-melted alloy, while both alloys prepared by induction melting contained oxygen (O) impurities. The presence of oxygen can be attributed to the contamination of the sample with Y₂O₃ particles from the crucible coating (most probable reason for the sample melted in the graphite crucible where oxygen was detected only in a few separate points), as well as to the interaction of the melt with the residual atmosphere of the induction furnace chamber and with the inner surface of the crucible. The latter also relates to the source of the silicon (Si) impurity, which was found only in the sample prepared in the alumo-silica crucible. The EDS results allow us to conclude that the applied protecting coating, which eliminates severe contamination of the ingot and destruction of the crucible due to its interaction with the melt, does not result in the complete elimination of the latter process

accompanied by the leaching of some metallic components and contamination of the ingot with non-metallic impurities. However, this effect is much less pronounced for the graphite crucible. Due to interference with the background signal from carbon support, the reliable determination of carbon in the studied samples by EDS was not possible.

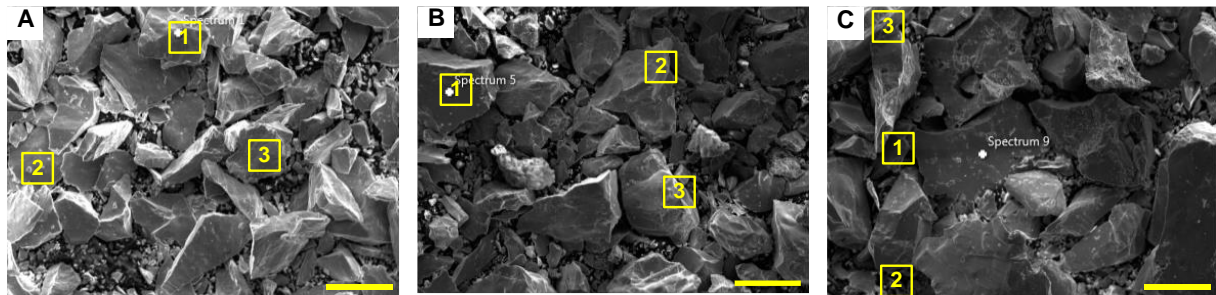


Figure 4. 1: SEM images of the AB₂-type alloy prepared by (A) – arc-melting and annealing, (B) – induction melting in alumo-silica crucible, and (C) – induction melting in graphite crucible. Each scale bar (thick yellow line) corresponds to 100 μm.

Table 4. 1: Summary of compositional properties of the alloy samples according to EDS data collected from typical points (1–3 in Figure 4.1).

Components	Content (wt. %)												
	Nominal	Measured Fig. 4.1 (A) Arc melted				Measured Fig. 4.1 (B) Induction melted (Alumina crucible)				Measured Fig. 4.1 (C) Induction melted (Graphite crucible)			
		Total area	Point 1	Point 2	Point 3	Total area	Point 1	Point 2	Point 3	Total area	Point 1	Point 2	Point 3
A (Ti)	26.38	25.43	24.26	26.57	23.74	25.5	24.82	24.85	23.93	28.25	25.65	25.51	28.73
A (Zr)	8.38	7.05	9.19	8.83	8.8	7.3	5.16	4.93	9.09	8.3	9.95	8.48	6.45
B (Cr)	6.82	6.96	6.9	6.2	6.5	7.66	7.46	8.18	8.17	7.25	6.7	6.98	6.9
B (Mn)	40.76	43.96	41.82	39.84	42.6	42.44	43.16	42.93	41.69	40.25	43.08	41.67	40.34
B (Ni)	6.21	4.96	6.69	6.64	6.01	5.14	5.19	4.95	6.08	4.42	4.45	5.84	6.53
B (V)	9.47	9.47	9.34	10.09	9.99	9.3	10.32	11.07	8.54	9.29	8.14	7.5	7.51
B (Fe)	1.98	2.17	1.8	2.08	2.36	1.92	1.95	1.99	1.73	2.24	2.03	2.15	1.88
Impurity (O)						2.24	0.67	0.59	0.11			1.87	1.66
Impurity (Si)						0.42	0.39	0.51	0.66				

4.1.2 Phase and structural characterisation of Ti-Zr based AB₂ type alloys prepared by different routes

The refined XRD patterns of the AB₂ type alloys prepared by the different routes are shown in Figure 4.2. The calculated abundancies and lattice periods of the constituent phases are summarised in Table 4.2; for the major C14-AB₂ phase, the unit cell volumes are presented as well. The last column in Table 4.2 also presents the estimations of the crystallite size of the constituent phases. It is seen from Table 4.2 that the sample prepared by arc melting is single-phase, which is in line with the EDS results (Table 4.1). In La-containing induction-melted samples, La₂TiO₅ formed during interaction of La deoxidiser with molten Ti and oxygen was detected. In the sample induction melted in alumo-silica crucible main impurity phase was found to be the (Ti,Zr)O₂ mixed oxide characterised by broad peaks testifying about nanocrystalline nature of this impurity. The lattice periods and unit cell volumes of the major C14- AB₂ phase in the studied samples are higher as compared to the reference data [100] ;the increase of the unit cell volume for the arc melted alloy was of 3.81% at the similar *c/a* ratio (1.637 against 1.641 for the studied and reference samples, respectively). The increase in the lattice periods is caused by the higher content of zirconium (atomic radius 1.60 Å) in the studied alloy as compared to the reference intermetallic mainly containing Ti (atomic radius 1.46 Å).

When comparing the unit cell volume of the major phase in the arc melted and induction melted alloys, it can be seen that for the alloy melted in alumo-silica crucible, it is reduced by 0.91% while increases by 0.71% for the alloy melted in the graphite crucible. The smaller lattice periods and unit cell volume for the sample induction melted in alumo-silica crucible can be explained by the reduced content of Zr in this alloy (Table 4.1). The reason for the increase of the lattice periods of the C14-AB₂ phase in the sample induction melted in the graphite crucible is less clear. Presumably, it could be explained by the presence of interstitial carbon in this sample.

The XRD patterns of the induction melted samples (Figure 4.2 (B, C)) exhibit less intensive and more broad peaks than the arc melted sample (Figure 4.2 (A)), testifying about a significant decrease in the crystallite size of the major C14-AB₂ phase (see last column in Table 4.2). It has to be noted that the presented values are only rough estimations because, for the major C14-AB₂ phase in the arc melted and induction-melted in graphite crucible samples, the calculated crystallite size exceeds or approaches the value of 100–200 nm above which the precision of the size calculations from XRD data drops dramatically [105], [106]. Nevertheless, this observation testifies about high degree of crystallinity of the major phase in these samples

further confirmed by the TEM/SAED studies (section 4.1.3) while the impurity phases have a nanocrystalline nature.

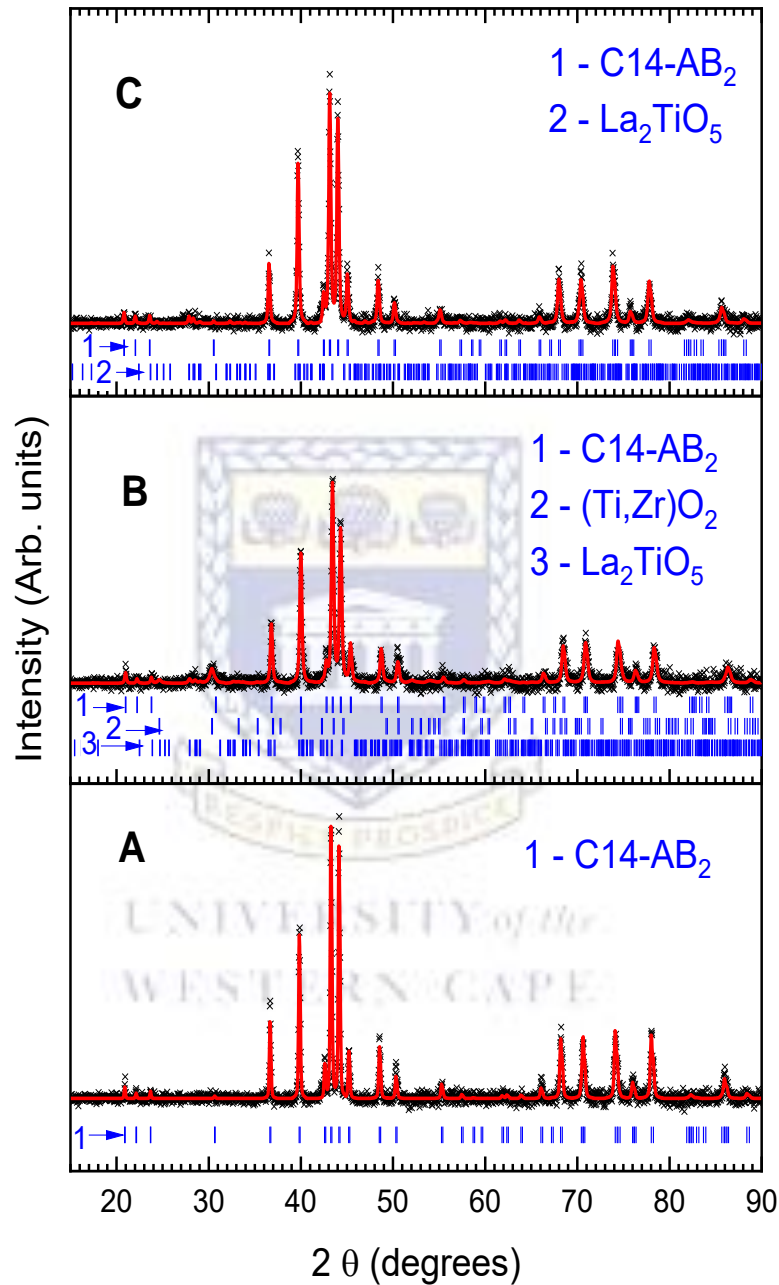


Figure 4. 2: Observed (points) and calculated (red lines) XRD patterns of the AB₂-type alloy prepared by (A) – arc-melting, (B) – induction melting in alumo-silica crucible, and (C) – induction melting in graphite crucible. Bottom ticks show the calculated peak positions of the constituent phases.

Table 4. 2: Results of Rietveld refinement of the XRD patterns of the studied alloy samples (Figure 4.2). Errors of the values calculated during refinement (shown in brackets) relate to the last decimal digit.

Alloy Composition Preparation method	Phase	Abundance (wt. %)	Lattice periods (Å)			Unit cell volume (Å ³)	Estimated crystallite size (nm)
			<i>a</i>	<i>b</i>	<i>c</i>		
Ti _{0.85} Zr _{0.15} Cr _{0.2} Mn _{1.22} Ni _{0.22} V _{0.3} Fe _{0.06} Arc melting	C14-AB ₂	100(-)	4.8910(1)	–	8.0063(3)	165.868(8)	>300
Ti _{0.85} Zr _{0.15} Cr _{0.2} Mn _{1.22} Ni _{0.22} V _{0.3} Fe _{0.06} + 1 wt. % La Induction melting in alumo-silica crucible	C14-AB ₂	87.9(-)	4.8765(2)	–	7.9810(6)	164.37(2)	80
	(Ti,Zr)O ₂	10.2(6)	4.86(1)	5.38(1)	5.08(1)		25
	La ₂ TiO ₅	1.9(3)	10.90(5)	3.93(1)	11.43(4)		50
Ti _{0.85} Zr _{0.15} Cr _{0.2} Mn _{1.22} Ni _{0.22} V _{0.3} Fe _{0.06} + 1 wt. % La Induction melting in graphite crucible	C14-AB ₂	98.0(-)	4.9019(1)	–	8.0290(4)	167.08(1)	100
	La ₂ TiO ₅	2.0(3)	10.80(2)	3.952(5)	11.58(2)		80

4.1.3 TEM, SAED and AES characterisation of Ti-Zr based AB₂ type alloys prepared by different routes

The TEM images and selected area electron diffraction (SAED) patterns taken from the areas containing several alloy particles are shown in Figure 4.3. The patterns exhibit the presence of both rings and spots, signifying that the alloys are mainly polycrystalline in nature. However, all the samples exhibit the presence of separate, almost completely monocrystalline particles (Figure 4.4), which for the sample melted in the graphite crucible (E, F) have the highest degree of crystallinity. This sample also does not contain completely polycrystalline separate particles, which were found in other samples. The reason for these observations appears to be due to the slower cooling rate of this sample since both the electrically conductive graphite crucible and the sample were heated during induction melting, therefore the hot mass (100g of the sample and 150 g of graphite) will cool down slower than in the case of alumo-silica crucible (100 g of sample only) at the similar cooling conditions. Conversely, very fast cooling of the sample during arc melting may result in a slightly poorer crystallinity; see Figure 4.4(A, B). For the sample induction melted in alumo-silica crucible is characterised by the poorest crystallinity Figure 4.4(C, D). The origins of the observed effect may also be in the presence of noticeable amounts of impurity phases, including nanocrystalline (Ti,Zr)O₂ (see XRD data in Table 4.2). It was not detected in the SAED patterns, as well as introducing silicone into metallic matrix (see Table 4.1) associated with appearance of additional lattice defects.

The SAED patterns for all the samples exhibit the presence of the major phase C14-AB₂ in good correspondence with XRD results, as illustrated by the example in Figure 4.5(A, B) for the sample melted in alumo-silica crucible. Of the impurity phases, only traces of La₂TiO₅ poorly crystallised monocrystals were found in the induction-melted samples (Figure 4.5(C)). The low probability of occurrence of the corresponding reflections in SAED patterns taken from an area of $\sim 1 \mu$ in diameter (Figure 4.5 (A)) is caused by the small content of this phase in the sample (≤ 2 wt.% according to the XRD data).

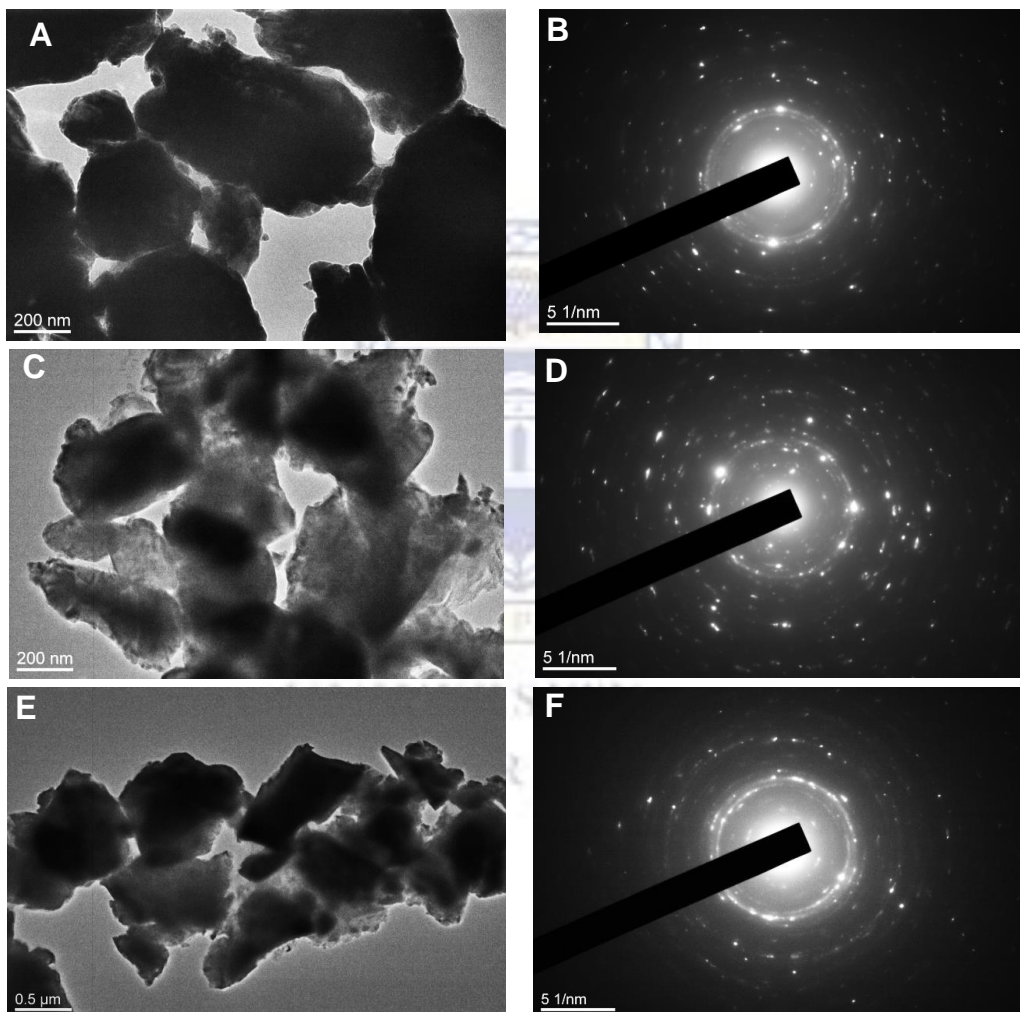


Figure 4. 3: TEM images (A,C,E) and the corresponding SAED patterns (B,D,F) for the arc-melted sample (A,B), the sample induction melted in the alumo-silica crucible (C,D) and the sample induction melted in the graphite crucible (E,F).

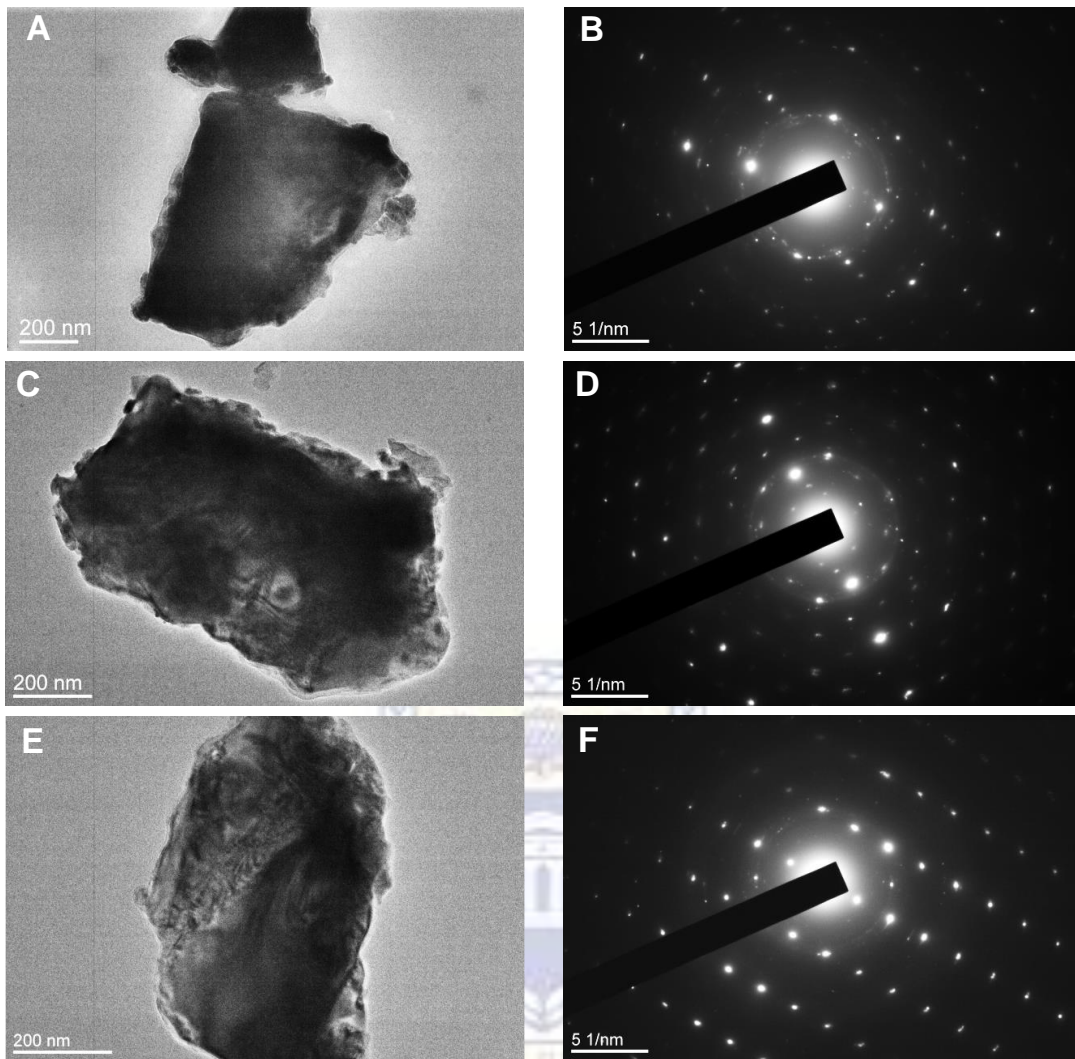


Figure 4. 4: TEM images (A,C,E) and the corresponding SAED patterns (B,D,F) of separate particles for the arc-melted sample (A,B), the sample induction melted in the alumo-silica crucible (C,D) and the sample induction melted in the graphite crucible (E,F).

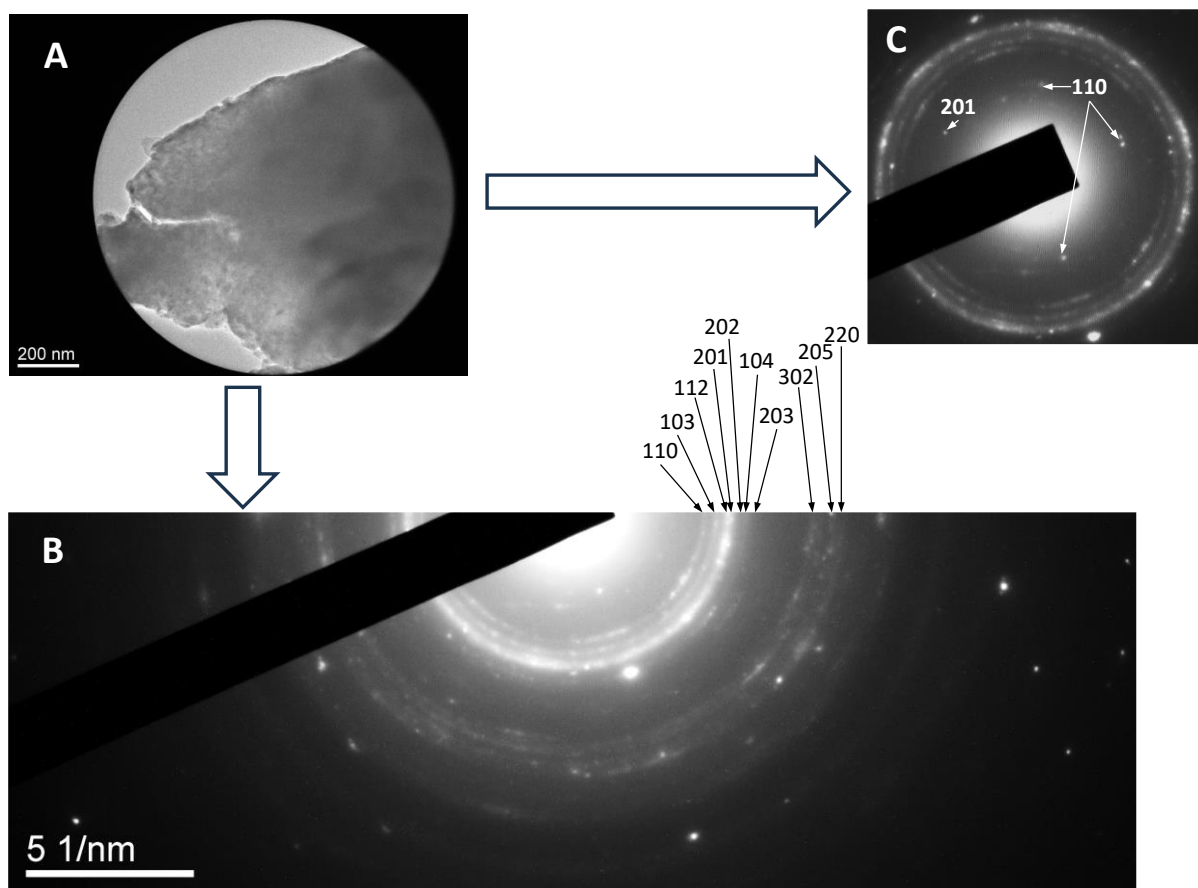


Figure 4. 5: Selected area of the TEM image (A) taken for the sample induction melted in alumo-silica crucible and the corresponding SAED patterns supplemented by Miller indexes of rings and spots for the major C14-AB₂ phase (B) and La₂TiO₅ impurity (C).

The AES studies gave a semi-quantitative validation of the EDS and XRD results, according to which the main impurity in the induction-melted samples was oxygen. It is illustrated by Figure 4.6. The maximum amount of the oxygen impurity was determined for the sample induction melted in alumo-silica crucible, followed by the sample induction melted in graphite crucible and the arc melted sample.

Due to the overlapping of the most intensive carbon line (247.8561 nm) with the lines of Fe, Cr and Ti, it could not be resolved during AES studies. We assume that all three samples do not contain noticeable amounts of carbon, but presence of its traces is possible.

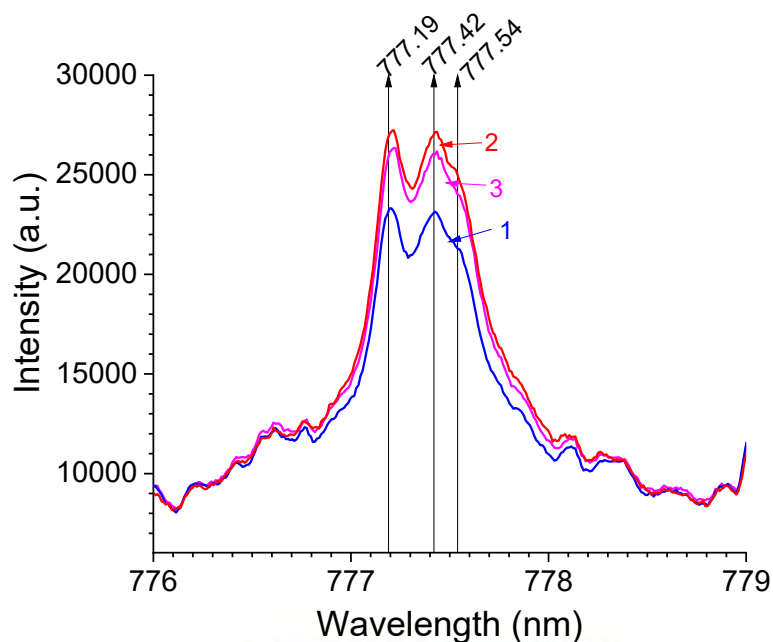


Figure 4. 6: Fragments of atomic emission spectra for the arc-melted sample (1) and samples induction melted in aluminosilica (2) and graphite (3) crucible. The most intensive oxygen spectral lines are shown by the vertical arrows.

4.1.4 Hydrogen sorption properties of Ti-Zr based AB₂ type alloys prepared by different routes

Figure 4.7(A) shows the as-measured hydrogen absorption and desorption isotherms ($T=20\text{ }^{\circ}\text{C}$) for the Ti-Zr based AB₂ alloys prepared by induction melting and arc melting. The corresponding van't Hoff plots at $H/M=0.35$ are shown in Figure 4.7(B), and the main hydrogen sorption parameters taken from the pressure – composition isotherms are summarised in Table 4.3.

As it can be seen, the induction melted samples exhibit significant reduction in both maximum and reversible hydrogen storage capacity, especially pronounced for the sample induction melted in aluminosilica crucible. This sample (# 2 in Figure 4.7) is also characterised by the lowest thermal stability of hydride, resulting in the higher hydrogen equilibrium pressures. The latter effect can be explained by the lower content of the zirconium in this sample shown by the EDS results, which also results in the decrease of the lattice periods and the unit cell volume of the C14-AB₂ major phase confirmed by the XRD results. The decrease of the maximum hydrogen storage capacity also correlates well with the minimum abundance of this phase as shown by XRD ($\sim 88\%$; Table 4.2) where the impurity phases do not absorb hydrogen. Thus,

we can conclude that during induction melting in the alumo-silica crucible, even protected by Y_2O_3 coating, the crucible – melt interaction, along with oxygen contamination, results in the predominant removal from the melt of Zr characterised by higher than Ti affinity to oxygen [66].

The induction melted samples are also characterised by the increased plateau slope, which is especially pronounced for the sample melted in the graphite crucible. This effect can be associated with the inhomogeneity of these samples. An additional reason may be in the incorporation of the traces of non-metallic impurities into interstitials of the $C14-AB_2$ major phase. Such effects for boron and carbon were observed for TiFe accompanied by a drastic decrease in hydrogen sorption capacity and increase in the plateau slope [107].

We note that despite the significantly more incline plateau for the sample induction melted in the graphite crucible, the thermal stability of its hydride is very close to the one for the arc melted sample (Figure 4.7(B), Table 4.3).

All the alloys are characterised by a moderate hydrogen absorption desorption hysteresis, $\ln(P_A/P_D)=0.3-0.5$, or hysteresis energy loss, $RT \ln(P_A/P_D)=0.75-1.25$ kJ/mol H_2 .

Hysteresis slightly decreases in the series: arc melted \rightarrow induction melted in alumo-silica crucible \rightarrow induction melted in graphite crucible.

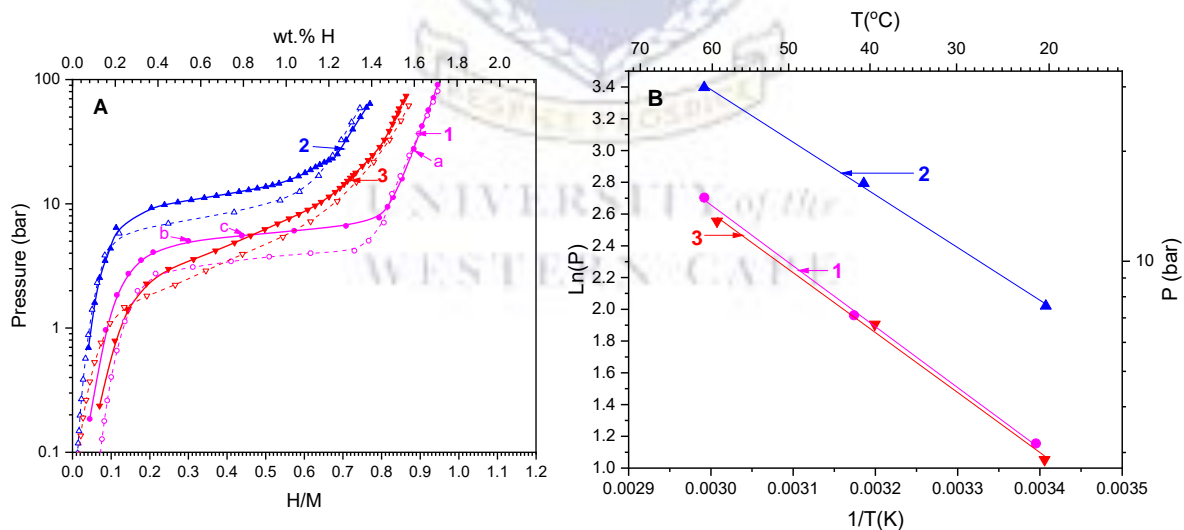


Figure 4. 7: Hydrogen absorption and desorption isotherms at $T=20^\circ C$ (A) and van't Hoff plots for the AB_2 -type alloy samples (B): (1) – arc melted, (2) – induction-melted in alumo-silica crucible and (3) – induction-melted in graphite crucible. Points a, b and c on the absorption isotherm for the arc melted sample (1 in A) correspond to hydrogen pressures and concentrations for which kinetic data (Figure 4.8A,B) are presented..

Table 4. 3: Hydrogen sorption parameters of the studied alloy samples

Parameter		Sample		
		Arc melted	Induction melted in alumo-silica crucible	Induction melted in graphite crucible
H sorption capacity (H/M / wt.% H)	Maximum (absorption at T=20°C, P=50 bar)	0.92 / 1.64	0.75 / 1.36	0.83 / 1.50
	Reversible (absorption at T=20°C, P=15 bar, desorption at T=60°C, P=5 bar))*	0.76 / 1.37	0.50 / 0.89	0.58 / 1.03
Thermodynamic parameters of hydride formation	–ΔH° (kJ/mol H ₂)	31.88	27.59	31.39
	–ΔS° (J/(mol H ₂ K))	117.74	111.07	115.85
	Hysteresis at T=20°C, Ln(P _A /P _B)	0.488	0.368	0.297
	Plateau slope at T=20°C, d(Ln P)/d(H/M)	0.991	1.227	3.363

*typical conditions for the integrated energy systems comprising PEM electrolyser and PEM fuel cell

All the studied samples exhibit excellent hydrogen absorption and desorption kinetics. As it can be seen from Figure 4.8(A), even the first H₂ absorption after vacuum heating is very fast: the equilibrium corresponding to point A in Figure 4.8(A) is achieved in 1 hour while about 90% of hydrogen is absorbed during the first 2 minutes accompanied by significant self-heating the sample due to exothermic nature of the hydrogenation process. Similar behaviour was observed during the measurements of the pressure–composition isotherms characterised by the low pressure driving force. It is illustrated by Figure 4.8(B) which shows hydrogen absorption kinetics for the same alloy when passing from point B to point C on the absorption isotherm (Figure 4.7A). The equilibrium is achieved in less than 10 minutes, and 95% of hydrogen is absorbed in 2 minutes.

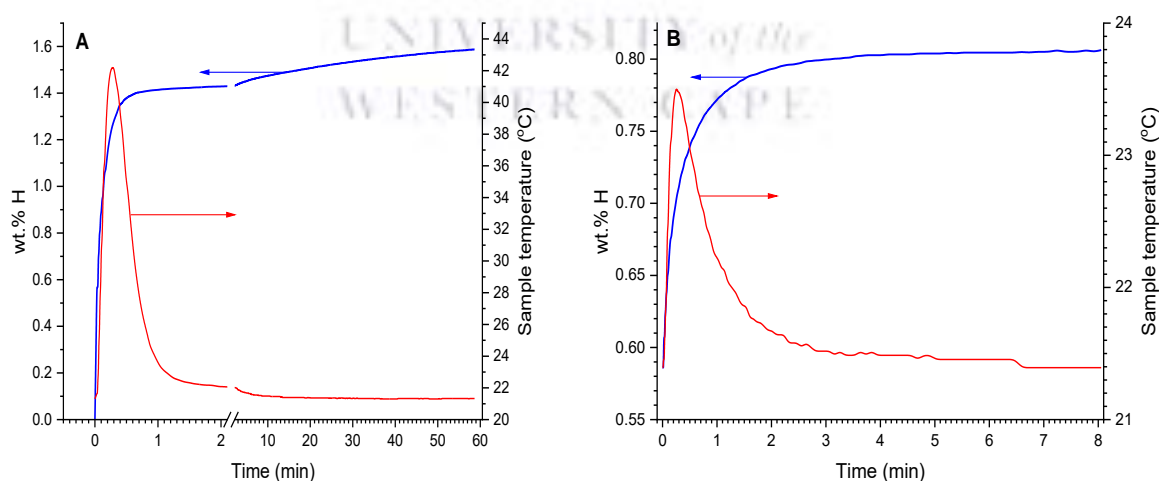
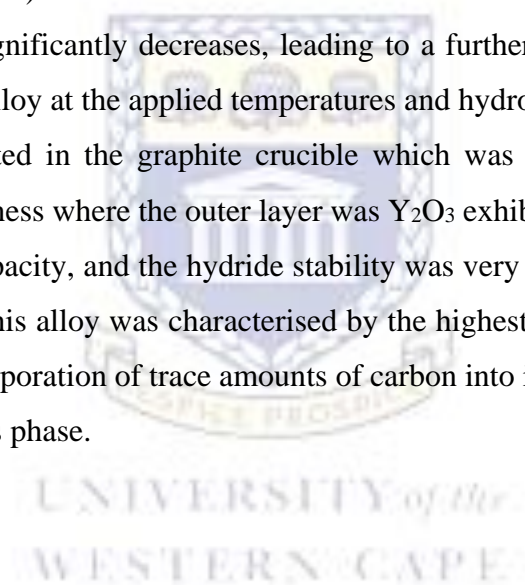


Figure 4. 8: Hydrogen absorption kinetics and changes of the sample temperature at T₀=21°C for the arc melted sample: A – first absorption at the starting H₂ pressure of 33 bar and final H₂ pressure of 27 bar (point a in Figure 4.7A). B – hydrogen absorption during the measurement of the pressure–composition isotherm (points b and c in Figure 4.7A)

4.1.5 Conclusions on the effect of preparation routes of Ti-Zr based AB₂ type alloys
Our results confirmed the high sensitivity of hydrogen sorption properties of AB₂-type hydrogen storage alloys (A=Ti+Zr) to their preparation routes, particularly when moving from arc melting to induction melting. The changes observed for the induction-melted alloys include lowering the hydrogen storage capacity and increasing the plateau slope mainly associated with the crucible – melt interaction accompanied by contamination of the ingot. Another reason for the observed effects is the higher inhomogeneity of the induction-melted alloys.

The crucible – melt interaction, which cannot be completely suppressed by the protective 0.05 inches-thick coating of the alumo-silica crucible deposited by spray painting of suspension of Y₂O₃ powder, results in the contamination of the ingot with the components of the crucible material (oxygen, silicon, aluminium) and simultaneous leaching of zirconium (having the strongest affinity to oxygen) from the melt. As a result of the latter process, thermal stability of the formed hydride significantly decreases, leading to a further decrease of the hydrogen sorption capacity of the alloy at the applied temperatures and hydrogen pressures.

The alloy induction melted in the graphite crucible which was protected by a three-layer coating of the same thickness where the outer layer was Y₂O₃ exhibited the lesser reduction of the hydrogen sorption capacity, and the hydride stability was very close to the one for the arc melted alloy. However, this alloy was characterised by the highest plateau slope, presumably originating from the incorporation of trace amounts of carbon into interstitials of the matrix of the major C14-AB₂ Laves phase.



4.2 Effect of Oxygen substitution on Ti-Zr based AB₂ alloy

Numerous studies on Ti-Zr based AB₂ alloys have been carried out in order to improve the performance of the alloy such as the storage capacity, cyclic stability, kinetics and activation which are normally achieved by substitution with different alloying elements [108],[109].

The effects of oxygen in Ti-based alloys have been studied by various researchers, they concluded that even small amounts of oxygen affect the P-C isotherms, predominantly the dissociation pressure, the hydrogen storage capacities decrease and the plateau pressures of the alloys increase with increased oxygen concentration [110]–[112].

Introduction of oxygen in the alloys of Ti and/or Zr with transition metals (TM=Fe, V, Ni, etc.) often results in the formation of oxygen-stabilised intermetallic η -phases, η_1 - (Ti,Zr)₃TM₃O_{1-x} and η_2 -(Ti,Zr)₄TM₂O_{1-x} with crystal structures related to Ti₂Ni. These phases often form hydrides which, however, are characterised by high stabilities thus reducing reversible hydrogen storage capacity of the material at pressure-temperature conditions specific for the applications. In this work, a multi component Ti-Zr based AB₂-type alloy with a composition of (A=Ti_{0.85}Zr_{0.15}, B=Mn_{1.22}Ni_{0.22}Cr_{0.2}V_{0.3}Fe_{0.06}) was prepared by arc-melting. The alloy was also further modified by oxygen to yield the composition AB₂O_{0.05}. The oxygen was introduced by adding TiO₂ to the charge, with corresponding decrease of the Ti amount. Both alloys were annealed at 950 °C for 24 h followed by quenching in ice water.

4.2.1 Surface morphology and elemental composition of oxygen modified Ti-Zr based AB₂ alloy

The SEM images of the unmodified AB₂ and modified AB₂O_{0.05} are shown in Figure 4.9. The SEM and EDS analysis shows that both alloys are homogeneous. It can be observed that both alloys have a smooth continuous surface. It can also be seen that the oxygen modified sample (Figure 4.9 (B)) has more cracks on the surface than the unmodified sample (Figure 4.9 (A)). The EDS results shown in Table 4.4 confirm the XRD data, which displays the main C14-Laves phase with a composition corresponding to A:B≈2, this is confirmed as the measured amounts of the metals correspond closely to the nominal composition of the alloy. EDS results show that the total oxygen impurity was 0.78 wt.% for the modified sample (B), while in the unmodified sample (A) oxygen was only detected at point 2, this can be attributed mainly to the use of FeV as it contains small amounts of impurities.

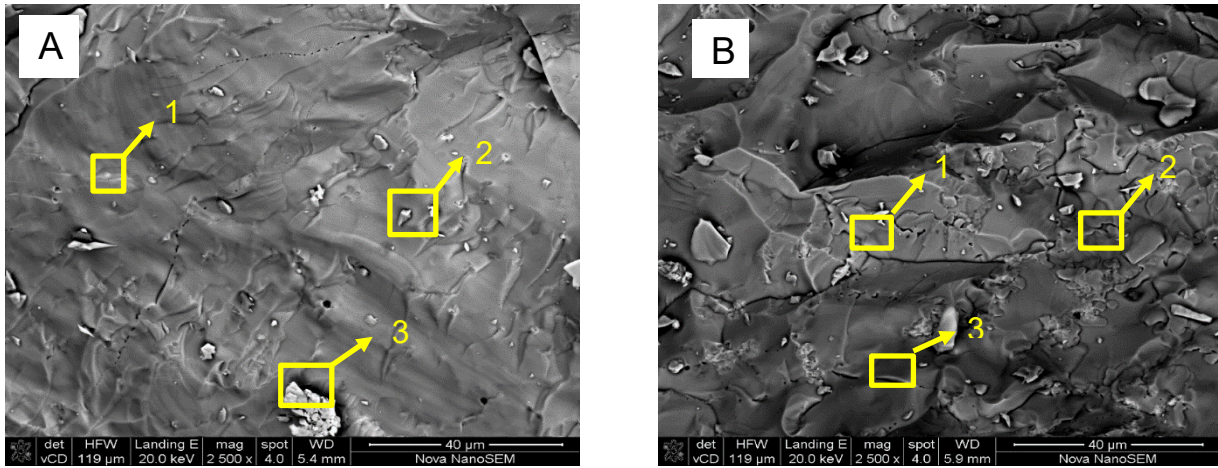


Figure 4. 9: SEM images for the arc-melted samples: (A) $\text{Ti}_{0.85}\text{Zr}_{0.15}\text{Cr}_{0.2}\text{Mn}_{1.22}\text{Ni}_{0.22}\text{V}_{0.3}\text{Fe}_{0.06}$, (B) $\text{Ti}_{0.85}\text{Zr}_{0.15}\text{Cr}_{0.2}\text{Mn}_{1.22}\text{Ni}_{0.22}\text{V}_{0.3}\text{Fe}_{0.06}\text{O}_{0.05}$

Table 4. 4: Compositional properties of the multi component AB2 type alloys prepared via arc melting

Components	Content, wt. %									
	Measured Fig 4.8(A) $\text{Ti}_{0.85}\text{Zr}_{0.15}\text{Cr}_{0.2}\text{Mn}_{1.22}\text{Ni}_{0.22}\text{V}_{0.3}\text{Fe}_{0.06}$					Measured Fig 4.8(B) $\text{Ti}_{0.85}\text{Zr}_{0.15}\text{Cr}_{0.2}\text{Mn}_{1.22}\text{Ni}_{0.22}\text{V}_{0.3}\text{Fe}_{0.06}\text{O}_{0.05}$				
	Nominal	Total area	Point 1	Point 2	Point 3	Nominal	Total area	Point 1	Point 2	Point 3
A (Ti)	24.922	26.44	25.08	24.32	29.86	24.8	24.31	26.37	28.02	26.44
A (Zr)	8.375	8.72	9.86	9.27	8.39	8.335	9.45	8.73	8.63	12.3
B (Cr)	6.365	4.9	5.3	6.66	3.77	6.334	6.09	6.97	5.49	8.08
B (Mn)	41.026	39.19	39.8	39.89	35.42	40.826	40.02	39.43	37.74	32.7
B (Ni)	7.906	9.31	8.46	7.8	11.72	7.868	7.31	6.31	7.81	6.72
B (Fe)	2.051	1.99	2.07	2.15	1.78	2.041	2.4	2.25	2.34	2.7
B (V)	9.355	9.45	9.44	8.75	9.06	9.309	9.64	8.82	9.33	10.21
Impurity:(O)	-	-	-	1.16	-	0.487	0.78	1.12	0.64	0.85

4.2.2 Phase and structural properties of oxygen modified Ti-Zr based AB₂ alloy

Figure 4.10 shows the refined XRD patterns for the as prepared alloys (A, C) and the hydrogenated alloys (B, D). XRD analysis showed that both alloys consist of the main C14 Laves phase. Both alloys exhibited impurity of η – phase (Ti₄Fe₂O_{1-x}), Ti₂Ni-type intermetallic stabilised by interstitial oxygen [113] introduced into the sample during its preparation as a result of oxygen capture by the titanium-containing melt which has very strong affinity to oxygen [66]. The abundance of the η – phase for the as prepared AB₂ and AB₂O_{0.05} alloys corresponds to 1.2 and 3.8 wt. % respectively. The reason for the appearance of the impurity phase in the unmodified sample (A) is mainly attributed to the use of commercial ferrovanadium containing oxide impurities. The main constituent of the hydrogenated alloys is a hydride phase AB₂H_x with the increased unit cell volume $\Delta V/V_0 = 24.93\%$ and 25.80% , for the unmodified (Figure 4.9 (B)) and oxygen-modified (Figure 4.9(D)) samples, respectively.

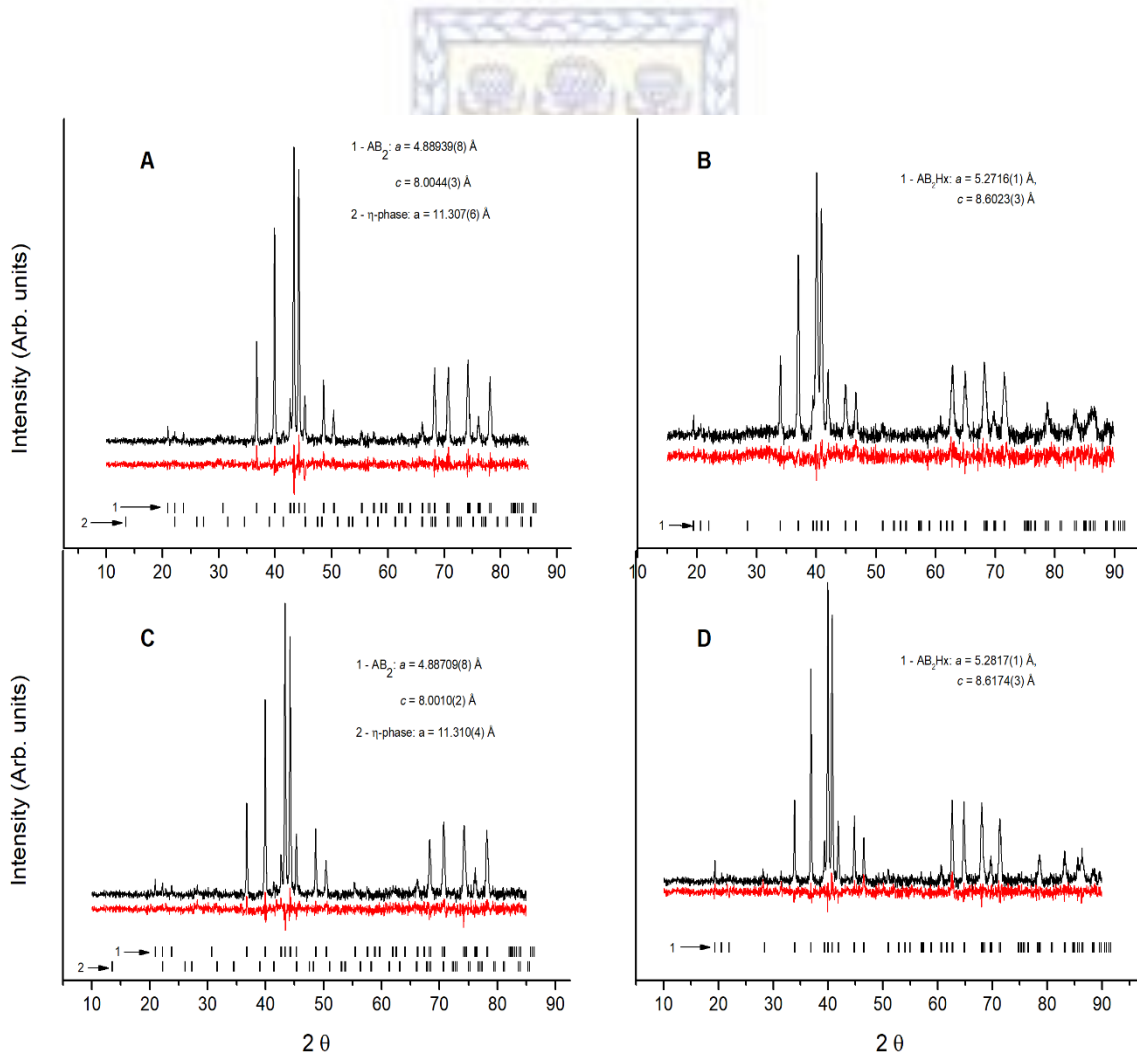


Figure 4. 10: XRD patterns for arc-melted samples (A) as prepared AB₂ alloy, (B) hydrogenated AB₂ alloy, (C) as prepared AB₂O_{0.05} alloy, (D) hydrogenated AB₂O_{0.05}.

4.2.3 Hydrogen absorption kinetics of the unmodified and oxygen-modified Ti based AB₂ alloy

The hydrogen absorption kinetics of the unmodified and oxygen-modified Ti based AB₂ are illustrated in Figure 4.11. It can be seen that despite slightly slower kinetics for AB₂O_{0.05} as compared to oxygen-free AB₂ after activation by vacuum heating, it starts to absorb H₂ in the non-activated state immediately while the non-activated oxygen-free sample has an incubation period about 30 minutes. This is mainly due to the occurrence of the η -(Ti,Zr)₄Fe₂O_{1-x} phase in the alloy, which acts as a catalyst for hydrogen absorption; it also increases brittleness of the starting alloy. However, the introduction of oxygen into the alloy leads to a slight decrease in the hydrogen absorption capacity, from 1.8 wt. % to 1.7 wt. %.

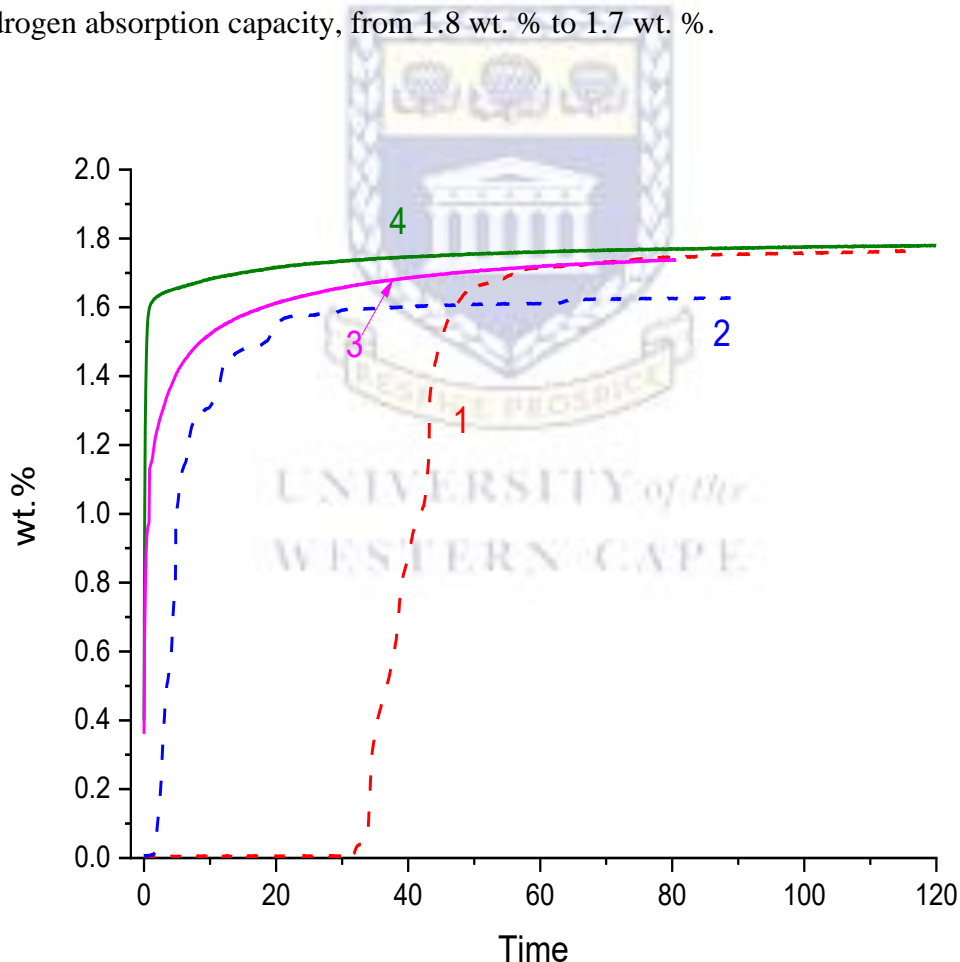


Figure 4. 11: Hydrogen absorption kinetics at T=20 °C and P₀ = 30 bar for the Ti-based AB₂ type alloys: (1) AB₂ alloy without activation, (2) AB₂O_{0.05} alloy without activation, (3)

AB₂O_{0.05} alloy after activation by vacuum heating at 300 °C for 1 hr, (4) AB₂ alloy after activation by vacuum heating at 300 °C for 1 hr.

4.2.4 Hydrogen sorption PCT properties of unmodified and oxygen-modified Ti based AB₂ alloy

Figure 4.12 (A) and (B) shows the hydrogen absorption and desorption isotherms of unmodified and oxygen-modified Ti based AB₂ alloys at 20, 40 and 60 °C. The isotherms for both samples exhibit the presence of two different phases namely α -solid solution of hydrogen in the parent intermetallic and β -hydride. The two-phase ($\alpha + \beta$) region of hydrogen concentrations is manifested by the appearance of plateau. From the P-C isotherms measurement, the maximum hydrogen storage capacity was approximately 1.8 wt. % at P(H₂) = 90 bar and T=20 °C for both alloys. The reversible storage capacity for the unmodified AB₂ alloy is 1.62 wt. % and for the oxygen modified AB₂ alloy it is 1.56 wt. %. The reason for the slight decrease in the H storage capacity could be due to the formation of hydride of the η -phase which is characterised by a high stability and does not desorb hydrogen at experimental pressure – temperature conditions.

The formation of the η -phase (A:B=2:1) may result in the withdrawal of the A component from the major Laves phase making it over-stoichiometric (B/A>2). In turn, it can result in the decrease of thermal stability of the AB₂ hydride. Indeed, the P-C isotherms (Figure 4.12) show that the plateau pressures for the oxygen-modified AB₂ sample are higher than the unmodified AB₂ sample.

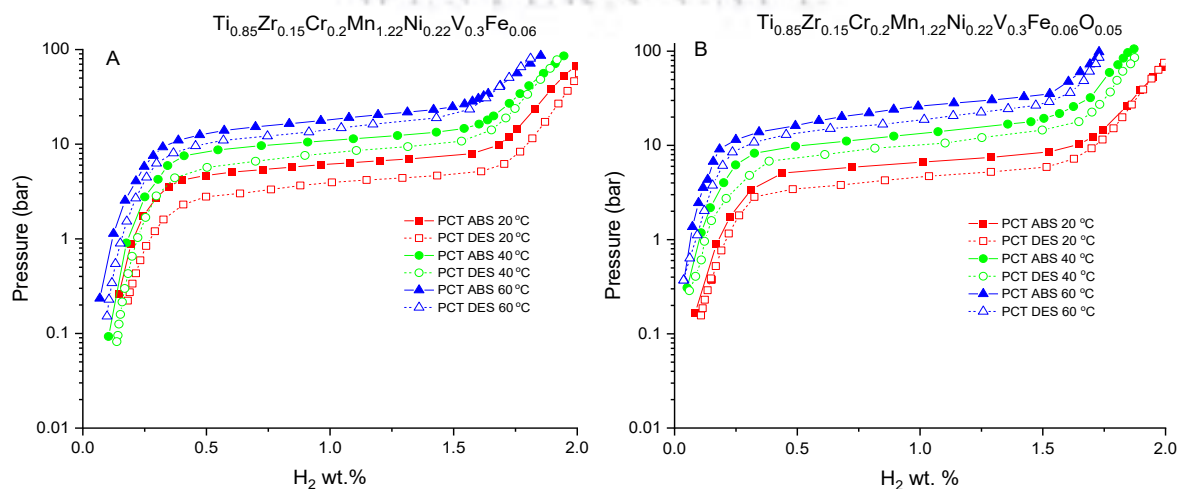


Figure 4. 12: Hydrogen absorption and desorption isotherms for Ti-Zr based AB₂ alloys (A) Unmodified AB₂, (B) Oxygen modified AB₂ alloy

The thermodynamic properties such as the enthalpies and entropies of formation and dissociation of the two hydrides were calculated from the Van't Hoff plots shown in Figure 4.13 (A) and (B). Good linear relationships were observed in the Van't Hoff plots for both alloys. The values for the enthalpy and entropy (ΔH and ΔS) for the unmodified sample obtained from Van't Hoff plots were calculated as -22.0 ± 0.6 kJ/mol H_2 and -90 ± 2 J/K/mol H_2 for absorption and 26.4 ± 0.7 kJ/mol H_2 and 102 ± 2 J/K/mol H_2 for desorption; the values for the modified sample are -27.8 ± 0.7 kJ/mol H_2 and -110 ± 2 J/K/mol H_2 for absorption and 28 ± 1 kJ/mol H_2 and 110 ± 4 J/K/mol H_2 for desorption.

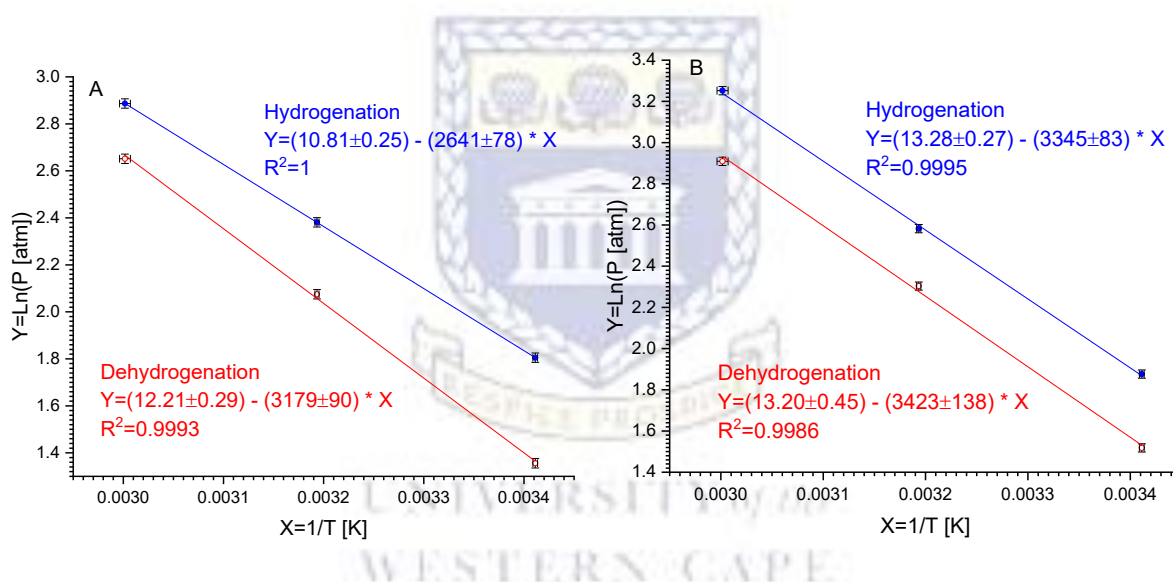


Figure 4. 13: Van't Hoff plots for hydrogen absorption and desorption for the unmodified (A) and modified (B) alloys.

4.2.5 Conclusions of Oxygen substitution on Ti-Zr based AB_2 alloy

The modification of Ti-Zr based AB_2 alloy by oxygen introduction was investigated. The results revealed that with the increase of oxygen content in the Ti-Zr based AB_2 alloy an increase in the abundance of η – phase ($Ti_4Fe_2O_{1-x}$) impurity occurs. The activation performance of the Ti-Zr based AB_2 alloy was improved by the introduction of oxygen into the alloy allowing it to absorb H_2 without any activation, but decreases its reversible hydrogen absorption capacity from 1.62 wt. % to 1.56 wt. %.

4.3 Effect of changing Ti-Zr ratio

A number of researchers have studied the effects of changing the Ti and Zr ratio in AB₂ alloys [78], [85], [114]. They have concluded that substituting Ti with Zr, plateau pressures decrease, since the atomic radius and hydrogen affinity of Zr is larger than that of Ti. In addition, the increase of Zr content also increases the hole size. Lundin *et al.*, [115] also suggested that the decrease of the plateau pressure is mainly contributed by the enlargement of interstitial size, which resulted from the increase of unit cell volume. In this work, the modification of the base alloy by changing the Ti and Zr ratio; Ti_{0,9}Zr_{0,1}Cr_{0,2}Mn_{1,2}Ni_{0,22}Cu_{0,02}V_{0,3}Fe_{0,06} and Ti_{0,8}Zr_{0,2}Cr_{0,2}Mn_{1,22}Ni_{0,22}Cu_{0,02}V_{0,3}Fe_{0,06} prepared by arc melting was studied.

4.3.1 Surface morphology and elemental composition of

Ti_{0,9}Zr_{0,1}Cr_{0,2}Mn_{1,2}Ni_{0,22}Cu_{0,02}V_{0,3}Fe_{0,06} and Ti_{0,8}Zr_{0,2}Cr_{0,2}Mn_{1,22}Ni_{0,22}Cu_{0,02}V_{0,3}Fe_{0,06}.

The SEM images of Ti_{0,9}Zr_{0,1}Cr_{0,2}Mn_{1,2}Ni_{0,22}Cu_{0,02}V_{0,3}Fe_{0,06} and Ti_{0,8}Zr_{0,2}Cr_{0,2}Mn_{1,22}Ni_{0,22}Cu_{0,02}V_{0,3}Fe_{0,06} prepared by arc melting are shown in Figure 4.14 (A and B). Both alloys exhibit smooth and continuous surface. The EDS data in Table 4.5(A) for Ti_{0,9}Zr_{0,1}Cr_{0,2}Mn_{1,2}Ni_{0,22}Cu_{0,02}V_{0,3}Fe_{0,06} reveal that despite Cr and Fe being present in the composition, it was absent in EDS data. This could be due to the increase in Ti, since the Ti atomic radii (0.147 nm) is larger than Cr (0.130 nm) and Fe (0.126 nm), and may occupy the B-sites of Cr and Fe [116]. This is not observed for Ti_{0,8}Zr_{0,2}Cr_{0,2}Mn_{1,22}Ni_{0,22}Cu_{0,02}V_{0,3}Fe_{0,06}. No impurities were present in both alloys.

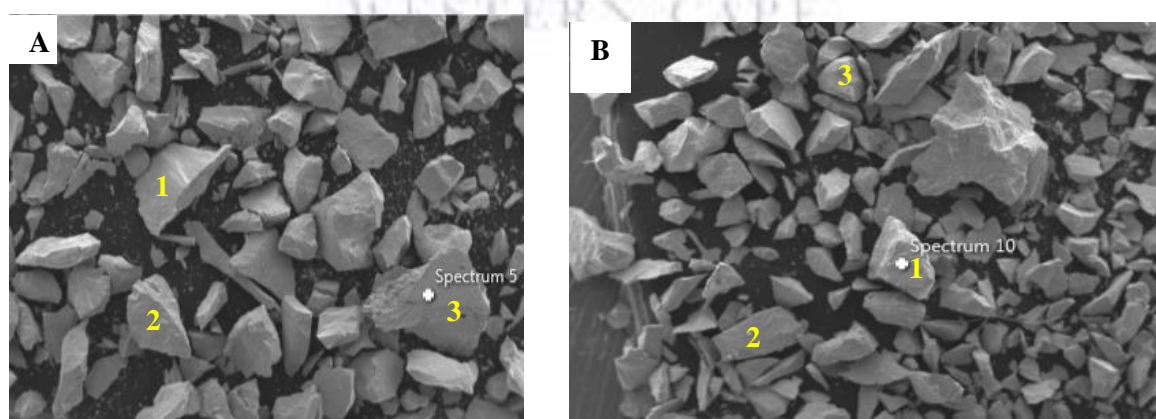


Figure 4.14: SEM images for the arc-melted samples: (A) Ti_{0,9}Zr_{0,1}Cr_{0,2}Mn_{1,2}Ni_{0,22}Cu_{0,02}V_{0,3}Fe_{0,06} and (B) Ti_{0,8}Zr_{0,2}Cr_{0,2}Mn_{1,22}Ni_{0,22}Cu_{0,02}V_{0,3}Fe_{0,06}.

Table 4. 5: EDS data of arc-melted (A) $Ti_{0,9}Zr_{0,1}Cr_{0,2}Mn_{1,2}Ni_{0,22}Cu_{0,02}V_{0,3}Fe_{0,06}$ and (B) $Ti_{0,8}Zr_{0,2}Cr_{0,2}Mn_{1,2}Ni_{0,22}Cu_{0,02}V_{0,3}Fe_{0,06}$.

Components	Content (wt%)									
	Arc melted									
	$Ti_{0,9}Zr_{0,1}Cr_{0,2}Mn_{1,2}Ni_{0,22}Cu_{0,02}V_{0,3}Fe_{0,06}$ (A)					$Ti_{0,8}Zr_{0,2}Cr_{0,2}Mn_{1,2}Ni_{0,22}Cu_{0,02}V_{0,3}Fe_{0,06}$ (B)				
	Nominal	Total area	Point 1	Point 2	Point 3	Nominal	Total area	Point 1	Point 2	Point 3
A (Ti)	32.79	30.20	29.74	31.14	29.47	22.22	23.87	21.09	21.96	23.52
A (Zr)	2.21	3.88	3.85	3.24	3.31	7.93	13.18	15.75	12.12	9.93
B (Cr)	-	-	-	-	-	6.40	5.30	6.21	6.20	5.26
B (Mn)	41.42	43.74	42.74	42.97	41.15	41.51	41.55	41.21	41.75	41.79
B (Ni)	7.61	8.59	8.14	8.23	7.41	5.94	5.71	5.06	5.77	5.95
B(Cu)	0.66	0.81	0.95	0.81	0.70	1.09	1.27	1.07	1.10	1.20
B (V)	12.07	11.82	11.57	13.61	11.66	9.31	9.43	8.70	9.22	9.85
B (Fe)	-	-	-	-	-	1.89	1.93	1.99	1.98	1.90



4.3.2 Phase and structural properties of $\text{Ti}_{0,9}\text{Zr}_{0,1}\text{Cr}_{0,2}\text{Mn}_{1,2}\text{Ni}_{0,22}\text{Cu}_{0,02}\text{V}_{0,3}\text{Fe}_{0,06}$ and $\text{Ti}_{0,8}\text{Zr}_{0,2}\text{Cr}_{0,2}\text{Mn}_{1,22}\text{Ni}_{0,22}\text{Cu}_{0,02}\text{V}_{0,3}\text{Fe}_{0,06}$

The phase structure of $\text{Ti}_{0,9}\text{Zr}_{0,1}\text{Cr}_{0,2}\text{Mn}_{1,2}\text{Ni}_{0,22}\text{Cu}_{0,02}\text{V}_{0,3}\text{Fe}_{0,06}$ and $\text{Ti}_{0,8}\text{Zr}_{0,2}\text{Cr}_{0,2}\text{Mn}_{1,22}\text{Ni}_{0,22}\text{Cu}_{0,02}\text{V}_{0,3}\text{Fe}_{0,06}$ was analysed by X-ray diffraction (XRD) and shown in Figure 4.15 (A and B), respectively. The refined XRD patterns show that the alloys contain a single C14 phase with no impurities, confirmed by EDS data (Table 4.5). The calculated abundancies and lattice periods of both alloys are summarized in Table 4.6. With the increase in Zr content, the diffraction peaks shift towards lower angles due to lattice expansion [81]. The increase in lattice periods and unit cell values may be attributed to the larger Zr atomic radii compared to Ti atomic radii [84].

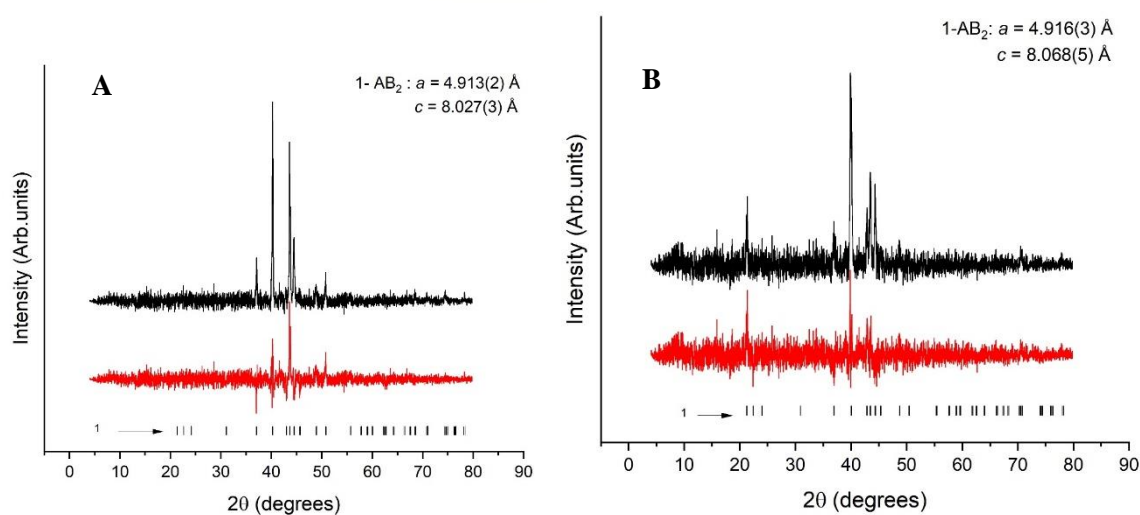


Figure 4. 15: XRD patterns of (A) $\text{Ti}_{0,9}\text{Zr}_{0,1}\text{Cr}_{0,2}\text{Mn}_{1,2}\text{Ni}_{0,22}\text{Cu}_{0,02}\text{V}_{0,3}\text{Fe}_{0,06}$ and (B) $\text{Ti}_{0,8}\text{Zr}_{0,2}\text{Cr}_{0,2}\text{Mn}_{1,22}\text{Ni}_{0,22}\text{Cu}_{0,02}\text{V}_{0,3}\text{Fe}_{0,06}$

Table 4. 6: Results of Rietveld refinement of the XRD patterns of the studied alloy samples (Figure 4.13). Errors of the values calculated during refinement (shown in brackets) relate to the last decimal digit.

Alloys	Phases	Abundance (wt%)	Lattice periods		Unit cell volume
			a (Å)	c (Å)	(Å ³)
$\text{Ti}_{0,9}\text{Zr}_{0,1}\text{Cr}_{0,2}\text{Mn}_{1,2}\text{Ni}_{0,22}\text{Cu}_{0,02}\text{V}_{0,3}\text{Fe}_{0,06}$	C14	100	4.913(2)	8.027(3)	167.8(1)
$\text{Ti}_{0,8}\text{Zr}_{0,2}\text{Cr}_{0,2}\text{Mn}_{1,22}\text{Ni}_{0,22}\text{Cu}_{0,02}\text{V}_{0,3}\text{Fe}_{0,06}$	C14	100	4.916(3)	8.068(5)	168.8(3)

4.3.3 Hydrogen sorption characteristics

The absorption and desorption isotherms of (A) $\text{Ti}_{0,9}\text{Zr}_{0,1}\text{Cr}_{0,2}\text{Mn}_{1,2}\text{Ni}_{0,22}\text{Cu}_{0,02}\text{V}_{0,3}\text{Fe}_{0,06}$ and (B) $\text{Ti}_{0,8}\text{Zr}_{0,2}\text{Cr}_{0,2}\text{Mn}_{1,2}\text{Ni}_{0,22}\text{Cu}_{0,02}\text{V}_{0,3}\text{Fe}_{0,06}$ at 20°, 40°, and 60°C are shown in Figure 4.16.

The maximum hydrogen storage capacity of $\text{Ti}_{0,9}\text{Zr}_{0,1}\text{Cr}_{0,2}\text{Mn}_{1,2}\text{Ni}_{0,22}\text{Cu}_{0,02}\text{V}_{0,3}\text{Fe}_{0,06}$ and $\text{Ti}_{0,8}\text{Zr}_{0,2}\text{Cr}_{0,2}\text{Mn}_{1,2}\text{Ni}_{0,22}\text{Cu}_{0,02}\text{V}_{0,3}\text{Fe}_{0,06}$ are approximately 1.8 wt% and 1.6 wt% H_2 at 20°C, respectively. It's clear with the increase in Zr content, the plateau pressures and hysteresis decreased, however the maximum hydrogen storage capacity decreased in Figure 4.16(B). The decrease in plateau pressure can be explained by the larger cell volume induced by Ti substituted by Zr. The reversible storage capacity of $\text{Ti}_{0,9}\text{Zr}_{0,1}\text{Cr}_{0,2}\text{Mn}_{1,2}\text{Ni}_{0,22}\text{Cu}_{0,02}\text{V}_{0,3}\text{Fe}_{0,06}$ and $\text{Ti}_{0,8}\text{Zr}_{0,2}\text{Cr}_{0,2}\text{Mn}_{1,2}\text{Ni}_{0,22}\text{Cu}_{0,02}\text{V}_{0,3}\text{Fe}_{0,06}$ are approximately 1.45 wt% and 1.17 wt% H_2 at 20°C, respectively.

The thermodynamic properties such as enthalpies and entropies of formation and dissociation was calculated from Van't Hoff plots shown in Figure 4.17 (A and B).

The ΔH and ΔS for $\text{Ti}_{0,9}\text{Zr}_{0,1}\text{Cr}_{0,2}\text{Mn}_{1,2}\text{Ni}_{0,22}\text{Cu}_{0,02}\text{V}_{0,3}\text{Fe}_{0,06}$ was (-51.332) kJ/mol H_2 and 183.18 J/K/mol H_2 for absorption. For desorption, the ΔH and ΔS was (-45.741) kJ/mol H_2 and 160.71 J/K/mol H_2 .

The ΔH and ΔS for $\text{Ti}_{0,8}\text{Zr}_{0,2}\text{Cr}_{0,2}\text{Mn}_{1,2}\text{Ni}_{0,22}\text{Cu}_{0,02}\text{V}_{0,3}\text{Fe}_{0,06}$ was (-16.565) kJ/mol H_2 and 59.233 J/K/mol H_2 . For desorption, the ΔH and ΔS was (-13.857) kJ/mol H_2 and 49.108 J/K/mol H_2 .

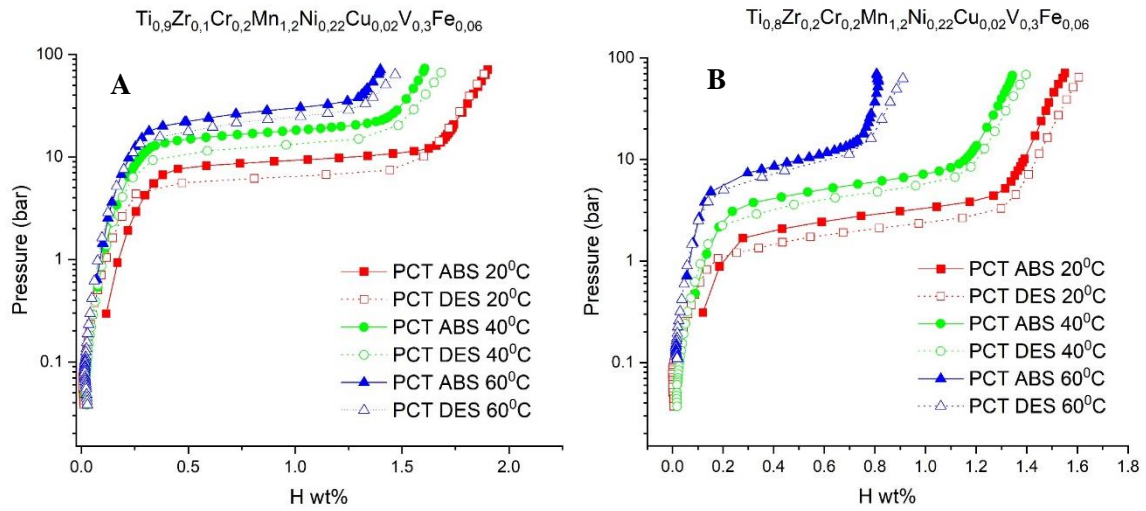


Figure 4. 16: PCT isotherms of (A) $Ti_{0.9}Zr_{0.1}Cr_{0.2}Mn_{1.2}Ni_{0.22}Cu_{0.02}V_{0.3}Fe_{0.06}$ and (B) $Ti_{0.8}Zr_{0.2}Cr_{0.2}Mn_{1.2}Ni_{0.22}Cu_{0.02}V_{0.3}Fe_{0.06}$ prepared by arc melting at different temperatures.

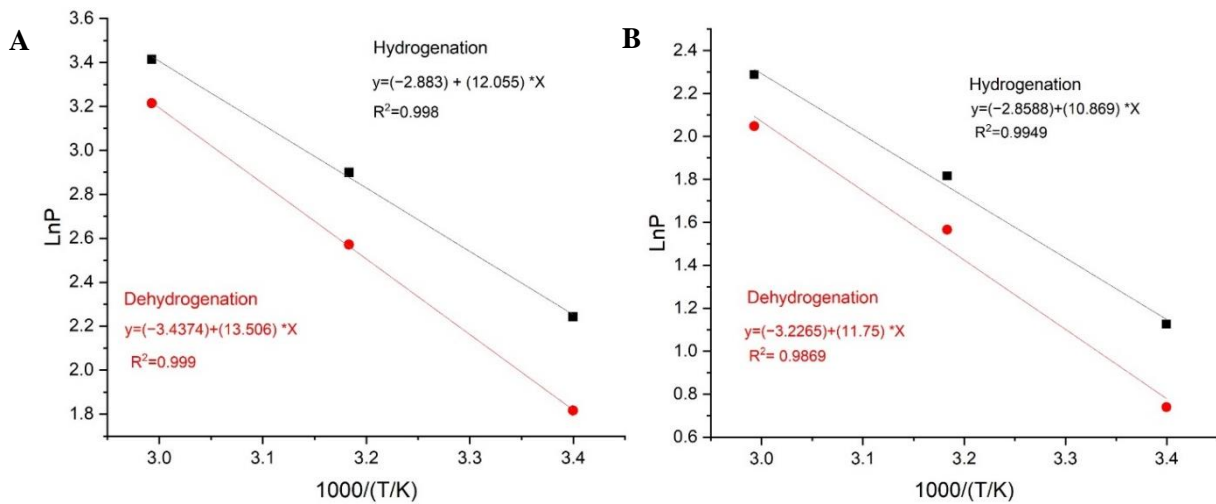


Figure 4. 17: Van't Hoff plots for hydrogen absorption and desorption for (A) $Ti_{0.9}Zr_{0.1}Cr_{0.2}Mn_{1.2}Ni_{0.22}Cu_{0.02}V_{0.3}Fe_{0.06}$ and (B) $Ti_{0.8}Zr_{0.2}Cr_{0.2}Mn_{1.2}Ni_{0.22}Cu_{0.02}V_{0.3}Fe_{0.06}$

4.3.4 Conclusions on the effect of changing Ti-Zr ratio

The effect of changing the Ti-Zr ratio of $\text{Ti}_{0,9}\text{Zr}_{0,1}\text{Cr}_{0,2}\text{Mn}_{1,2}\text{Ni}_{0,22}\text{Cu}_{0,02}\text{V}_{0,3}\text{Fe}_{0,06}$ and $\text{Ti}_{0,8}\text{Zr}_{0,2}\text{Cr}_{0,2}\text{Mn}_{1,2}\text{Ni}_{0,22}\text{Cu}_{0,02}\text{V}_{0,3}\text{Fe}_{0,06}$, revealed that with the increase of Zr, decreased the plateau pressures and hysteresis however, decreased the maximum hydrogen storage capacity from 1.8 wt.% to 1.6 wt.%, respectively. No secondary phases or impurities were present in both alloys, and confirmed by EDS data (Table 4.5).



UNIVERSITY of the
WESTERN CAPE

4.4 The effect of Ferrovandium on the base alloy

An approach to reduce raw material cost is to substitute expensive and rare materials with less expensive and more abundant raw materials while minimizing negative effects on the performance of the resulting hydrogen storage alloy. An effective strategy to decrease the cost of Ti-Mn-V alloy is to replace V with inexpensive ferrovanadium (FeV). However, it was reported that with the replacement of V with FeV, the hydrogen storage capacities decreased and increased the plateau slope [63], [117], [118]. In this work, the base alloy was modified by replacing pure V with ferrovanadium (FeV) prepared by arc melting.

4.4.1 Surface morphology and elemental composition of $\text{Ti}_{0,85}\text{Zr}_{0,15}\text{Cr}_{0,2}\text{Mn}_{1,2}\text{Ni}_{0,22}\text{Cu}_{0,02}\text{FeV}_{0,42}$.

The surface morphology and elemental composition of $\text{Ti}_{0,85}\text{Zr}_{0,15}\text{Cr}_{0,2}\text{Mn}_{1,2}\text{Ni}_{0,22}\text{Cu}_{0,02}\text{FeV}_{0,42}$ was carried out by SEM and EDS, respectively. The SEM image of the modified $\text{Ti}_{0,85}\text{Zr}_{0,15}\text{Cr}_{0,2}\text{Mn}_{1,2}\text{Ni}_{0,22}\text{Cu}_{0,02}\text{FeV}_{0,42}$ alloy was shown in Figure 4.18. Due to the impurities due to Ferrovanadium (FeV), the secondary phases can be seen on the surface in Figure 4.18 (b). In Figure 4.18 (a) and Table 4.7 the EDS of $\text{Ti}_{0,85}\text{Zr}_{0,15}\text{Cr}_{0,2}\text{Mn}_{1,2}\text{Ni}_{0,22}\text{Cu}_{0,02}\text{FeV}_{0,42}$ was shown. It was revealed that a secondary phase of Silicon was found in the sample. To confirm the secondary phases of FeV, a reference scanned EDS image along with elemental composition data was shown in Figure 4.18(b) and Table 4.8.

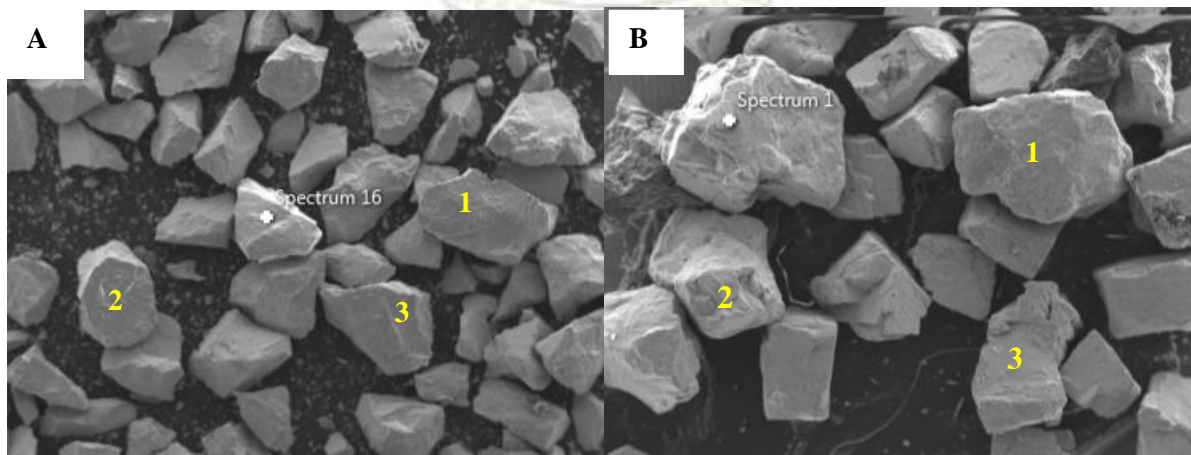


Figure 4. 18: SEM image of (A) $\text{Ti}_{0,85}\text{Zr}_{0,15}\text{Cr}_{0,2}\text{Mn}_{1,2}\text{Ni}_{0,22}\text{Cu}_{0,02}\text{FeV}_{0,42}$ and (B) pure FeV at low magnification.

Table 4. 7: EDS data of arc-melted $\text{Ti}_{0,85}\text{Zr}_{0,15}\text{Cr}_{0,2}\text{Mn}_{1,2}\text{Ni}_{0,22}\text{Cu}_{0,02}\text{FeV}_{0,42}$

Content (wt%)					
$\text{Ti}_{0,85}\text{Zr}_{0,15}\text{Cr}_{0,2}\text{Mn}_{1,2}\text{Ni}_{0,22}\text{Cu}_{0,02}\text{FeV}_{0,42}$					
Components	Nominal	Total area	Point 1	Point 2	Point 3
A(Ti)	27.97	27.42	26.43	26.07	25.63
A(Zr)	2.86	5.34	7.11	6.20	7.93
B(Cr)	5.05	5.37	5.90	6.28	7.24
B(Mn)	39.18	44.05	44.66	46.10	46.91
B(Ni)	4.89	5.87	5.54	5.07	4.02
B(Cu)	-	-	-	-	-
B(V)	8.56	8.92	8.33	8.26	8.26
B(Fe)	-	-	1.38	1.47	-
Impurity (Si)	0.23	0.31	-	-	-

Table 4. 8: EDS data of pure FeV

Content (wt%)					
FeV					
Components	Nominal	Total area	Point 1	Point 2	Point 3
O	19.27	6.96	22.17	16.36	30.92
Al	0.85	0.52	1.21	0.84	2.11
Si	6.16	3.90	10.15	3.73	3.15
Ca	0.26	0.23	1.82	0.59	0.32
V	6.87	7.89	54.25	63.20	50.76
Cr	39.16	45.93	-	-	-
Fe	27.44	34.57	9.05	14.90	12.14
Mg	-	-	0.39	0.27	0.23
W	-	-	0.96	-	-
P	-	-	-	-	0.12
S	-	-	-	-	0.14
Cl	-	-	-	-	0.10

4.4.2 Phase structure

The XRD patterns of $\text{Ti}_{0,85}\text{Zr}_{0,15}\text{Cr}_{0,2}\text{Mn}_{1,2}\text{Ni}_{0,22}\text{Cu}_{0,02}\text{FeV}_{0,42}$ is shown in Figure 4.19. The alloy consists of a single C14 phase, even though in the EDS data (Table 4.7), an impurity of silicon is observed (value too small). The lattice periods, a and c , are $4.927(2) \text{ \AA}$ and $8.090(4) \text{ \AA}$, respectively. The unit cell volume is $170.0(2) \text{ \AA}^3$. Very narrow XRD peaks specify about high crystallinity of the C14 phase; the calculated crystallite size significantly exceeds the value of 100–200 nm above which the size calculations from XRD data become untrustable [105], [106].

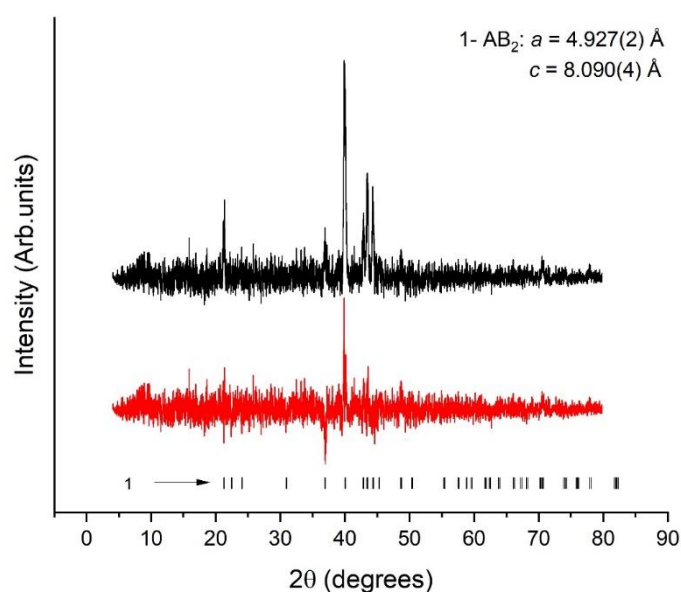


Figure 4. 19: Refined XRD patterns of $\text{Ti}_{0,85}\text{Zr}_{0,15}\text{Cr}_{0,2}\text{Mn}_{1,2}\text{Ni}_{0,22}\text{Cu}_{0,02}\text{FeV}_{0,42}$

4.4.3 Hydrogen sorption characteristics

The absorption and desorption isotherms at 20°, 40°, and 60°C for $\text{Ti}_{0,85}\text{Zr}_{0,15}\text{Cr}_{0,2}\text{Mn}_{1,2}\text{Ni}_{0,22}(\text{FeV})_{0,42}$ was shown in Figure 4.20(A). Similar to the base alloy, $\text{Ti}_{0,85}\text{Zr}_{0,15}\text{Cr}_{0,2}\text{Mn}_{1,2}\text{Ni}_{0,22}(\text{FeV})_{0,42}$ exhibits a α -solid solution and β -hydride phase. However, due to FeV, the slope of the α -solid solution phase is steep. This may be due to inhomogeneity and/or impurities introduced by FeV. The maximum hydrogen storage capacity for the alloy was approximately 1.5 wt% H_2 at 20°C and 90 bar. The reversible hydrogen storage was approximately 1.0 wt% H_2 at 20°C

The thermodynamic properties such as enthalpies and entropies of formation and dissociation was calculated from Van't Hoff plots shown in Figure 4.20(B). The ΔH and ΔS of $\text{Ti}_{0,85}\text{Zr}_{0,15}\text{Cr}_{0,2}\text{Mn}_{1,2}\text{Ni}_{0,22}(\text{FeV})_{0,42}$ was (-18.023) kJ/mol H_2 and 67.658 J/K/mol H_2 for absorption. For desorption, ΔH and ΔS was (-16.611) kJ/mol H_2 and 60.809 J/K/mol H_2 , respectively.

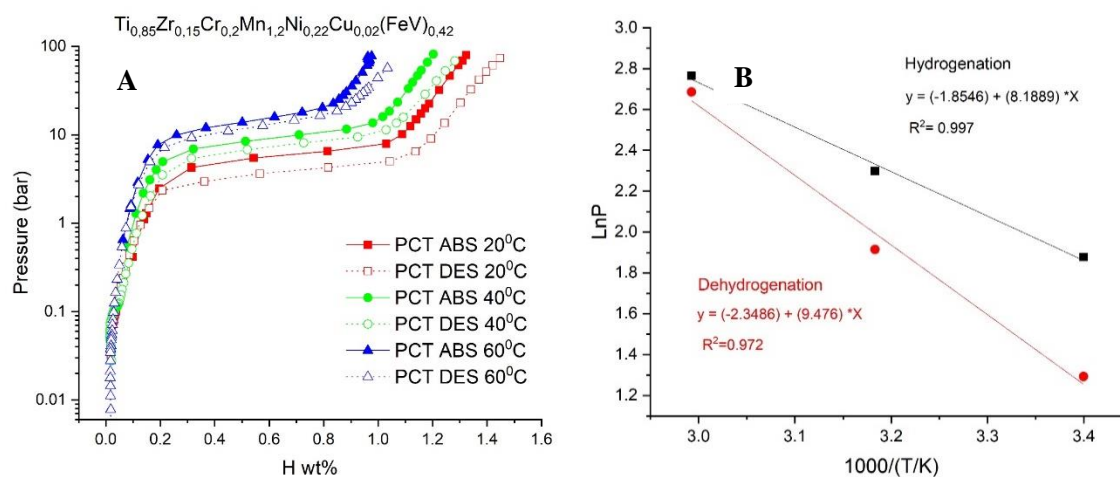


Figure 4. 20: (A) PCT isotherms of $\text{Ti}_{0,85}\text{Zr}_{0,15}\text{Cr}_{0,2}\text{Mn}_{1,2}\text{Ni}_{0,22}\text{Cu}_{0,02}\text{FeV}_{0,42}$, (B) van't Hoff plots for hydrogen absorption and desorption of $\text{Ti}_{0,85}\text{Zr}_{0,15}\text{Cr}_{0,2}\text{Mn}_{1,2}\text{Ni}_{0,22}\text{Cu}_{0,02}\text{FeV}_{0,42}$.

4.4.4 Conclusion on the effect of Ferrovandium on base alloy

The modification of the base alloy by introduction of ferrovandium was studied. Due to the impurities introduced by FeV, the maximum hydrogen storage capacity was 1.5 wt.%. However, the XRD pattern showed a single C14 phase with no additional phases/impurities.

4.5 Effect of Chromium/Manganese substitution on the base alloy

The effect of Chromium (Cr)/Manganese substitution on the base alloy prepared by arc melting was studied. The Cr substitution values were ranged from $x=0, 0.3,$ and $0.6,$ respectively. The Mn substitution values were ranged from $y=1.4, 1.1,$ and $0.8,$ respectively. The three alloys were characterized by SEM/EDS, XRD, and Hydrogen sorption (Sievert's method).

4.5.1 Surface morphology and elemental composition of $\text{Ti}_{0,85}\text{Zr}_{0,15}\text{Mn}_{1,4}\text{Ni}_{0,22}\text{Cu}_{0,02}\text{Fe}_{0,06}\text{V}_{0,3},$ $\text{Ti}_{0,85}\text{Zr}_{0,15}\text{Cr}_{0,3}\text{Mn}_{1,1}\text{Ni}_{0,22}\text{Cu}_{0,02}\text{Fe}_{0,06}\text{V}_{0,3},$ and $\text{Ti}_{0,85}\text{Zr}_{0,15}\text{Cr}_{0,6}\text{Mn}_{0,8}\text{Ni}_{0,22}\text{Cu}_{0,02}\text{Fe}_{0,06}\text{V}_{0,3}.$

The surface morphology and elemental composition of the Cr substituted alloys were analysed by SEM and EDS, respectively. The SEM images of the three alloys exhibit similar properties (Figure 4.21 (a-c)); smooth continuous surfaces. The EDS data (Table 4.9), confirm the absence of Cr in $\text{Ti}_{0,85}\text{Zr}_{0,15}\text{Mn}_{1,4}\text{Ni}_{0,22}\text{Cu}_{0,02}\text{Fe}_{0,06}\text{V}_{0,3}$ alloy. No impurities were present for $\text{Ti}_{0,85}\text{Zr}_{0,15}\text{Mn}_{1,4}\text{Ni}_{0,22}\text{Cu}_{0,02}\text{Fe}_{0,06}\text{V}_{0,3}$ and $\text{Ti}_{0,85}\text{Zr}_{0,15}\text{Cr}_{0,3}\text{Mn}_{1,1}\text{Ni}_{0,22}\text{Cu}_{0,02}\text{Fe}_{0,06}\text{V}_{0,3},$ however, in $\text{Ti}_{0,85}\text{Zr}_{0,15}\text{Cr}_{0,6}\text{Mn}_{0,8}\text{Ni}_{0,22}\text{Cu}_{0,02}\text{Fe}_{0,06}\text{V}_{0,3}$ an oxygen impurity was present.

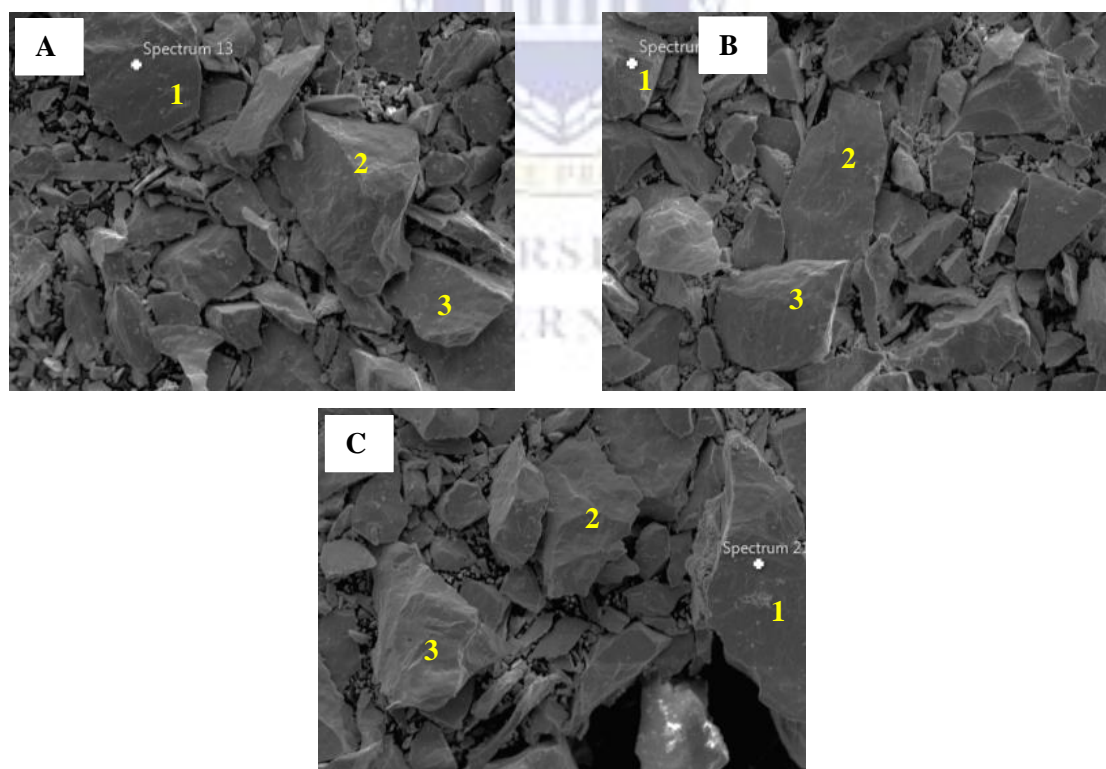


Figure 4. 21: Surface morphology of (A) $\text{Ti}_{0,85}\text{Zr}_{0,15}\text{Mn}_{1,4}\text{Ni}_{0,22}\text{Cu}_{0,02}\text{Fe}_{0,06}\text{V}_{0,3},$ (B) $\text{Ti}_{0,85}\text{Zr}_{0,15}\text{Cr}_{0,3}\text{Mn}_{1,1}\text{Ni}_{0,22}\text{Cu}_{0,02}\text{Fe}_{0,06}\text{V}_{0,3},$ and (C) $\text{Ti}_{0,85}\text{Zr}_{0,15}\text{Cr}_{0,6}\text{Mn}_{0,8}\text{Ni}_{0,22}\text{Cu}_{0,02}\text{Fe}_{0,06}\text{V}_{0,3}.$

Table 4. 9: EDS data of Cr substituted alloys prepared by arc melting.

Components	Content (wt%)														
	Arc melted														
	Ti _{0,85} Zr _{0,15} Mn _{1,4} Ni _{0,22} Cu _{0,02} Fe _{0,06} V _{0,3} (A)					Ti _{0,85} Zr _{0,15} Cr _{0,3} Mn _{1,1} Ni _{0,22} Cu _{0,02} Fe _{0,06} V _{0,3} (B)					Ti _{0,85} Zr _{0,15} Cr _{0,6} Mn _{0,8} Ni _{0,22} Cu _{0,02} Fe _{0,06} V _{0,3} (C)				
	Nominal	Total area	Spot 1	Spot 2	Spot 3	Nominal	Total area	Spot 1	Spot 2	Spot 3	Nominal	Total area	Spot 1	Spot 2	Spot 3
A (Ti)	25.51	24.90	23.47	23.97	26.77	25.13	25.02	25.11	24.76	23.29	42.77	46.15	25.91	23.54	26.09
A (Zr)	3.93	7.31	7.82	8.57	5.48	3.79	7.19	6.36	7.19	9.30	1.10	2.27	6.71	9.27	6.61
B (Cr)	-	-	-	-	-	6.86	7.41	8.68	8.76	10.64	2.31	2.70	14.14	18.37	14.25
B (Mn)	40.69	45.56	44.34	46.50	47.06	31.40	35.86	37.30	37.50	37.72	8.05	9.97	27.49	27.29	27.17
B (Ni)	7.25	8.67	7.18	5.97	8.18	7.04	8.59	7.44	6.34	4.79	13.32	17.61	9.76	6.33	9.18
B (Cu)	0.65	0.84	0.69	-	0.66	0.80	1.06	0.66	-	-	1.49	2.14	1.36	0.65	1.22
B (V)	9.24	9.60	9.03	9.15	10.07	9.08	9.61	9.78	9.68	8.82	8.27	9.49	10.56	8.95	10.45
B (Fe)	-	-	1.73	-	-	1.42	1.65	1.86	1.80	2.00	0.84	1.06	1.75	2.08	1.75
Impurity (O)	-	-	-	-	-	-	-	-	-	-	10.46	3.77	-	-	-



4.5.2 Phase structure

The phase structure of $\text{Ti}_{0,85}\text{Zr}_{0,15}\text{Mn}_{1,4}\text{Ni}_{0,22}\text{Cu}_{0,02}\text{Fe}_{0,06}\text{V}_{0,3}$, $\text{Ti}_{0,85}\text{Zr}_{0,15}\text{Cr}_{0,3}\text{Mn}_{1,1}\text{Ni}_{0,22}\text{Cu}_{0,02}\text{Fe}_{0,06}\text{V}_{0,3}$, and $\text{Ti}_{0,85}\text{Zr}_{0,15}\text{Cr}_{0,6}\text{Mn}_{0,8}\text{Ni}_{0,22}\text{Cu}_{0,02}\text{Fe}_{0,06}\text{V}_{0,3}$ are shown in Figure 4.22(A-C), respectively. The lattice periods are summarised in Table 4.10. All alloys exhibit single C14 phases, with no impurities, even though in Table 4.9(C), an oxygen impurity is present. Though the atomic radii of Cr (1.27 Å) is smaller than that of Mn (1.32 Å), the increase of Cr content, increased the lattice periods and unit cells. This may be due to their electronic structure [75].

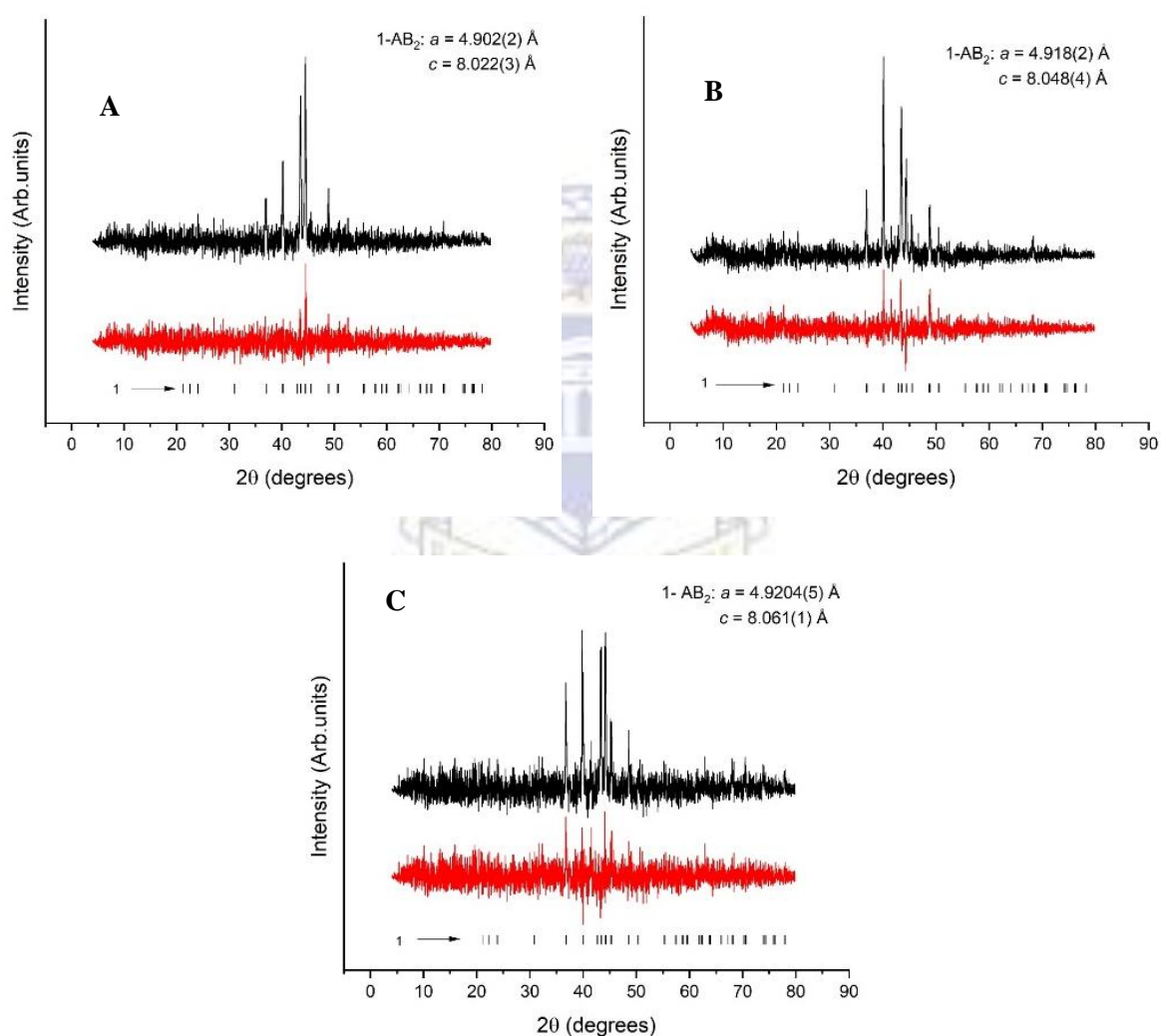


Figure 4. 22: XRD patterns of (a) $\text{Ti}_{0,85}\text{Zr}_{0,15}\text{Mn}_{1,4}\text{Ni}_{0,22}\text{Cu}_{0,02}\text{Fe}_{0,06}\text{V}_{0,3}$, (b) $\text{Ti}_{0,85}\text{Zr}_{0,15}\text{Cr}_{0,3}\text{Mn}_{1,1}\text{Ni}_{0,22}\text{Cu}_{0,02}\text{Fe}_{0,06}\text{V}_{0,3}$, and (c) $\text{Ti}_{0,85}\text{Zr}_{0,15}\text{Cr}_{0,6}\text{Mn}_{0,8}\text{Ni}_{0,22}\text{Cu}_{0,02}\text{V}_{0,3}\text{Fe}_{0,06}$

Table 4. 10: Results of Rietveld refinement of the XRD patterns of the studied alloy samples (Figure 4.18). Errors of the values calculated during refinement (shown in brackets) relate to the last decimal digit.

Alloys	Phases	Abundance (wt%)	Lattice periods		Unit cell volume
			<i>a</i> (Å)	<i>c</i> (Å)	(Å ³)
Ti _{0,85} Zr _{0,15} Mn _{1,4} Ni _{0,22} Cu _{0,02} Fe _{0,06} V _{0,3}	C14	100	4.902(2)	8.022(3)	166.9(2)
Ti _{0,85} Zr _{0,15} Cr _{0,3} Mn _{1,1} Ni _{0,22} Cu _{0,02} Fe _{0,06} V _{0,3}	C14	100	4.918(2)	8.048(4)	168.6(2)
Ti _{0,85} Zr _{0,15} Cr _{0,6} Mn _{0,8} Ni _{0,22} Cu _{0,02} Fe _{0,06} V _{0,3}	C14	100	4.920(5)	8.061(1)	169.0(3)

4.5.3 Hydrogen sorption characteristics

The absorption and desorption isotherms for Ti_{0,85}Zr_{0,15}Mn_{1,4}Ni_{0,22}Cu_{0,02}Fe_{0,06}V_{0,3}, Ti_{0,85}Zr_{0,15}Cr_{0,3}Mn_{1,1}Ni_{0,22}Cu_{0,02}Fe_{0,06}V_{0,3}, and Ti_{0,85}Zr_{0,15}Cr_{0,6}Mn_{0,8}Ni_{0,22}Cu_{0,02}Fe_{0,06}V_{0,3} was shown in Figure 4.23 (A-C).

With the increase of Cr content from 0.3 to 0.6, the maximum hydrogen storage capacity decreased from 1.7 wt.% H₂ at 40°C to 1.6 wt.% H₂ at 20°C, respectively. The alloy containing no Cr content, maximum hydrogen storage capacity was approximately 1.8 wt.% H₂ at 20°C. With the increased Cr content, the plateau region becomes narrower, with an increased slope, hence leading to a smaller hydrogen storage capacity[119]. The reversible hydrogen storage for alloy Ti_{0,85}Zr_{0,15}Mn_{1,4}Ni_{0,22}Cu_{0,02}Fe_{0,06}V_{0,3} and Ti_{0,85}Zr_{0,15}Cr_{0,3}Mn_{1,1}Ni_{0,22}Cu_{0,02}Fe_{0,06}V_{0,3} were 1.4 wt.% and 1.1 wt.%, respectively.

The thermodynamic properties such as enthalpies and entropies of formation and dissociation was calculated from Van't Hoff plots shown in Figure 4.24(A-C). The ΔH and ΔS of Ti_{0,85}Zr_{0,15}Mn_{1,4}Ni_{0,22}Cu_{0,02}Fe_{0,06}V_{0,3} for absorption was (-47.435) kJ/mol H₂ and 169.83 J/K/mol H₂, respectively. For desorption, ΔH and ΔS was (-34.072) kJ/mol H₂ and 120.03 J/K/mol H₂, respectively.

The ΔH and ΔS of Ti_{0,85}Zr_{0,15}Cr_{0,3}Mn_{1,1}Ni_{0,22}Cu_{0,02}Fe_{0,06}V_{0,3} for absorption was (-23.228) kJ/mol H₂ and 83.846 J/K/mol H₂, respectively. For desorption, ΔH and ΔS was (-22.18) kJ/mol H₂ and 78.899 J/K/mol H₂, respectively.

The ΔH and ΔS of Ti_{0,85}Zr_{0,15}Cr_{0,6}Mn_{0,8}Ni_{0,22}Cu_{0,02}Fe_{0,06}V_{0,3} for absorption was (-21.18) kJ/mol H₂ and 75.454 J/K/mol H₂, respectively. For desorption, ΔH and ΔS was (-21.166) kJ/mol H₂ and 74.842 J/K/mol H₂.

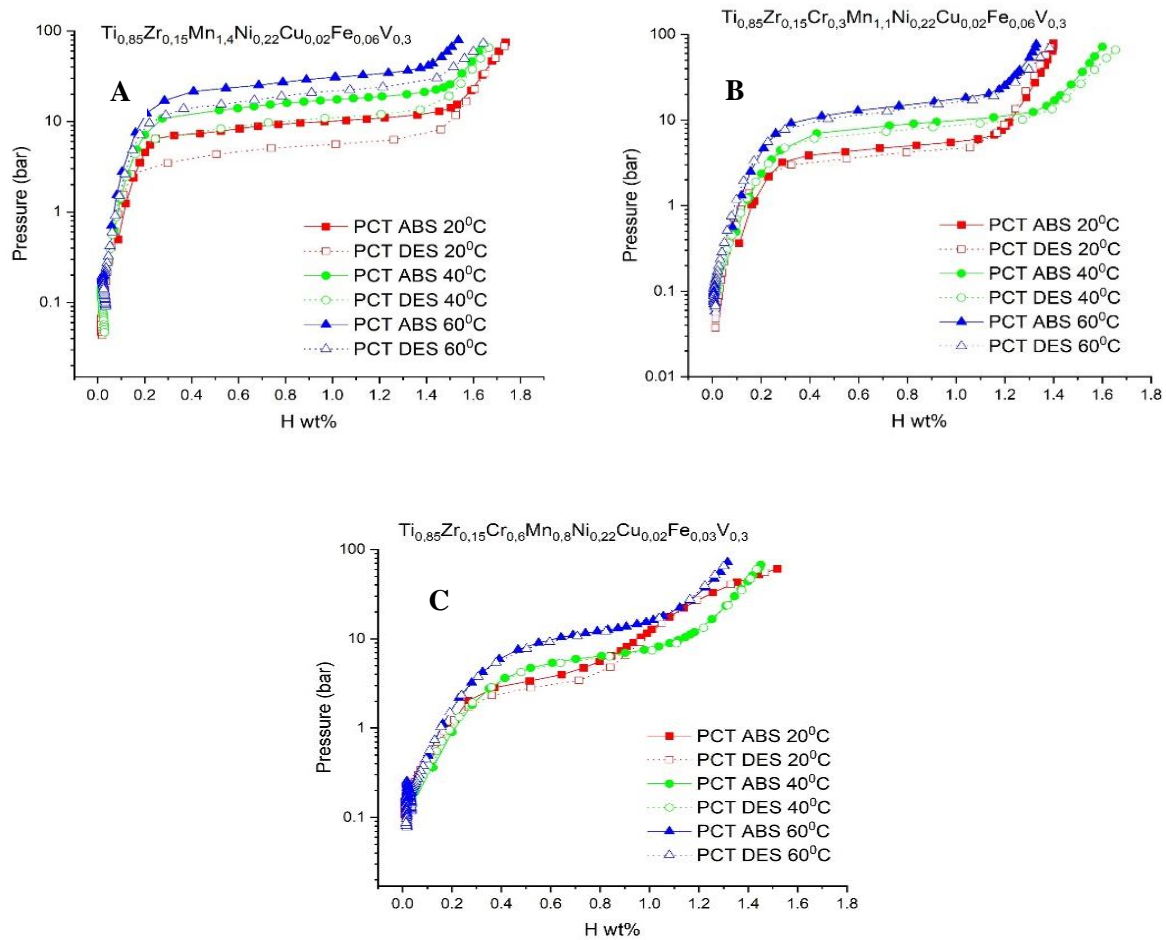


Figure 4. 23: PCT isotherms of (A) $\text{Ti}_{0.85}\text{Zr}_{0.15}\text{Mn}_{1.4}\text{Ni}_{0.22}\text{Cu}_{0.02}\text{Fe}_{0.06}\text{V}_{0.3}$, (B) $\text{Ti}_{0.85}\text{Zr}_{0.15}\text{Cr}_{0.3}\text{Mn}_{1.1}\text{Ni}_{0.22}\text{Cu}_{0.02}\text{Fe}_{0.06}\text{V}_{0.3}$, and (C) $\text{Ti}_{0.85}\text{Zr}_{0.15}\text{Cr}_{0.6}\text{Mn}_{0.8}\text{Ni}_{0.22}\text{Cu}_{0.02}\text{Fe}_{0.06}\text{V}_{0.3}$ prepared by arc melting at different temperatures.

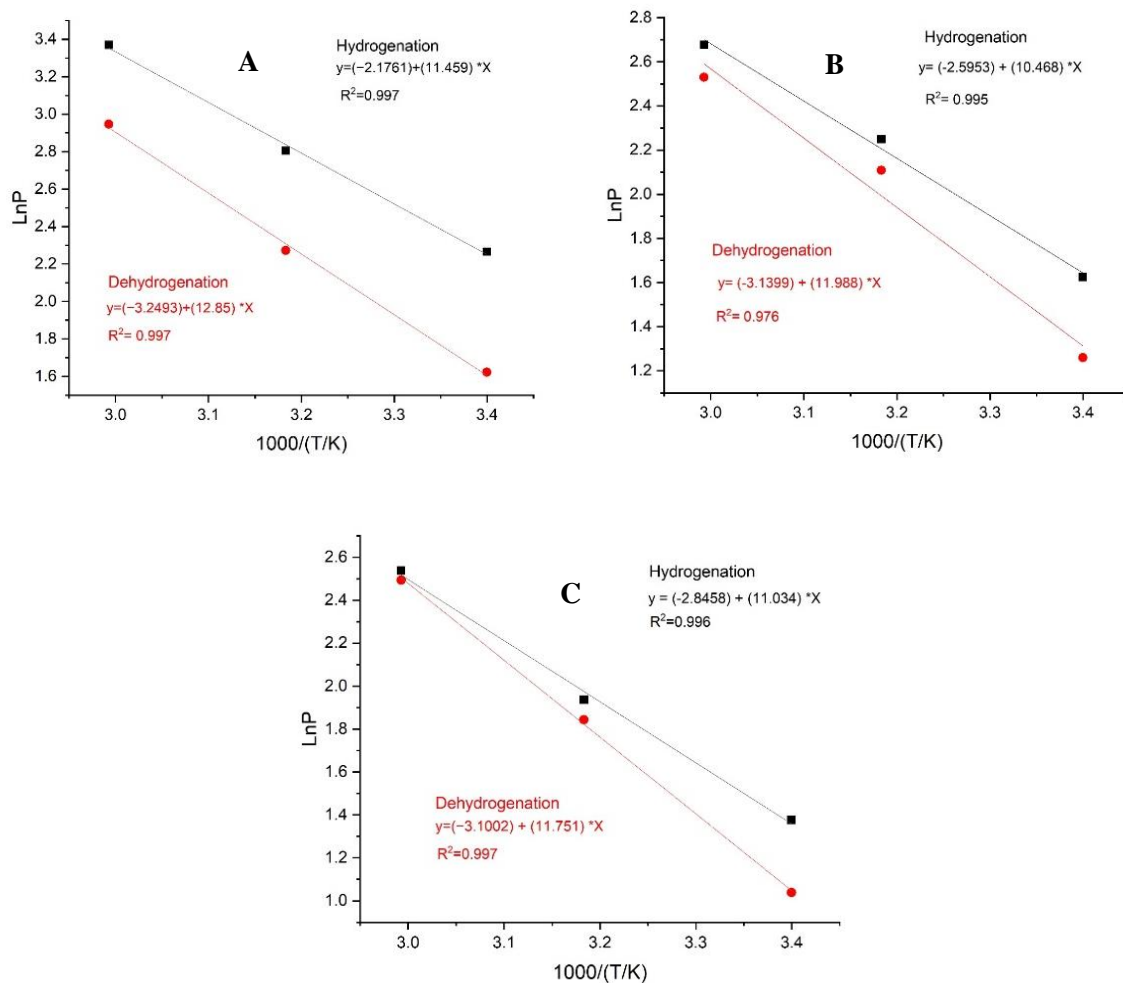


Figure 4. 24: Van't Hoff plots for hydrogen absorption and desorption for (A) $Ti_{0,85}Zr_{0,15}Mn_{1,4}Ni_{0,22}Cu_{0,02}Fe_{0,06}V_{0,3}$, (B) $Ti_{0,85}Zr_{0,15}Cr_{0,3}Mn_{1,1}Ni_{0,22}Cu_{0,02}Fe_{0,06}V_{0,3}$, and (C) $Ti_{0,85}Zr_{0,15}Cr_{0,6}Mn_{0,8}Ni_{0,22}Cu_{0,02}Fe_{0,06}V_{0,3}$.

4.5.4 Conclusion on the effect of Cr substitution on base alloy

The substitution of Cr/Mn on the base alloy was investigated. The results revealed that with the increase of Cr content, decreased the hydrogen storage capacity and narrows plateau pressures. The XRD patterns showed that all alloys contained a single C14 phase, despite having an impurity in the EDS data (Table 4.9(C)).

5. Conclusion and Future prospects

The main objective of this project was to study the upscaling effects of Ti-Zr based intermetallic compounds belonging to AB₂ (A=Ti, Zr; B= Mn, Cr, Fe, V, Ni, Cu).

The Ti-Zr based AB₂ metal hydride was prepared by arc melting and induction melting followed by various characterization techniques; SEM/EDS, XRD, TEM/SAED, AES, Sievert's method (hydrogen sorption measurements).

Results of the preparation routes and characterization methods were summarised as follows:

1. The synthesis of the Ti-Zr based AB₂ prepared by arc melting was used as the base alloy. The XRD results proved that the alloy exhibited a single phase C14 phase with no impurities, which was further confirmed by the EDS data. The hydrogen sorption measurements revealed that the alloy exhibited an α -solid solution phase and β -hydride phase. The maximum storage capacity is approximately 1.8 wt% H₂ at 90 bar and 20°C.
2. The synthesis of Ti-Zr based AB₂ prepared by induction melting with an alumo-silica crucible and graphite crucible with a yttria coating. Even though both crucibles were coated with yttria, the XRD results revealed that both alloys contained a C14 phase, however both alloys presented with a La₂TiO₅ impurity. The AES results also confirmed the presence of oxygen impurity in both alloys. The PCT measurements showed a decrease in maximum hydrogen storage (1.4 wt% alumo silica crucible, 1.6 wt% graphite crucible) compared to the base alloy (1.8 wt%) which may be due to the impurities. The higher plateaus may be due to inhomogeneous composition.
3. The effect of Oxygen addition was also studied by arc melting. The XRD results revealed a secondary phase (η -phase; Ti₄Fe₂O_{1-x}) with an abundance of 2.3 %. Hydrogen absorption kinetics showed that the modified oxygen alloy was slighter slower compared to the base alloy after activation by vacuum heating. However, in the non-activated state, the modified oxygen alloy absorbed hydrogen immediately, while the non-activated base alloy had an incubation period of 30 min. The reason for the immediate hydrogen absorption was due to the impurity phase acting as a catalyst, however, the introduction of oxygen led to a decrease in hydrogen storage.
4. The effect of Ti_{0,9}Zr_{0,1}Cr_{0,2}Mn_{1,2}Ni_{0,22}Cu_{0,02}V_{0,3}Fe_{0,06} and Ti_{0,8}Zr_{0,2}Cr_{0,2}Mn_{1,22}Ni_{0,22}Cu_{0,02}V_{0,3}Fe_{0,06} was also studied. The XRD results showed that both alloys contained a single C14 phase with no impurities. With the increase in Zr content, the diffraction peaks shifted towards lower angles due to the lattice

expansion. Also, the lattice periods and unit cell volumes increased with increased Zr content due to larger atomic Zr radii than Ti. The hydrogen sorption measurements revealed that with the increase of Zr content, the hydrogen storage decreased.

5. Since V is expensive, a cheaper alternative such as FeV was used to investigate any changes and compare it to the base alloy. $\text{Ti}_{0,85}\text{Zr}_{0,15}\text{Cr}_{0,2}\text{Mn}_{1,2}\text{Ni}_{0,22}\text{Cu}_{0,02}\text{FeV}_{0,42}$ was characterized by XRD, which revealed no impurity phase however, in the EDS data, a silicon impurity was found. Also the hydrogen storage capacity was 1.5 wt%.
6. The effect of Cr/Mn was also studied. With the increase of Cr content, and decrease in Mn content, the lattice periods and unit cell volumes increased, even though Cr atomic radii is smaller than that of Mn atomic radii. The hydrogen storage capacities decreased with increasing Cr content, with increased plateau slopes.

Based on the results and conclusions of this study, a few recommendations regarding future research in this field should include:

1. Focus on upscaling of Ti-based AB_2 metal hydrides where $\text{A}=\text{Ti}$, Zr , $\text{B}=\text{Mn}$, Cr , Fe , V , Cu , Ni , and to increase the yield of the target alloy.
2. Research on crucible materials primarily used for upscaling that may be improved to withstand molten Ti for Ti-based AB_2 metal hydrides.
3. Efforts to reduce crucible melt interactions by changing the preparation route such as levitation induction melting or cold crucible melting may also reduce impurities which may affect the hydrogen storage capacity.
4. A look into cheaper alternatives such as sponge Ti and FeV, to replace pure Ti and V.

References

- [1] M. V Lototsky, I. Tolj, L. Pickering, C. Sita, and F. Barbir, "Progress in Natural Science: Materials International The use of metal hydrides in fuel cell applications," *Prog. Nat. Sci. Mater. Int.*, vol. 27, no. 1, pp. 3–20, 2017.
- [2] S. S. Makridis, "Hydrogen storage and compression," *Methane Hydrog. Energy Storage*, pp. 1–13, 2016.
- [3] L. Schlapbach and A. Züttel, "Hydrogen storage materials for mobile applications," *Nature*, vol. 414, no. November, pp. 353–358, 2001.
- [4] I. Dincer and M. A. Rosen, "Sustainability aspects of hydrogen and fuel cell systems," *Energy Sustain. Dev.*, vol. 15, no. 2, pp. 137–146, 2011.
- [5] G. Sandrok, "Applications of Hydrides," in *Hydrogen Energy System: Production and Utilization of Hydrogen and Future Aspects*, 1995, pp. 253–280.
- [6] L. A. Bendersky *et al.*, "Ti_{12.5}Zr₂₁V₁₀Cr_{8.5}Mn_xCo_{1.5}Ni_{46.5-x} AB₂-type metal hydride alloys for electrochemical storage application: Part 1. Structural characteristics," *J. Power Sources*, vol. 218, pp. 474–486, 2012.
- [7] U. Eberle, M. Felderhoff, and F. Schüth, "Chemical and physical solutions for hydrogen storage," *Angew. Chemie - Int. Ed.*, vol. 48, no. 36, pp. 6608–6630, 2009.
- [8] E. . Hudson and G. Sandrok, "Engineering properties of metal hydrides," *J. Less Common Met.*, vol. 74, no. 2, pp. 435–443, 1980.
- [9] P. Dantzer, "Properties of intermetallic compounds suitable for hydrogen storage applications," *Mater. Sci. Eng. A*, vol. 329–331, pp. 313–320, 2002.
- [10] L. Pickering, M. V Lototsky, M. W. Davids, C. Sita, and V. Linkov, "Induction melted AB₂ -type metal hydrides for hydrogen storage and compression applications," *Mater. Today Proc.*, vol. 5, no. 4, pp. 10470–10478, 2018.
- [11] M. Klell, "Storage of Hydrogen in the pure form," in *Handbook of Hydrogen Storage*, 2010, p. 37.
- [12] X. Sun, S. Ohta, and W. Liu, "Hydrogen element and hydrogen gas," in *Hydrogen Molecular Biology and Medicine*, 2015, pp. 1–27.

- [13] T. Riis and G. Sandrock, “Hydrogen Storage – Gaps and Priorities,” *HIA HCG Storage Pap.*, pp. 1–13, 2005.
- [14] M. A. Rosen, “The Prospects for Renewable Energy through Hydrogen Energy Systems,” *J. Power Energy Eng.*, vol. 03, no. 04, pp. 373–377, 2015.
- [15] U. Bossel, “Hydrogen Economy.”
- [16] P. P. Edwards, V. L. Kuznetsov, W. I. F. David, and N. P. Brandon, “Hydrogen and fuel cells : Towards a sustainable energy future,” *Energy Policy*, vol. 36, pp. 4356–4362, 2008.
- [17] T. Abbasi and S. A. Abbasi, ““ Renewable ’ hydrogen : Prospects and challenges,” *Renew. Sustain. Energy Rev.*, vol. 15, pp. 3034–3040, 2011.
- [18] X. Y. Chen *et al.*, “Crystal structure and hydrogen storage properties of Ti-V-Mn alloys,” *Int. J. Hydrogen Energy*, vol. 43, no. 12, pp. 6210–6218, 2018.
- [19] P. R. Chitragar, K. V Shivaprasad, and G. N. Kumar, “Use of Hydrogen in Internal Combustion Engines : A Comprehensive Study,” *J. Mech. Eng. Biomech.*, vol. 1, no. 3, pp. 84–96, 2016.
- [20] M. W. Davids *et al.*, “Metal hydride hydrogen storage tank for light fuel cell vehicle,” *Int. J. Hydrogen Energy*, pp. 1–10, 2019.
- [21] J. Kleperis, P. Lesnicenoks, L. Grinberga, G. Chikvaidze, and J. Klavins, “Zeolite as material for hydrogen storage in transport applications,” *Latv. J. Phys. Tech. Sci.*, vol. 50, no. 3, pp. 59–64, 2013.
- [22] L. Zhou, “Progress and problems in hydrogen storage methods,” *Renew. Sustain. Energy Rev.*, vol. 9, pp. 395–408, 2005.
- [23] J. Andersson and S. Gr, “Large-scale storage of hydrogen,” *Int. J. Hydrogen Energy*, vol. 44, pp. 11901–11919, 2019.
- [24] G. Cipriani, V. Di, F. Genduso, and D. La, “Perspective on hydrogen energy carrier and its automotive applications,” *Int. J. Hydrogen Energy*, vol. 39, no. 16, pp. 8482–8494, 2014.
- [25] M. Mohan and V. Kumar, “Hydrogen storage in carbon materials — A review,” *Energy Storage*, pp. 1–26, 2019.

- [26] T. Kabutomori and K. Ohnishi, "Kinds and characteristics of hydrogen storage alloy," *Energy carriers Convers. Syst.*, vol. 2, p. 6.
- [27] D. J. Durbin and C. Malardier-Jugroot, "Review of hydrogen storage techniques for on board vehicle applications," *Int. J. Hydrogen Energy*, vol. 38, pp. 14595–14617, 2013.
- [28] B. Morten *et al.*, "Complex hydrides for hydrogen storage – new perspectives," *Mater. Today*, vol. 17, no. 3, pp. 122–128, 2014.
- [29] B. Bogdanovic, R. Brand, A. Marjanovic, M. Schwickardi, and J. Tolle, "Metal-doped sodium aluminium hydrides as potential new hydrogen storage materials," *J. Alloys Compd.*, vol. 302, pp. 36–58, 2000.
- [30] B. Bogdanovi, M. Felderhoff, and G. Streukens, "Hydrogen storage in complex metal hydrides," *J. Serbian Chem. Soc.*, vol. 74, no. 2, pp. 183–196, 2009.
- [31] C. Milanese, T. R. Jensen, B. C. Hauback, C. Pistidda, and M. Dornheim, "Complex hydrides for energy storage," *Int. J. Hydrogen Energy*, vol. 44, no. 15, pp. 7860–7874, 2018.
- [32] P. Rybár, C. Drebenstedt, M. Moloká, L. Hvizdák, and Ľ. Štrba, "Storage of liquid hydrogen in natural zeolite," *Acta Montan. Slovaca*, vol. 20, no. 3, pp. 242–250, 2015.
- [33] C. Liu, Y. Y. Fan, M. Liu, H. T. Cong, and H. M. Cheng, "Hydrogen Storage in Single-Walled Carbon Nanotubes at Room Temperature," *Science (80-.)*, vol. 286, pp. 1997–2000, 1999.
- [34] D. Zhao, D. Yuan, and H.-C. Zhou, "The current status of hydrogen storage in metal–organic frameworks," *Energy Environ. Sci.*, vol. 1, no. 2, p. 222, 2008.
- [35] Z. Ozturk, S. Medikal, D. Kose, and A. Sekizkardes, "Hydrogen storage and metal organic frameworks," *Int. Conf. Hydrog. Prod.*, p. 7, 2015.
- [36] M. Dornheim, "Thermodynamics of Metal Hydrides : Tailoring Reaction Enthalpies of Hydrogen Storage Materials," in *Thermodynamics-Interaction studies-Solids, Liquids and Gases*, 2016, pp. 1–29.
- [37] R. Griessen and A. Zuttel, "I Chapter : Short History of Hydrogen," *Sci. Technol. Hydrog. Met.*, pp. 1–9.
- [38] L. Pickering, "Ti-V-Mn based metal hydrides for hydrogen storage and compression

- application,” 2013.
- [39] M. Lototsky, B. Tarasov, and V. Yartys, “Gas phase applications of metal hydrides,” *J. Energy Storage*, vol. 72, no. 108165, 2023.
- [40] L. Kit Heung, “Using metal hydride to store hydrogen,” p. 9.
- [41] H. J. Chuang and S. L. I. Chan, “Study of the performance of Ti – Zr based hydrogen storage alloys,” *J. Power Sources*, vol. 77, pp. 159–163, 1999.
- [42] M. Y. Song, D. Ahn, I. Kwon, R. Lee, and H. Rim, “Development of AB₂-type Zr-Ti-Mn-V-Ni-Fe hydride electrodes for Ni-MH secondary batteries,” *J. Alloys Compd.*, vol. 298, no. 1–2, pp. 254–260, 2000.
- [43] K.-H. Young, S. Chang, and X. Lin, “C14 Laves Phase Metal Hydride Alloys for Ni / MH,” *Batteries*, vol. 3, no. 27, pp. 1–33, 2017.
- [44] Y. Song *et al.*, “First-principles study of hydrogen adsorption behavior in C15 Laves phase compound ZrV₂,” *AIP Adv.*, vol. 11, no. 11, 2021.
- [45] E. D. Kouloukakis, S. S. Makridis, E. Pavlidou, P. De Rango, and A. K. Stubos, “Investigation of ZrFe₂-type materials for metal hydride hydrogen compressor systems by substituting Fe with Cr or V,” *Int. J. Hydrogen Energy*, vol. 39, no. 36, pp. 21380–21385, 2014.
- [46] A. Jain *et al.*, “Synthesis , characterization and hydrogenation of ZrFe_{2-x}Ni_x(x=0.2, 0.4, 0.6, 0.8) alloy.”
- [47] T. B. Zhang *et al.*, “Hydrogen absorption properties of Zr (V 1 L x Fe x) 2 intermetallic compounds,” *Int. J. Hydrogen Energy*, vol. 37, pp. 2328–2335, 2011.
- [48] E. H. Jensen, M. Dornheim, and S. Sartori, “Scaling up Metal Hydrides for Real-Scale Applications : Achievements , Challenges and Outlook,” pp. 1–21, 2021.
- [49] S. Tan, Y. Shen, E. Onur Şahin, D. Noréus, and T. Öztürk, “Activation behavior of an AB₂ type metal hydride alloy for NiMH batteries,” *Int. J. Hydrogen Energy*, vol. 41, no. 23, pp. 9948–9953, 2016.
- [50] Y. Xu, C. Chen, X. Wang, and Q. Wang, “The structure and electrochemical properties of ball-milled Ti_{0.9}Zr_{0.2}Mn_{1.6}Ni_{0.2}V_{0.2} alloys,” *Solid State Ionics*, vol. 146, pp. 157–161, 2002.

- [51] M. Kazemipour *et al.*, “The electrochemical hydrogen storage properties of Ti_{0.72}Zr_{0.28}Mn_{1.6}V_{0.4} alloy synthesized by vacuum plasma spraying and vacuum copper boat induction melting: A comparative study,” *Int. J. Hydrogen Energy*, vol. 40, no. 45, pp. 15569–15577, 2015.
- [52] H. Chu *et al.*, “Structure , morphology and hydrogen storage properties of composites prepared by ball milling Ti_{0.9}Zr_{0.2}Mn_{1.5}Cr_{0.3}V_{0.3} with La-Mg based alloy,” *Int. J. Hydrogen Energy*, vol. 32, pp. 3363–3369, 2007.
- [53] H. Chu *et al.*, “Structure and electrochemical properties of composite electrodes synthesized by mechanical milling Ni-free TiMn₂ -based alloy with La-based alloys,” *J. Alloys Compd.*, vol. 447–447, pp. 614–619, 2007.
- [54] W. Davids, “Advanced Ti – based AB and AB₂ hydride forming materials,” 2011.
- [55] M. Kazemipour, H. Salimijazi, A. Aref Arjmand, A. Saidi, and A. Saatchi, “Electrochemical hydrogen storage capacity of Ti_{0.9}Zr_{0.1}Mn_{1.2}V_{0.4}Cr_{0.4} alloy synthesized by ball milling and annealing,” *Trans. Indian Inst. Met.*, vol. 69, pp. 1327–1333, 2016.
- [56] H. Chu *et al.*, “Structure, morphology and hydrogen storage properties of composites prepared by ball milling Ti_{0.9} Zr_{0.2} Mn_{1.5} Cr_{0.3} V_{0.3} with La-Mg-based alloy,” *Int. J. Hydrogen Energy*, vol. 32, pp. 3363–3369, 2007.
- [57] I. D. Wijayanti *et al.*, “Studies of the effect of melt spinning on the electrochemical properties of the AB₂ Laves phase alloys,” *Int. J. Mech. Eng. Sci.*, vol. 5, no. 1, pp. 24–29, 2021.
- [58] T. P. Yadav *et al.*, “Synthesis of a single phase of high-entropy Laves intermetallics in the Ti – Zr – V – Cr – Ni equiatomic alloy,” *Philos. Mag. Lett.*, vol. 0839, pp. 1–10, 2018.
- [59] T. M. Abu-lebdeh and G. P. León, “Gas Atomization of Molten Metal : Part II . Applications,” 2010.
- [60] H. J. Chuang and S. S. Huang, “Effect of annealing heat treatment on an atomized AB₂ hydrogen storage alloy,” *J. Alloys Compd.*, vol. 285, pp. 284–291, 1999.
- [61] K. Young, T. Ouchi, A. Banik, J. Koch, and M. A. Fetcenko, “Improvement in the electrochemical properties of gas atomized AB₂ metal hydride alloys by hydrogen

- annealing,” *Int. J. Hydrogen Energy*, vol. 36, no. 5, pp. 3547–3555, 2011.
- [62] M. Bram, H. P. Buchkremer, and D. Sto, “Vacuum plasma spraying of NiTi protection layers,” *Mater. Lett.*, vol. 57, pp. 647–651, 2002.
- [63] J. Kim, K. Han, K. Hwang, B. Kim, and Y. Kang, “Effect of heat treatment on microstructure and hydrogen storage properties of mass-produced,” *Int. J. Hydrogen Energy*, vol. 38, no. 14, pp. 6215–6220, 2012.
- [64] A. R. Galvis Escobar, A. Chaise, V. Iosub, B. Salque, J. F. Fernandez, and O. Gillia, “Stress effect on the swelling/shrinking behavior of an AB₂ alloy during hydrogenation cycles,” *Int. J. Hydrogen Energy*, vol. 42, no. 35, pp. 22422–22431, 2017.
- [65] V. A. Yartys and M. V Lototsky, “Laves type intermetallic compounds as hydrogen storage materials- A review,” *J. Alloys Compd.*, vol. 916, p. 165219, 2022.
- [66] S. Fashu *et al.*, “A review on crucibles for induction melting of titanium alloys,” *Mater. Des.*, vol. 186, p. 108295, 2020.
- [67] V. A. Dekhtyarenko, “Hydrogen storage properties of Ti_{15.4}Zr_{30.2}Mn₄₄V_{5.4}Cr₅ alloy produced by induction and arc melting,” *Met. Adv. Technol.*, vol. 43, no. 8, pp. 1053–1063, 2021.
- [68] K. Young, T. Ouchi, J. Koch, and M. A. Fetcenko, “Compositional optimization of vanadium-free hypo-stoichiometric AB₂ metal hydride alloy for Ni/MH battery application,” *J. Alloys Compd.*, vol. 510, no. 1, pp. 97–106, 2011.
- [69] K. Young, D. F. Wong, S. Yasuoka, J. Ishida, J. Nei, and J. Koch, “Different failure modes for V-containing and V-free AB₂ metal hydride alloys,” *J. Power Sources*, vol. 251, pp. 170–177, 2014.
- [70] K. Young, T. Ouchi, B. Huang, and M. A. Fetcenko, “Effects of B, Fe, Gd, Mg, and C on the structure, hydrogen storage, and electrochemical properties of vanadium-free AB₂ metal hydride alloy,” *J. Alloys Compd.*, vol. 511, no. 1, pp. 242–250, 2012.
- [71] K. Young, M. A. Fetcenko, F. Li, T. Ouchi, and J. Koch, “Effect of vanadium substitution in C14 Laves phase alloys for NiMH battery application,” *J. Alloys Compd.*, vol. 468, pp. 482–492, 2009.
- [72] K. Young, M. A. Fetcenko, F. Li, and T. Ouchi, “Structural, thermodynamic, and

- electrochemical properties of $\text{Ti}_x\text{Zr}_{1-x}(\text{VNiCrMnCoAl})_2$ C14 Laves phase alloys,” *J. Alloys Compd.*, vol. 464, no. 1–2, pp. 238–247, 2008.
- [73] K. Young, T. Ouchi, B. Huang, B. Reichman, and M. A. Fetcenko, “The structure , hydrogen storage , and electrochemical properties of Fe-doped C14-predominating AB₂ metal hydride alloys,” *Int. J. Hydrogen Energy*, vol. 36, no. 19, pp. 12296–12304, 2011.
- [74] Z. Cao *et al.*, “Studies on Ti-Zr-Cr-Mn-Fe-V based alloys for hydrogen compression under mild thermal conditions of water bath,” *J. Alloys Compd.*, vol. 892, p. 162145, 2021.
- [75] F. Fang, Y. Li, Q. Zhang, L. Sun, Z. Shao, and D. Sun, “Hydrogen storage properties of TiMn_{1.5}V_{0.2}-based alloys for application to fuel cell system,” *J. Power Sources*, vol. 195, no. 24, pp. 8215–8221, 2010.
- [76] K. Manickam, D. M. Grant, and G. S. Walker, “Optimization of AB₂ type alloy composition with superior hydrogen storage properties for stationary applications,” *Int. J. Hydrogen Energy*, vol. 40, no. 46, pp. 16288–16296, 2015.
- [77] X. Wang, H. Liu, and H. Li, “A 70 MPa hydrogen-compression system using metal hydrides,” *Int. J. Hydrogen Energy*, vol. 36, no. 15, pp. 9079–9085, 2011.
- [78] P. Zhou *et al.*, “Development of Ti-Zr-Mn-Cr-V based alloys for high-density hydrogen storage,” *J. Alloys Compd.*, vol. 875, p. 160035, 2021.
- [79] R. Elliott and W. Rostoker, “The occurrence of Laves-type phases among transition elements,” *Trans.ASM*, vol. 50, pp. 617–633, 1958.
- [80] M. Kandavel and S. Ramaprabhu, “Hydriding properties of Ti-substituted non-stoichiometric AB₂ alloys,” *J. Alloys Compd.*, vol. 381, no. 1–2, pp. 140–150, 2004.
- [81] M. Kandavel *et al.*, “Improvement of hydrogen storage properties of the AB₂ Laves phase alloys for automotive application,” vol. 33, pp. 3754–3761, 2008.
- [82] Z. Cao *et al.*, “Advanced high-pressure metal hydride fabricated via Ti-Cr-Mn alloys for hybrid tank,” *Int. J. Hydrogen Energy*, vol. 40, no. 6, pp. 2717–2728, 2015.
- [83] B. Tu, H. Wang, Y. Wang, R. Li, and L. Ouyang, “Optimizing TiZrCrMnNiV alloys for hybrid hydrogen storage tank of fuel cell bicycle,” *Int. J. Hydrogen Energy*, vol. 47, no.

- 33, pp. 14952–14960, 2022.
- [84] Q. Li, Z. Peng, W. Jiang, L. Ouyang, H. Wang, and J. Liu, “Optimization of Ti-Zr-Cr-Fe alloys for 45 MPa metal hydride hydrogen compressors using orthogonal analysis,” *J. Alloys Compd.*, vol. 889, p. 161629, 2021.
- [85] J. G. Park, H. Y. Jang, S. C. Han, P. S. Lee, and J. Y. Lee, “Hydrogen storage properties of TiMn₂-based alloys for metal hydride heat pump,” *Mater. Sci. Eng. A*, vol. 329–331, pp. 351–355, 2002.
- [86] J. A. Murshidi, M. Paskevicius, D. A. Sheppard, and C. E. Buckley, “Structure, morphology and hydrogen storage properties of a Ti_{0.97}Zr_{0.019}V_{0.439}Fe_{0.097}Cr_{0.045}Al_{0.026}Mn_{1.5} alloy,” *Int. J. Hydrogen Energy*, vol. 36, no. 13, pp. 7587–7593, 2011.
- [87] Z. Cao, L. Ouyang, H. Wang, J. Liu, L. Sun, and M. Zhu, “Composition design of Ti – Cr – Mn – Fe alloys for hybrid high-pressure metal hydride tanks,” *J. Alloys Compd.*, vol. 639, pp. 452–457, 2015.
- [88] M. Hagstrom, S. Klyamkin, E. Mescheryakova, and P. Lund, “High pressure AB₂ metal hydrides with low hysteresis,” *J. Mater. Sci.*, vol. 35, pp. 127–131, 2000.
- [89] U. Ulmer, M. Dieterich, A. Pohl, R. Dittmeyer, M. Linder, and M. Fichtner, “Study of the structural, thermodynamic and cyclic effects of Vanadium and Titanium substitution in Laves phase AB₂ hydrogen storage alloys,” *Int. J. Hydrogen Energy*, vol. 42, no. 31, pp. 20103–20110, 2017.
- [90] T. Nakagawa *et al.*, “Structural Properties of (Ti, Zr)(Mn,Cr)₂M_{0.1} (M = None, Fe, Co, Ni, and Cu) Hydrogen Storage Alloys: Composition Distribution and Occupied Site of Doped Element,” *Mater. Trans.*, vol. 62, no. 6, pp. 899–904, 2021.
- [91] N. Hanada *et al.*, “Effect of CO₂ on hydrogen absorption in Ti-Zr-Mn-Cr based AB₂ type alloys,” *J. Alloys Compd.*, vol. 705, pp. 507–516, 2017.
- [92] F. Liu, H. Ota, S. Okamoto, and S. Suda, “Surface properties of the fluorinated La-incorporated Ti/Zr-based AB₂ Laves phase alloys,” *J. Alloys Compd.*, vol. 253–254, pp. 452–458, 1997.
- [93] F. Liu, G. Sandrock, and S. Suda, “Surface and metallographic microstructure of the La-added compound (Ti, Zr)(Mn, Cr, Ni)₂,” *J. Alloys Compd.*, vol. 231, pp. 392–396,

- 1995.
- [94] F. J. Liu and S. Suda, "F-treatment effect on the hydriding properties of the La-substituted AB₂ compound (Ti, Zr)(Mn, Cr, Ni)₂," *J. Alloys Compd.*, vol. 231, no. 1–2, pp. 666–669, 1995.
- [95] M. Gao, H. Miao, Y. Zhao, Y. Liu, and H. Pan, "Effects of rare earth elements substitution for Ti on the structure and electrochemical properties of a Fe-doped Ti-V based hydrogen storage alloy," *J. Alloys Compd.*, vol. 484, pp. 249–255, 2009.
- [96] K. Young, D. F. Wong, T. Ouchi, B. Huang, and B. Reichman, "Effects of La-addition to the structure, hydrogen storage, and electrochemical properties of C14 metal hydride alloys," *Electrochim. Acta*, vol. 174, pp. 815–825, 2015.
- [97] B. Friedrich, "Large-Scale Production and Quality Assurance of Hydrogen Storage (Battery) Alloys," vol. 3, no. February, pp. 37–46, 1994.
- [98] M. W. Davids *et al.*, "Effect of preparation routes on the performance of a multi-component AB₂-type hydrogen storage alloy," vol. 6, pp. 1–12, 2024.
- [99] J.-L. Bobet, B. Chevalier, and B. Darriet, "Crystallographic and hydrogen sorption properties of TiMn₂ based alloys," *Intermetallics*, vol. 8, pp. 359–63, 2000.
- [100] U. Troitzsch, A. Christy, and D. Ellis, "The crystal structure of disordered (Zr,Ti)O₂ solid solution including srilankite: Evolution towards tetragonal ZrO₂ with increasing Zr.," *Phys. Chem. Miner.*, vol. 32, pp. 504–14, 2005.
- [101] M. Martin-Sedeno *et al.*, "Structural and Electrical Investigation of Oxide Ion and Proton Conducting Titanium Cuspidines," *Chem. Mater.*, vol. 17, pp. 5989–98, 2005.
- [102] I. Zavalij, G. Wojcik, G. Mlynarek, I. Saldan, V. Yartys, and M. Kopczyk, "Phase-structural characteristics of (Ti_{1-x}Zr_x)₄Ni₂O_{0.3} alloys and their hydrogen gas and electrochemical absorption desorption properties.," *J. Alloys Compd.*, vol. 314, pp. 124–131, 2001.
- [103] M. Mahadeshwara, "Transmission electron microscopy," *Tribonet*, 2022. .
- [104] M. Alnarabiji, O. Tantawi, A. Ramli, N. Zabidi, O. Ghanem, and B. Abdullah, "Comprehensive review of structured binary Ni-NiO catalyst: Synthesis, characterization and applications," *Renew. Sustain. Energy Rev.*, vol. 114, p. 109326,

- 2019.
- [105] F. Jones, "Particle size measurement by the X-ray method.," *J. Sci. Instruments*, vol. 18, pp. 157–8, 1941.
- [106] S. Hassanzadeh-Tabrizi, "Precise calculation of crystallite size of nanomaterials: A review.," *J. Alloys Compd.*, vol. 968, p. 171914, 2023.
- [107] S. Lee and T. Perng, "Effects of boron and carbon on the hydrogenation properties of TiFe and Ti_{1.1}Fe," *Int. J. Hydrogen Energy*, vol. 25, no. 9, pp. 831–836, 2000.
- [108] P. Yadav, R. Shahi, and N. Srivastava, "Synthesis, characterization and hydrogen storage behaviour of AB₂ (ZrFe₂, Zr(Fe_{0.75}V_{0.25})₂, Zr(Fe_{0.5}V_{0.5})₂) type materials," *Int. J. Hydrogen Energy*, vol. 37, pp. 3689–3696, 2012.
- [109] Y. L. Zhang, J. S. Li, T. B. Zhang, R. Hu, and X. Y. Xue, "Microstructure and hydrogen storage properties of non-stoichiometric Zr-Ti-V Laves phase alloys," *Int. J. Hydrogen Energy*, vol. 38, no. 34, pp. 14675–14684, 2013.
- [110] Y. Morita, T. Gamo, and S. Kuranaka, "Effects of non-metal addition on hydriding properties for Ti-Mn Laves phase alloys," *J. Alloys Compd.*, vol. 253–254, pp. 29–33, 1997.
- [111] M. Tsukahara, K. Takahashi, A. Isomura, and T. Sakai, "Influence of oxygen on hydrogen storage and electrode properties for micro-designed V-based battery alloys," *J. Alloys Compd.*, vol. 265, pp. 257–263, 1998.
- [112] W. Davids and M. Lototskyy, "Influence of oxygen introduced in TiFe-based hydride forming alloy on its morphology, structural and hydrogen sorption properties," *Int. J. Hydrogen Energy*, vol. 37, pp. 18155–18162, 2012.
- [113] T. Ha *et al.*, "Hydrogen occupation in Ti₄M₂O_y compounds (M=Fe, Co, Ni, Cu, and y=0,1) and their hydrogen storage characteristics," *J. Alloys Compd.*, vol. 891, p. 162050, 2021.
- [114] Z. Dehouche, M. Savard, F. Laurencelle, and J. Goyette, "Ti-V-Mn based alloys for hydrogen compression system," *J. Alloys Compd.*, vol. 400, pp. 276–280, 2005.
- [115] C. Lundin, F. Lynch, and C. Magee, "A correlation between the interstitial hole sizes in intermetallic compounds and the thermodynamic properties of the hydrides formed from

- those compounds,” *J. Less Common Met.*, vol. 56, pp. 19–37, 1977.
- [116] P. Zhou, Z. Cao, X. Xiao, and Z. Jiang, “Study on low-vanadium Ti- Zr -Mn-Cr-V based alloys for high-density hydrogen storage,” *Int. J. Hydrogen Energy*, vol. 47, no. 3, pp. 1710–1722, 2021.
- [117] Y. Xu, C. Chen, W. Geng, and Q. Wang, “The hydrogen storage properties of Ti-Mn based C14 Laves phase intermetallics as hydrogen resource for PEMFC,” *Int. J. Hydrogen Energy*, vol. 26, pp. 593–596, 2001.
- [118] O. Bernauer, J. Topler, and D. Noreus, “Fundamentals and properties of some Ti/Mn based Laves phase hydrides,” *Int. J. Hydrogen Energy*, vol. 14, pp. 187–200, 1989.
- [119] J. Liu, L. Sun, J. Yang, D. Guo, D. Chen, and L. Yang, “Ti – Mn hydrogen storage alloys : from properties to,” pp. 35744–35755, 2022.



UNIVERSITY of the
WESTERN CAPE



UNIVERSITY *of the*
WESTERN CAPE